MYELINATION IN THE AUDITORY BRAINSTEM

ALISHA L. NABEL

Graduate School of
Systemic Neurosciences
LMU Munich

Dissertation der Graduate School of Systemic Neurosciences der
Ludwig-Maximilians-Universität München

June 21, 2021

Supervisor:
Prof. Dr. Benedikt Grothe
Division of Neurobiology
Department Biology II
Ludwig-Maximilians-Universität München

First Reviewer:	Prof. Dr. Benedikt Grothe
Second Reviewer:	Dr. Tim Czopka
External Reviewer:	Prof. Charles ffrench-Constant
Date of submission:	June 21, 2021
Date of oral defense:	September 13, 2021

Für Mama

»Waren sie nicht zufrieden, wo sie sich befanden?«
– »wir sind nie zufrieden, wo wir sind«, sagte der Weichensteller.
— Antoine de Saint-Exupéry

ABSTRACT

The evolution of myelin was a major key event in vertebrates which aimed to enhance conduction velocity of electrical impulses in axons. Distinct myelination patterns along axons can shape the speed and timing of action potentials. Exact arrival time of inputs at target neurons are crucial for proper neural circuit function. Two key determinants for tuning conduction velocity of myelinated axons are the length of individual myelin sheaths together with the axon diameter. However, it remains unanswered who determines specific myelination patterns along axons – the oligodendrocyte or the axon? And further, when and how do structural parameters of myelinated axons develop in neural circuits in general, in terms of their functionally relevant myelination patterns, axonal morphology and nodes of Ranvier?

A system with highest temporal demands is the mammalian sound localization system. Globular bushy cell (GBC) axons involved in circuits processing sound location information are some of the fastest and most precise conducting axons in the mammalian central nervous system. In the Mongolian gerbil (*Meriones unguiculatus*) GBCs that are tuned to low sound frequencies transmit sound signals to the binaural comparator neurons in the medial superior olive (MSO) where the arrival time of sound at the two ears (interaural time differences; ITDs) is computed. These differences can be as low as only a few microseconds and thus, computation of ITDs relies on explicitly fast and highly precise axons. To cope with the need for exact input timing, low-frequency GBC axons exhibit specific structural adaptations to adjust conduction velocity. Their exceptional thick axons combined with comparably short internodes result in unusual low ratios of internode length to axon diameter (L/*d* ratios) which in turn increase the conduction velocity along their axons. To gain insight into when and how the specific myelin sheath lengths, axon diameter and thus L/*d* ratios are established, we characterized the developmental time course of these structural parameters at timepoints before and after the onset of hearing. Our findings show the internode length is set prior to a significant axon diameter increase. While the internode length is established already two days before hearing onset, which is at P12, the axon diameter only increases five days after hearing onset, and thereby decreasing its L/*d* ratio. This strongly suggests that, at least in GBCs, the axon itself is the key determinant in ensuring that the required conduction velocity is met by adjusting its diameter retrospectively.

Together with the length of myelin sheaths and the axon diameter, nodes of Ranvier are critical determinants of action potential speed and timing of and therefore the development of all these structures must be tightly regulated. By assessing the development of nodes of Ranvier we found that axon and node morphology by and large mature synchronously. Early nodal clusters appear already when myelination of GBC axons is initiated at P6/P7 and these premature clusters subsequently progress

until reaching maturity during the 4th postnatal week. Interestingly, we were able to show that node maturation depends on the location along the axon with nodes closer to the cell body develop earlier compared to nodes close to the synaptic terminal.

The adjustment of structural parameters of myelinated axons is a fundamental prerequisite for proper function of neuronal circuits. Understanding how these structures develop along GBC axons could raise awareness of the general developmental time course of morphological features along myelinated axons.

CONTENTS

1. INTRODUCTION

1.1. MYELIN

During evolution animals began to invade new and potentially riskier environments and consequently they required complex and quicker escape and predatory responses. Consequently, the speed of conduction along nerve fibers became a critical factor for survival (Zalc & Coleman, 2000). The need for higher conduction velocity of signal transmission initiated the evolution of two key mechanisms (Hartline & Colman, 2007). The first solution to enhance the conduction velocity along nerve fibers aimed to decrease the axial resistance of nerve fibers by increasing the inner axon diameter (Hartline & Colman, 2007). The increase of conduction velocity in proportion to the square root of the interior diameter of a nerve fiber (Hodgkin, 1954) led to the evolution of giant axons in circuits with a high demand for speed (e.g. escape jetting of the squid or tail-flip response of the lobster and crayfish (Eaton & Robert, 1984)). Yet, one major disadvantage came with this mechanism; bigger axons need more space.
Thus, an alternative fundamental adaptation in vertebrates evolved to facilitate action potential propagation. Faster conduction speeds can also be achieved by decreasing transverse capacitance and increasing transmembrane resistance. This lead to the evolution of myelin, which ensheathes and thus insulates nerve fibers with a lipid-rich multilaminar membrane – the myelin sheath (Hartline & Colman, 2007).

1.1.1. Myelin - structure and function

The existence of myelin was first described by Virchow already in 1858 who introduced the term ‘myelin’ from the greek word ‘myelos’ (marrow). However, for a long time it has been assumed that myelin was secreted by the neuron itself (Virchow, 1856) and it took almost a century to realize that myelin is formed by specialized glial cells (Del Río Hortega, 1921, 1922, 1928). In the central nervous system (CNS) of vertebrates the myelin-forming glia cells are oligodendrocytes which extend their plasma membrane and enwrap long segments around axons in a spiral fashion. (Rasband & Peles, 2016; Simons & Nave, 2016). A single oligodendrocyte is able to myelinate up to 60 axons (Hildebrand et al., 1993). The myelinated segments are called internodes and consist of tightly packed cell membranes (Bunge et al., 1961) which are only interrupted at small unmyelinated sections between two consecutive sheaths, the nodes of Ranvier (Huxley & Stampfli, 1949; Ranvier, 1871) (Figure 1A). Nodes of Ranvier are highly specialized regions and play a crucial role in action potential

generation and propagation (Rasband & Peles, 2016). The tight compaction of myelin membranes around axons leaves space for cytoplasm only at the non-compacted ends of the myelin spiral, termed the inner and outer tongue (Chang et al., 2016). The extracellular space between the axon and the myelin sheath is termed the periaxonal space (Simons & Nave, 2016) (Figure 1B).

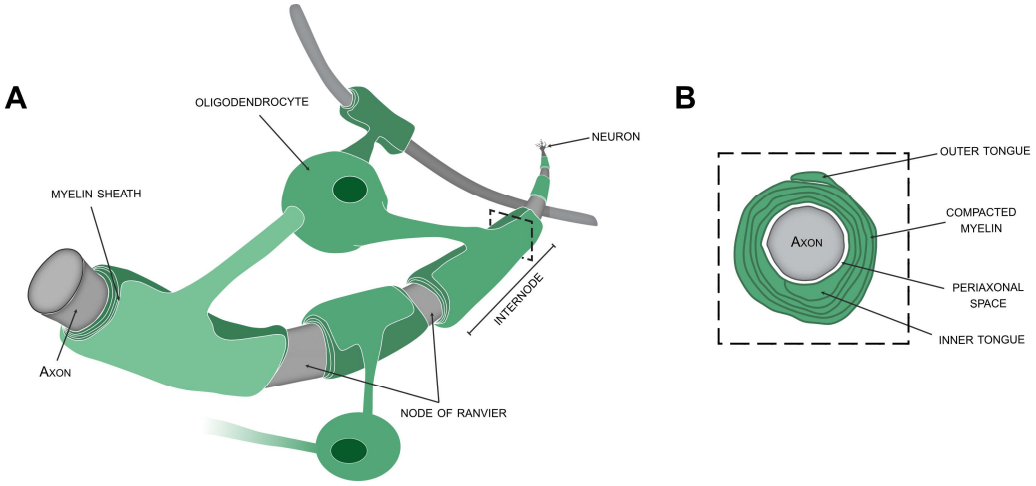

Figure 1: Architecture of a myelinated axon in the CNS. (A) Schematic of myelinated axons with oligodendrocytes (green) forming myelin sheaths around axons (gray). The myelinated segments are termed internodes and are interspersed with small unmyelinated segments, the nodes of Ranvier (adapted from Chilton, 2020). (B) Cross-sectional view of a myelinated axon. Compacted myelin lays in between the inner and outer tongue and the periaxonal space is located between axon and myelin sheath.

Structurally, a myelinated axon can be divided into four distinct compartments: the node of Ranvier, the paranode, the juxtaparanode (JXP) and internode. Their highly distinctive molecular composition is required in order to accurately meet their specific functions (Bunge et al., 1961; Simons & Nave, 2016). In principle, myelination fulfills two main functions in which neurons benefit from their myelinated axons. First, the ensheathment of axons with myelin increases conduction velocity of action potentials, and second, myelin reduces the energy required for action potential transmission (Nave, 2010) and the latter being potentially the phylogenetically older function (Weil et al., 2018).

Action potential propagation

The tight enwrapment of axons into the lipid-rich multilaminar myelin membrane electrically insulates the axon. This insulation decreases the transverse capacitance between inside and outside of the nerve fibers while increasing the resistance (Hartline & Colman, 2007; Kuhn et al., 2019). In addition, myelination of axons clusters voltage gated sodium (Na_v) channels in a high density at the nodes of Ranvier (Kaplan et al., 1997; Salzer, 2003) thereby allowing the action potential to ‘jump’ from one node to

the next, called saltatory conduction (Huxley & Stampfli, 1949; Hursh, 1939; Tasaki, 1939) (Figure 2A). Hence both the insulating myelin membrane together with the clustering of ion channels at the nodes speed up propagation of electrical impulses. In non-myelinated axons, the speed of conduction is proportional to the square root of the diameter (Hursh, 1939; Pumphrey & Young, 1938; Rushton, 1951), while in myelinated axons the relationship is linear, i.e. the speed is directly proportional to the axon diameter (Hursh, 1939; Waxman, 1980). The unmyelinated squid giant axon with a diameter of 500 µm has conduction velocity of 25 m/s (Bullock & Horrdige, 1965), however saltatory conduction in myelinated axons enables the propagation of action potentials with up to 70 – 120 m/s in axons with diameters of 12 – 20 µm (Chambers et al., 2015). However, the length of internodes and the thickness of myelin also affects conduction velocity (Hursh, 1939; Waxman, 1980; Zalc et al., 2008).

The ratio of the inner axon diameter to the diameter of the myelinated axon is called g-ratio and plays an important role in determining the conduction speed (Figure 2B). Theoretical calculations revealed a g-ratio of 0.6 at myelinated nerve fiber for optimal conduction speed in the PNS (Rushton, 1951; Smith & Koles, 1970). For the CNS more recent calculations predicted an optimal g-ratio of 0.7 (Chomiak & Hu, 2009) (Figure 2B). In addition, the length of the myelin sheath is an important factor that influences the speed of signal transmission. For a long time it has been believed that conduction velocity increases with increasing internode length until a threshold of internode length is reached (Hursh, 1939; Huxley & Stampfli, 1949; Rushton, 1951; Waxman, 1980). While the positive correlation of sheath length and conduction velocity might be true for myelinated axons in the PNS (Wu et al., 2012) their relationship are less clear and potentially more complex in the CNS. In the CNS, various recent studies have reported variable patterns of myelin sheath length affecting and optimizing the conduction velocity (Auer et al., 2018; Ford et al., 2015; Hill et al., 2018; Krasnow et al., 2018; Micheva et al., 2016; Tomassy et al., 2014). In particular the ratio of internode length to axon diameter (L/*d* ratio) has been shown to determine conduction velocity and the precise timing of action potentials along myelinated axons in the CNS. More specifically, in a subpopulation of globular bushy cell (GBC) axons involved in sound localization circuits specific L/*d* ratios define the speed of conduction with unusual low L/*d* ratios facilitating the transmission of action potentials (Ford et al., 2015) (Figure 2C). To transmit information with exceptionally high speed and precision, these neurons rely on their unique L/*d* ratio. Modeling of conductance in these specific GBC fibers revealed that shorter internodes leading to smaller L/*d* ratios result in a faster rise time of APs, shorter AP half-width, and increased AP amplitude compared to L/*d* ratios around 100. Longer internodes are less efficient at transferring the current from one node to the next, leading to less synchronous activation of Na_v channels and less rapid and synchronous activation of potassium channel and thereby resulting in increased half width of the AP. However, activating more sodium channels is more costly in terms of energy consumption. Thus,

the small L/d ratio in the subpopulation of GBC axons represents a compromise between speed, precision, and energy consumption (Ford et al., 2015).

This recent discovery challenged the traditional assumption of a rather stable L/*d* ratio of ~100 amongst all neurons (Hursh, 1939; Rushton, 1951) and suggested a more central and complex role of L/*d* ratios in determining conduction velocity in the CNS.

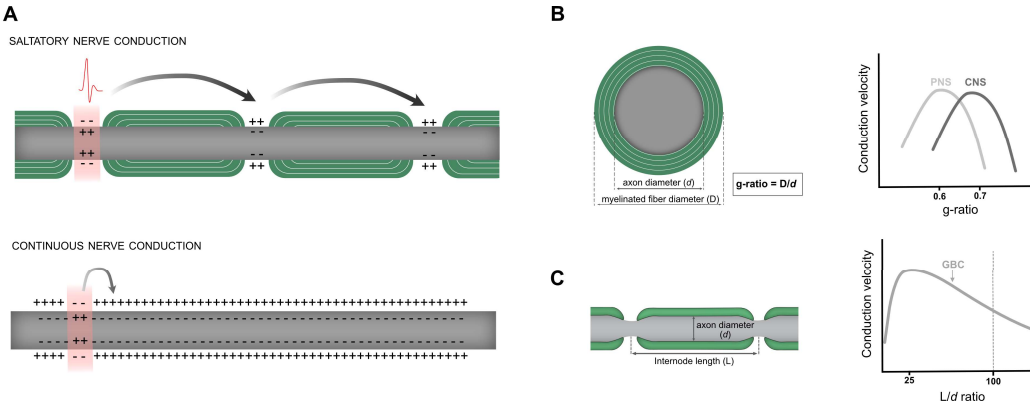

Figure 2: Function of myelinated axons to increase conduction velocity. **(A)** Schematic of saltatory nerve conduction (*top*) and continuous nerve conduction (*bottom*). **(B)** Schematic illustrates the g-ratio which is calculated by division of the axon diameter (d) by the diameter of the myelinated fiber (D; *left*). Optimal value for AP conduction can be calculated for g-ratios and deviations result in slower conduction (*right*). **(C)** Optimal ratio of axon diameter to internode length (L/*d* ratio) in globular bushy cell (GBC) axons (arrow) deviate from the assumed stable value of ~100 (dotted line) and conduction velocity decreases when L/*d* ratio increases (*right*; adapted from Ford et al., 2015) (inspired by Auer, 2019).

Metabolic support

Apart from their famous function in ensheathing axons and thereby facilitating AP propagation, oligodendrocytes also play an essential role as a metabolic supporter for the neuron (Fünfschilling et al., 2012; Lee et al., 2012a) and this function may even represent the ancestral function of glial cells prior to the evolution of myelin (Weil et al., 2018). Neurons with their high demands for energy require substantial amounts of ATPs to maintain the activity for the Na^+/K^+ channels, but they do not possess energy stores themselves (Philips & Rothstein, 2017). The contribution of glial cells to neuronal metabolism was initially proposed for astrocytes (Kasischke et al., 2004; Pellerin & Magistretti, 1994). However, since axons are widely covered by myelin and astrocytes can only contact the neurons at the unmyelinated nodes of Ranvier the concept emerged that myelin-forming oligodendrocytes provide essential metabolites to the axon (Philips & Rothstein, 2017). One essential nutrient for the axon is lactate (or pyruvate) which is generated by oligodendrocytes (Fünfschilling et al., 2012; Lee et al., 2012a). Oligodendrocytes transport lactate to the axon via the monocarboxylate

transporter 1 (MCT1) to the axon. The transport of lactate (or pyruvate) via MCT1 through oligodendrocytes to the axon appears to be a fundamental property to maintain the function and survival of axons and neurons (Lee et al., 2012a). The lactate generated by the oligodendrocyte can be readily metabolized by the axon for production of mitochondrial ATP (Fünfschilling et al., 2012). In addition, the import of glucose through glia glucose transporters (GLU1) is required (Lee et al., 2012a). First, oligodendrocytes take up glucose from the extracellular space which is then metabolized via glycolysis into lactate and pyruvate. Consequently, the lactate and pyruvate can be transported via the monocarboxylate transporter 1 (MCT1) into the periaxonal space from where they can be taken into the axon via MCT2. Within the axon lactate is converted into pyruvate which is imported into mitochondria and ATP is generated through the Krebs-cycle and the oxidative phosphorylation to provide the axon with energy (Morrison et al., 2013; Stadelmann et al., 2019).

1.1.2. The node of Ranvier - structure and function

A myelinated axon consists of several distinct compartments; the node of Ranvier, the paranode, the juxtaparanode and the internode. Each domain has a very specific and essential role in contributing to the fast and saltatory nerve conduction. The molecular composition and function of each domain is described below and illustrated in Figure 3.

The node of Ranvier

The node of Ranvier is the small unmyelinated interruption between compact myelin sheaths and represents the site of action potential generation and maintenance. Nodes of Ranvier are highly enriched in Na_v channels (Poliak & Peles, 2003; Rasband, 2012; Salzer, 2003) which mediate the ion flux across the membrane (Rasband & Peles, 2016). The predominant Na_v channel in adult nodes is $Na_v1.6$. Before adulthood, as nodes are forming, $Na_v1.2$ is expressed and is only later replaced by $Na_v1.6$ in most nodes in the CNS (Boiko et al., 2001; Salzer, 2003). In addition to Na_v channels, the scaffolding proteins AnkyrinG (AnkG) and ßIV-spectrin are enriched at nodes of Ranvier. They link the ion channels and cell adhesion molecules (CAMs), Neurofascin186 (NF186) and NrCAM, to the underlying axon cytoskeleton. These CAMs interact with the extracellular matrix and together with AnkG and ßIV-spectrin connect ion channels to extrinsic (glial) interactions (Rasband & Peles, 2016).

The paranode

The node of Ranvier is flanked on either side by the paranode where each myelin segment is attached to the axon (Rasband & Peles, 2016; Rosenbluth, 2009). The highly complex structure ensures the tight anchoring of myelin and is called the paranodal junction (PNJ). Here, myelin lamellae split into multiple cytoplasmic loops,

termed paranodal loops, that form septate-like junctions, specialized intercellular junctions providing tight adhesion between the axon and the oligodendrocyte. The axonal surface is connected to the oligodendrocyte through a ternary complex consisting of the adhesion protein Contactin-associated protein 1 (CASPR1) and Contactin 1 (Cntn1) on the axonal side that binds to Neurofascin155 (NF155) on the glial surface, thereby providing the tight seal between axon and the myelin sheath (Rasband & Peles, 2016; Salzer, 2003; Simons & Nave, 2016). This seal of the myelin sheath to the axon enables fast and efficient conduction by preventing current leakage. A further important functions of the PNJ is the segregation of Na_v channels at the nodes from voltage-gated potassium (K_v) channels at the juxtaparanode (Stadelmann et al., 2019). In addition to the axoglial adhesion at the paranodal region, the loop-loop adhesion is critical for proper impulse propagation. Loss of the adhesion between loops results in disrupted axonal patterning around the nodes, increased paranodal axon diameter, lower action potential threshold, and increased conduction velocity. Therefore, together with the axoglial adhesion, the loop-loop adhesion is critical for maintaining the integrity of paranodal spirals to ensure proper neuronal function (Jarjour et al., 2020).
The PNJ has diverse and crucial functions including the attachment of the myelin sheath to the axon, limiting current leakage and spatially separating conductances (Rasband & Peles, 2016; Rosenbluth, 2009). Moreover, the PNJ is also essential for the formation of nodal and juxtaparanodal compartments (Rasband & Peles, 2016).

The juxtaparanode
The juxtaparanode (JXP) is located adjacent to the paranode beneath the compact myelin. This domain is highly enriched in K_v1 channels consisting of $K_v1.1$, $K_v1.2$, $K_v1.4$ and $K_vß2$ subunits (Chiu & Ritchie, 1980; Rasband, 2011; Rasband & Peles, 2016). At the JXP a homologous interaction compared to that at paranodes was found. Here, Contactin 2 (Cntn2) and CASPR2 form a complex to properly cluster K_v1 channels. The juxtaparanodal K_v channels are proposed to prevent re-entrant excitation for maintaining the internodal resting potential and in addition the JXP mediates communication between the axon and the oligodendrocyte (Poliak & Peles, 2003).

The internode
The internode is the myelinated segment between two paranodal domains. The innermost noncompacted lamellae of the myelin sheath faces the periaxonal space and is therefore able to communicate with the neuron (Simons & Nave, 2016).

The explicit and unique composition of each domain and their protein-protein interaction are designed and orchestrated to facilitate the rapid propagation of nerve impulses. Every detail in each domain contributes to fast and saltatory nerve conduction (Rasband & Peles, 2016).

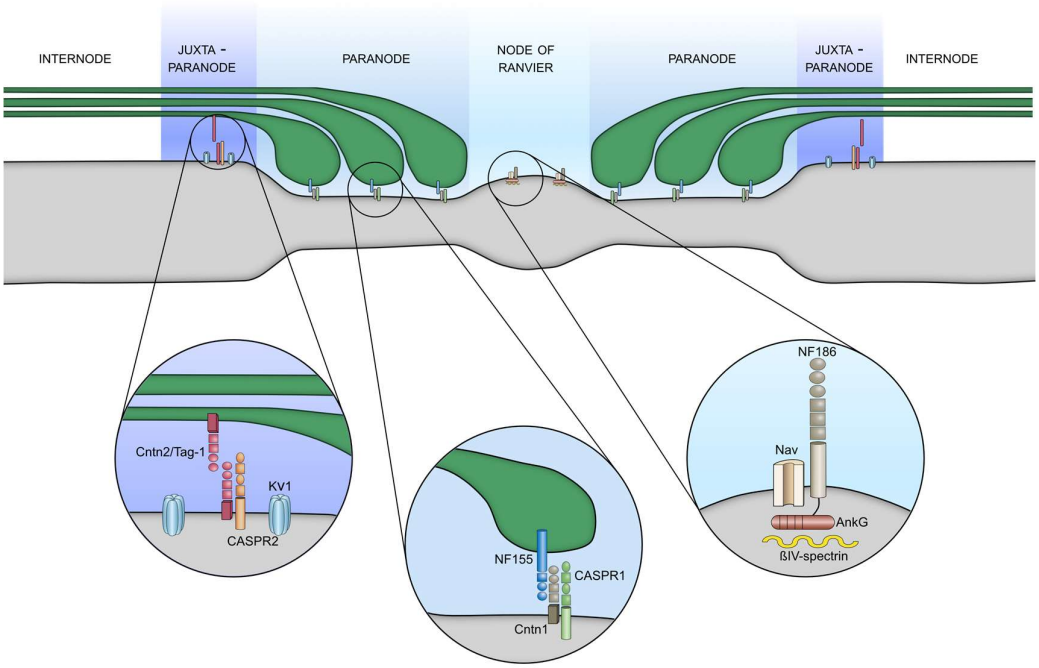

Figure 3: Architecture of the node of Ranvier. Nodes of Ranvier consist of distinct compartments, the node, the paranode, the juxtaparanode (JXP) and the internode. At the node, high densities of voltage gated sodium channels (Na_v) are linked to AnkyrinG (AnkG) and ßIV-spectrin, and Neurofascin186 (NF186) is also associated with AnkG. At the paranode, paranodal loops form tight seals between the axon and the myelin sheath via a ternary adhesion complex consisting of, Contactin 1 (Cntn1) and Neurofascin155 (NF155). At the JXP voltage gated potassium channels (K_v1) are clustered in a high density. CASPR2 and Contactin 2/Tag-1 (Cntn2/Tag-1) are also localized at the JXP.

1.1.3. The node of Ranvier - formation

In the last two decades, extensive research has focused on the formation of nodes of Ranvier in the CNS. Many open questions have been answered and a range of potential mechanisms proposed. While the exact mechanism is still not completely understood, several findings are widely accepted. In general, node formation is initiated by myelination (Brivio et al., 2017; Rasband & Peles, 2016; Susuki et al., 2013). There are three independent mechanisms involved in assembly of nodes of Ranvier ensuring proper assembly: (1) Clustering of NF186 by a glia derived extracellular matrix (ECM) complex; (2) the formation of PNJs as diffusion barriers to restrict nodal proteins and (3) anchoring of sodium channels to the cytoskeleton by axonal Cytoskeletal Scaffolds (SCs) (Susuki et al., 2013).

The formation of the PNJ is assumed to be the primary process in CNS node formation. The glial NF155 and axonal CASPR and Cntn1 are expressed and interact to form the PNJ, which then acts as lateral diffusion barrier between growing internodes (Sherman & Brophy, 2005; Susuki et al., 2013). After PNJ formation, Na_v channels cluster at the tips of the oligodendrocyte processes forming myelin sheaths together with NF186, AnkG and ßIV-spectrin (Susuki et al, 2013). The resulting heminodes are believed to elongate until they meet the next heminode and fuse to mature nodes of Ranvier (Brivio et al., 2017; Feinberg et al., 2010; Pedraza et al., 2001; Rasband & Peles, 2016). Lastly, the complex of Na_v and AnkG needs to be stabilized. This is achieved through interaction of ßIV-spectrin and the axon cytoskeleton and through NF186 interacting with the nodal core ECM components (Bcan, Vcan, Bral1, NrCAM) (Susuki et al., 2013).

1.1.4. Myelin - formation, growth and compaction

Myelin is formed by oligodendrocyte precursor cells (OPCs) that undergo differentiation into mature myelinating oligodendrocytes that are able to wrap around axons (Sherman & Brophy, 2005). Mature oligodendrocytes extend their highly dynamic and motile processes interacting with multiple prospective axons in their environment (Almeida & Lyons, 2017). Once making contact with an axon, oligodendrocytes form nascent sheaths but many of these early sheaths are retracted again (Czopka et al., 2013; P. Liu et al., 2013). Sheath retraction was found to be triggered by an elevation of the intracellular Ca^{2+} levels (Baraban et al., 2017; Krasnow et al., 2018). The remaining sheaths subsequently start to myelinate the axons and extend laterally. For instance, in zebrafish, upon the start of myelination, the oligodendrocyte forms new sheaths only within a 5 - 6-hour time window. After this period no further sheaths are formed (Czopka et al., 2013).

Formation

But how exactly do oligodendrocytes wrap their membrane around axons?

Different models have been suggested describing potential mechanisms of myelin formation. In the PNS, the ‘carpet crawler’ model proposed by Bunge et al., (1961) is generally accepted. According to the model, Schwann cells first extend along the entire axonal segment and only afterwards make one turn and move underneath the growing sheath. The inner tongue then continuously moves underneath the previously generated layers of myelin membrane.

In the CNS, the complicated pattern of developing myelin sheaths has led to the proposal of various mechanisms, ranging from a ‘croissant-like’-, (Sobottka et al., 2011) to a ‘yo-yo’-model (Pedraza et al., 2001). However, new technologies revealed a model that combines several features of previous proposed mechanisms. The current understanding of CNS myelin formation is that myelin grows by two coordinated

motions: by wrapping of the leading edge (inner tongue) around the axon underneath the previously deposited membrane, combined with the lateral extension of individual myelin layers towards the future nodes (Snaidero & Simons, 2014). During these processes each myelin layer is always in close contact with the axonal surface forming the coiling helical pattern (Butt & Berry, 2000; Pedraza et al., 2001; Sobottka et al., 2011). The edges move towards the nodal regions, eventually forming the 'paranodal loops' (Snaidero & Simons, 2014).

Growth

In order to allow the radial growth of myelin at the innermost tongue, the newly synthetized membrane has to be transported throughout the developing myelin sheath. This transport of myelin to the growth zone is achieved through cytoplasmic-rich (myelinic) channels (Velumian et al., 2011) which are mainly found in developing myelin sheaths but largely disappear after completion of myelination (Snaidero & Simons, 2014). In contrast, for lateral growth of the myelin sheath, the membrane needs to be transported to the lateral edges of each myelin layer. Here, cytoplasmic channels can be found which later form the paranodal loops. These channels remain open in order to, for example later adjust internode length (Snaidero & Simons, 2014).

Compaction

Myelin achieves its insulating function by exclusion of water-rich media resulting in extremely close and intimate appositions of the plasma membranes (Bakhti et al., 2013; Chang et al., 2016). To compact the extracellular sides of myelin, membrane adhesion and water exclusion is required (García-Mateo et al., 2018) and starts early in development after only a few wraps (Readhead et al., 1987). Compact myelin is visible as a periodic ultrastructure in electron microscopy and the compaction requires the expression of structural proteins such as proteolipid protein (PLP) and myelin basic Protein (MBP) in the CNS (Nave, 2010). For instance, shiverer mice lacking MBP fail to generate compact myelin (Privat et al., 1979; Rosenbluth, 1980). As described previously, membrane growth occurs at the innermost region of the myelin sheath, whereas compaction starts in the outermost layers and progress inward. This spatial segregation and coordinated regulation of myelin growth and compaction prevents premature compaction of the growing zone (Snaidero & Simons, 2014). There are two types of myelin compaction: the intracellular compaction between two cytoplasmic membranes and the poorly understood compaction between two extracellular leaflets (García-Mateo et al., 2018). While cytoplasmic leaflets are held tightly together by MBP, extracellular leaflets interactions are much weaker and poorly understood (Snaidero & Simons, 2014). Once the positively charged MBP is bound to the two adjacent negatively charged cytoplasmic membrane surfaces, the cytoplasmic side of the two bilayers have been brought into close apposition (Aggarwal et al., 2011).

1.1.5. Myelination patterns and their determinants

As described earlier, a main function of the myelin sheath around axons is to enhance conduction velocity of action potentials. Not only the variability of the myelin thickness can affect conduction velocity but also the lengths and patterning of individual myelin sheaths are crucial determinants in shaping action potential speed and timing.

Distinct patterning regarding the length of individual myelin sheaths can affect conduction velocity and axons exhibiting such unique myelination patterns have been found in the CNS. For instance, a pattern with yet unknown function was found in axons of pyramidal neurons in the mouse neocortex. Here, neurons exhibit a patchy myelination pattern. Myelinated axonal tracts of variable length are interspersed with long, unmyelinated tracts, much longer than typical nodes of Ranvier (Tomassy et al., 2014).
Moreover, in the gerbil auditory brainstem, globular bushy cell (GBC) axons involved in time critical sound localization circuits exhibit unique and specific myelination patterns enabling rapid action potential conduction speed (Ford et al., 2015). One adaption along these axons is the progressively shortening of internodal lengths towards the synapse allowing secure and precise action potential transmission. A second adaptation is that internode length is shorter in thicker and faster conducting GBC axons compared to thinner and slower conducting GBC axons (Ford et al., 2015). Hence, different and highly distinctive myelination patterns adjusting speed and timing of conduction have been reported in various species and neural systems (Ford et al., 2015; Lang & Rosenbluth, 2003; Salami et al., 2003; Seidl et al., 2010; Seidl & Rubel, 2016). This raises the question whether and how oligodendrocytes decide which axons and which parts of the axon are myelinated and on what pattern. Does the oligodendrocyte play a role in this decision at all? And if so, to what extent? These questions have been the subject of extensive debate and evidence for both possibilities exist.

A study revealed evidence for a central role of the oligodendrocyte in determining myelination patterns, in particular the myelin sheath length. Oligodendrocytes form sheath lengths around artificial fibers generating expected *in vivo* length. Here, without any feedback from axons, oligodendrocytes originating from the cortex form shorter internodes compared to spinal cord oligodendrocytes, indicating a regional identity of oligodendrocytes and hence a specific intrinsic program (Bechler et al., 2015). The fact that oligodendrocytes are able to ensheath myelin around inert fibers with no intrinsic factors (Bechler et al., 2015a; S. Lee et al., 2012b) also suggests an essential role of physical cues such as axon caliber in regulation of myelination (Bechler et al., 2015, 2017). In the PNS, axon diameter is a clear threshold of myelination with axons of a diameter of 1µm are myelinated (Snaidero & Simons, 2014). However, in the CNS

there is an overlap of myelinated and unmyelinated axons with diameters between 0.2µm and 0.8µm (Remahl & Hildebrand, 1982; Waxman & Bennett, 1972) indicating additional factors. For Instance, several molecules have been found to be expressed by axons, either inhibiting the oligodendrocyte outgrowth or the interaction of the oligodendrocyte with the axon (Simons & Lyons, 2013). Hence, it is likely that a combination of physical cues and the loss of negative inhibitory factors regulate myelination in the CNS. In addition, different factors were shown to modulate myelination to some extent, but these factors do not determine whether myelination will occur in general. Those factors are for example electrical activity, glutamate release, neuregulin signaling or interaction with extracellular matrix receptors of the integrin family (Stadelmann et al., 2019). Bechler et al. (2017) proposed a model considering both intrinsic and extrinsic factors. Based on their model, in a first intrinsic phase oligodendrocyte processes sense physical axon diameter and generate sheath length according to the caliber. The first phase is followed by the second adaptation phase marked by modification of the intrinsic myelin sheath regulated by extrinsic cues (Bechler et al., 2017).

To date, the question of how myelination patterns along axon are established is still a subject of controversial discussion. As described above evidence for both exist – that the axon and the oligodendrocyte determine the length and patterning of myelin sheaths. However, it remains determined how and when myelination pattern develop and whether and to what extent the oligodendrocyte or the axon – or both – decide about the final configuration of myelin sheath length to axon diameter and thereby decide about the action potential speed and timing.

1.2. THE MAMMALIAN SOUND LOCALIZATION CIRCUIT AS A MODEL SYSTEM FOR THE DEVELOPMENT OF MYELINATION

Neurons in the auditory brainstem involved in sound localization computations are some of the fastest and most precise neurons found in the mammalian brain. These auditory brainstem neurons exhibit remarkable adaptations to fulfil their exceedingly specific temporal demands (Grothe et al., 2010). Amongst others, the earlier mentioned specializations of GBC axons are crucial prerequisites for fast and precise action potential conduction (Ford et al., 2015). Hence, the sound localization circuit represents a well-suited model system to analyze the underlying structural adaptations that enable the remarkable speed of action potential transmission.

This section will provide an overview of how vertebrates detect the origin of spatial sound sources and will further give insights into the importance of specific structural adaptation, such as myelination patterns, in this system.

1.2.1. Sound transduction in the ear

When rapid changes of air pressure (sound waves) enter the ear, they induce oscillations of the tympanic membrane. The movement of the tympanic membrane sets the three middle ear bones into motion which in turn pass on the vibrations to the fluid filled cochlea. The resulting pressure fluctuations in the cochlea elicit oscillations of the basilar membrane of the cochlea (Fettiplace, 2017). The width and stiffness of the basilar membrane changes along its length resulting in a tonotopic organization, with high sound frequencies causing the strongest vibrations at the base and low frequencies causing the strongest vibrations at the apex of the basilar membrane (Bekesy, 1970). Sensory hair cells along the basilar membrane detect sound stimuli and convert the vibrations via mechanoeletrical transduction into electrical signals (Fettiplace, 2017). These electrical signals are conveyed via the auditory nerve in form of action potentials to the cochlea nucleus in the auditory brainstem (Grothe et al., 2010). Here, auditory nerve fibers innervate several types of neurons, some of which exhibit remarkably high temporal precision (Golding et al., 1995; Oertel, 1997; Oertel et al., 2000). For instance, spherical bushy cells (SBCs) and globular bushy cells (GBCs) in the cochlear nucleus (CN) transmit the information to the superior olivary complex (SOC) for sound localization computation before the sound information gets further processed in higher brain areas (Grothe et al., 2010).

In order to accurately determine the exact location of a sound source, central auditory neurons make use of several cues in parallel.
First, spectral cues are used to determine elevations and whether a sound is coming from in front or behind. These monoaural cues are particularly useful for locating sound sources in the vertical plane where they change most. Second, the auditory system utilizes binaural cues to localize sound sources in the horizontal plane by comparing differences in the movement of the two eardrums (Grothe et al., 2010). Two interaural differences are available for binaural analysis: the interaural level differences (ILDs) – the difference in sound intensity level at the two ears - and the interaural time differences (ITDs) - the difference in the time-of-arrival of a sound at the two ears (Rayleigh, 1907) (Figure 4).

1.2.2. Processing of interaural differences

Many mammals are able to use both of the binaural cues, ILDs and ITDs, to localize the origin of a sound source with a spatial accuracy of just a few degrees. For instance, humans can discriminate sound sources 1 – 2 degrees apart from each other (Grothe et al., 2010) and it was found that gerbils exhibit a similar ITD resolution (Lingner et al., 2018; Pecka & Encke, 2020; Tolnai et al., 2017).

ILDs are created when the sound is attenuated by the head (Rayleigh, 1907). The shadowing effect of the head causes different sound levels at the two ears with a reduced intensity at the ear farthest away from the sound source. ILDs are more pronounced at high sound frequencies and the magnitude of ILDs increase with increasing frequencies (Kandler et al., 2020). Large head sizes (e.g. humans) lead to a strong head shadowing effect and thus for small head sizes significant ILDs are predominantly induced only at higher frequencies (Tolnai et al., 2017). For gerbils, frequencies higher than 2 kHz creates increasingly sizable ILDs (Grothe et al., 2010).

ITDs describe the difference of arrival time between the sound signals at the two ears. When sounds do not arise directly from in front (or behind) they arrive earlier at one ear than at the other, creating an ITD. ITDs are mainly used to localize low frequencies sound sources that are not attenuated enough by the head to create ILDs. For frequencies below 2 kHz, information in the fine structure of the sounds is available for ITD processing in gerbils (Grothe et al., 2010; Grothe & Pecka, 2014).

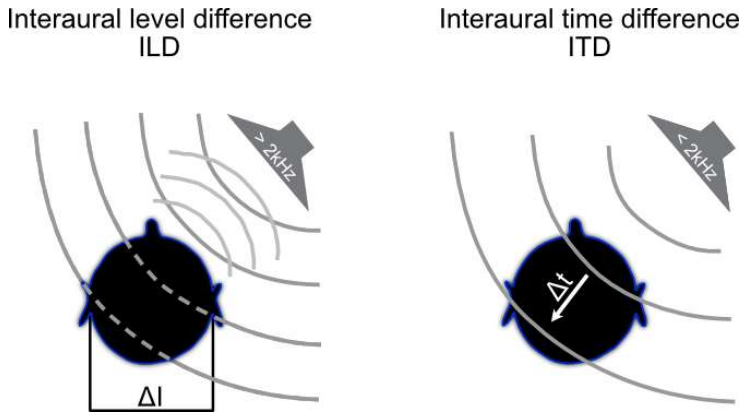

Figure 4: Processing of binaural cues. *Left:* Interaural level differences (ILDs) between the two ears are created by a shadowing effect of the head. ILDs are mainly used to localize high frequency sounds (> 2 kHz). *Right*: Interaural time differences (ITDs) occur when a sound arrives at one ear before the other and are used to localize predominantly low frequency sounds (< 2 kHz) (adapted from Grothe et al., 2010).

These binaural cues are processed separately by neurons in two specialized circuits of the SOC in the auditory brainstem. Individual neurons in the lateral and medial superior olive (LSO and MSO, respectively) assess the relative amplitude and timing between the two inputs. Computation in the LSO and MSO is based on precise interaction of glutamatergic excitation and glycinergic inhibition.

Encoding of ILDs by the LSO
The LSO best known for encoding ILDs (Tollin, 2003). Neurons in the LSO integrate excitatory (glutamatergic) inputs from SBCs in the ipsilateral anteroventral cochlear nucleus (AVCN) with inhibitory (glycinergic) inputs from the ipsilateral medial nucleus of the trapezoid body (MNTB). The MNTB itself is innervated by GBCs from the contralateral AVCN and by a giant synapse, the calyx of Held (Figure 5, *top*). In general, LSO neurons respond best to high frequencies at which ILDs are more pronounced (Kandler et al., 2020; Pecka & Encke, 2020). Nonetheless, also low-frequency LSO neurons have been identifies contributing to ITD coding (Lingner et al., 2018; Tolnai et al., 2017).

Encoding of ITDs by the MSO
The primary encoder for ITDs of sounds between the two ears is the MSO. Neurons in the MSO serve as coincidence detectors and are able to process microsecond differences in arrival time of primarily low-frequency sounds between the two ears. The MSO circuit shares the excitatory input from the ipsilateral AVCN and the contralateral-driven inhibitory input via the MNTB with the LSO circuit. In addition, the MSO circuit incorporates a second contralateral excitatory input from the AVCN and another inhibitory input from the ipsilateral lateral nucleus of the trapezoid body (LNTB) (Figure 5*, bottom*).

Although the processing of both binaural cues requires precise temporal accuracy, the low frequency circuit for ITD processing exceeds the temporal requirements for input timing of the ILD circuit. Contralateral inhibition from GBCs reliably precedes contralateral excitation in the MSO by a few hundreds of microseconds despite the additional synapse (Brand et al., 2002; Roberts et al., 2013). The importance of the precedence of inhibition is explained in more detail in the next section.
GBC axons involved in ITD processing exhibits remarkable adaptations to meet the temporal precision needed for computation of this binaural cue (Ford et al., 2015).

1.2.3. The GBC-to-MNTB connection: a central inhibitory pathway

The connection of GBCs to the MNTB is central part in mammalian sound localization circuits providing inhibitory inputs to neurons in the LSO and MSO. GBCs in the AVCN receive large axosomatic terminals directly from the auditory nerve (endbulbs

of Held) and, together with SBCs, are the first station of sound localization computation in the auditory brainstem. GBCs subsequently transmit auditory information along their thick and substantially myelinated axons to the contralateral MNTB where they make synaptic contact with principal neurons via the giant calyx of Held (Grothe et al., 2010; von Gersdorff & Borst, 2002). Here, MNTB cells convert the well-timed glutamatergic excitation into well-timed glycinergic inhibition to their main targets, the LSO and MSO. However, despite their similar role in detecting and computing interaural difference, the functional requirements for precise timing of this inhibitory pathway are different for the LSO and MSO circuit (Grothe et al., 2010).

The MNTB is tonotopically organized with those GBC axons that respond best to high frequency terminating onto neurons in the medial part of the MNTB (Figure 5, *light blue*) which innervate the LSO. In turn, those GBC axons that respond best to low frequencies terminate onto neurons in the lateral MNTB (Figure 5, *dark blue*) which provide prominent glycinergic inhibition to the MSO (Grothe et al., 2010). Here, inhibition must be precisely time for synaptic integration and coincidence detection. Glycinergic inhibition has been shown to tune the ITD sensitivity of MSO neurons *in viv*o and *in vitro* (Brand et al., 2002; Pecka et al., 2008; Myoga et al., 2014). Blocking the inhibition *in vivo* resulted in a broader ITD tuning of MSO neurons and a shift of the peak of ITD function towards the midline. Thus, glycinergic inhibition adjusts the maximal slope of ITD functions within the physiological range (Brand et al., 2002; Pecka et al., 2008). As mentioned earlier, contralateral MNTB-mediated inhibition precedes contralateral excitation and arrives earlier at MSO neurons. This precedence of inhibition relative to excitation lowers the spike probability and has been demonstrated to tune the ITD response function of MSO neurons (Brand et al., 2002; Pecka et al., 2008; Myoga et a., 2014), narrow the coincidence detection window and sharpen the precision of neurons in the MSO (Roberts et al., 2013).

In order to provide the earlier arrival time of inhibition at the MSO and ensuring fast and reliable transmission of sound source information, the inhibitory component of the circuits has incorporated numerous structural and functional adaptations. The probably most obvious characteristic is the size of the synapse, the calyx of Held, specialized for fast transmission at high rates with low jitter. The giant terminal forms a monosynaptic axosomatic connection onto the round, electrically compact postsynaptic principal neurons of the MNTB, enabling fast depolarization with a very short synaptic delay (Taschenberger & Von Gersdorff, 2000). Many active zones at the calyx (Dondzillo et al., 2010; Sätzler et al., 2002; Taschenberger et al., 2002; Wimmer et al., 2006) enable the release of more than 100 vesicles in response to a single action potential (Borst & Sakmann, 1996). In addition, GBC axons exhibit some of the largest diameters and are therefore some of the fastest conducting axons found in the vertebrate CNS (Kuwabara & Zook, 1991), allowing the transmission of signals as quickly as possible. Moreover, in addition to their large axon caliber, GBC axons

tuned to low frequencies exhibit unusual myelination patterns leading to unexpected small L/*d* ratios in turn enabling even higher conduction velocity and temporal precision (Ford et al., 2015).

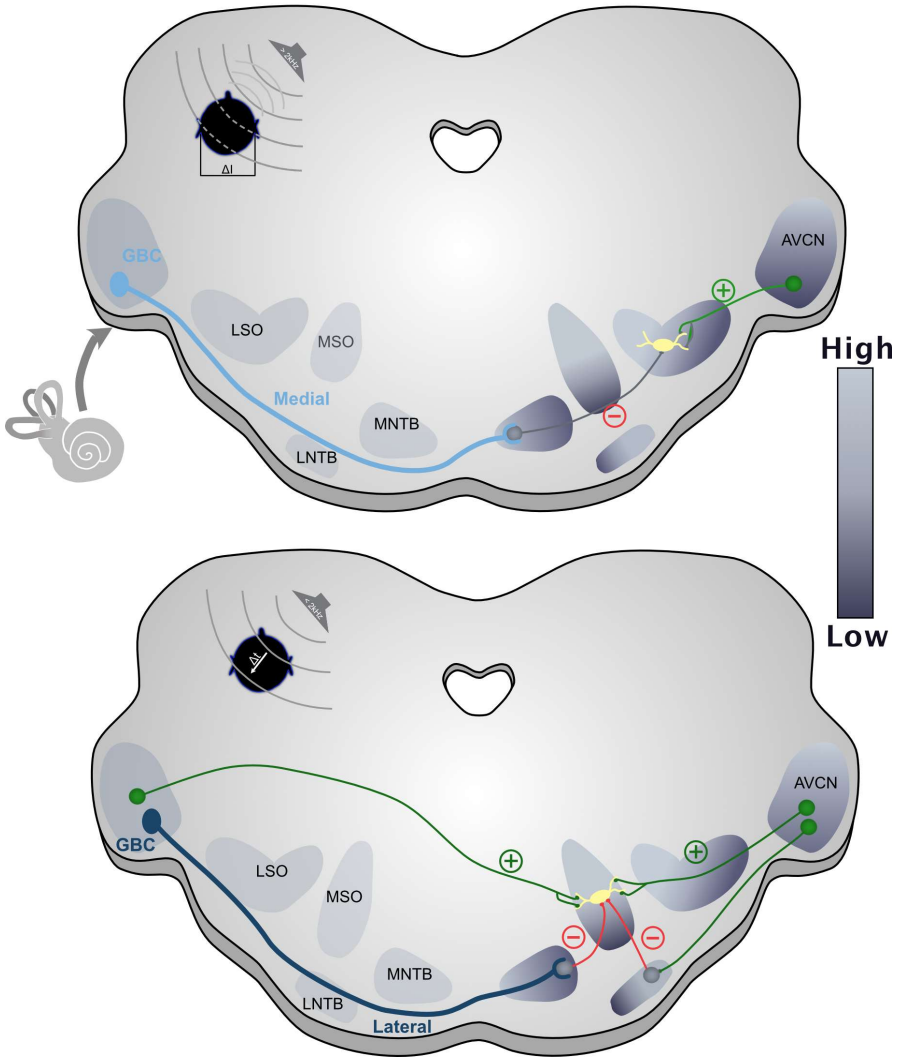

Figure 5: Sound Localization circuit in the auditory brainstem of the Mongolian gerbil. *Top*: tuned to high frequencies (> 2kHz, *light blue*) terminate medially in the tonotopically organized MNTB, making contact onto principal cells via a giant synapse, the calyx of Held. Here, the well-timed excitation is converted unto well-timed inhibition (*red*) and further transmitted to neurons in the LSO. Neurons in the LSO also receive direct excitation from the ipsilateral CN (*green*). *Bottom*: Circuit of interaural time differences (ITD). GBCs that are preferentially tuned to low frequencies (< 2 kHz, *dark blue*) make contact onto cells into the lateral part in the MNTB. From here, inhibition (*red*) is further transmitted to the MSO, which also receive inhibition from the ipsilateral LNTB, as well as direct excitation from the contralateral and ipsilateral CN (*green*). The spectrum on the right illustrates the frequency tuning of neurons in the distinct nuclei from high (*light gray*) to low (*dark gray*). GBCs, globular bushy cells; AVCN, anteroventral cochlear nucleus; LSO, lateral superior olive; MSO, medial superior olive; MNTB, medial nucleus of the trapezoid body; LNTB, lateral nucleus of the trapezoid body (inspired by Grothe et al., 2010).

1.3. AIM OF THE THESIS

The central aim of this thesis was to gain an in-depth understanding of the development of specific structural parameters of myelinated axons. In particular, the establishment of myelination patterns, axon diameter, L/*d* ratios and nodes of Ranvier has been the focus of interest. I approached this aim by using the sound localization circuit of the Mongolian gerbil (*Meriones unguiculatus*) as model system and took advantage of the differential GBC subpopulations that exhibit different structural adaptations along their myelinated axons.

First, I investigated whether the specific myelin and axon morphology of GBC axons involved in the ITD circuit provide the anatomic substrate for their required action potential conduction speed and timing. Given that neuronal processing of ITDs in the gerbil relies on exceptionally high input timing and ITDs can hardly be utilized as a binaural cue in mice, I compared the structural features of GBC axons between the two rodents to assess their functional relevance.

Second, an extensive developmental study was conducted to clarify when and how myelination patterns, axon morphology and nodes of Ranvier are established, and whether they develop in parallel or independently. By examining time points before and after the onset of hearing, I also aimed to gain insight into the role of sensory experience on the maturation of the above structures.

Finally, by understanding the developmental time course of myelin and axonal morphology establishment, I aimed to contribute to the controversial debate of who determines the relationship between myelin sheath length and axon diameter. Whether the oligodendrocyte or the axon, or both determine their final configuration.

Importantly, specific features and mechanisms involved in the central sound localization circuit in the auditory brainstem may reflect universal characteristics that could be present in other neuronal circuits and species as well.

2. INPUT TIMING FOR SPATIAL PROCESSING IS PRECISELY TUNED VIA CONSTANT SYNAPTIC DELAYS AND MYELINATION PATTERNS IN THE AUDITORY BRAINSTEM

2.1. AUTHOR CONTRIBUTIONS

Annette Stange-Marten[*], Alisha L. Nabel[*], James L. Sinclair, Matthew Fischl, Olga Alexandrova, Hilde Wohlfrom, Conny Kopp-Scheinpflug, Michael Pecka and Benedikt Grothe (2017). **Input timing for spatial processing is precisely tuned via constant synaptic delays and myelination patterns in the auditory brainstem**. PNAS 114(24), pp. 4851–4858. doi: 10.1073/pnas.1702290114.

[*]*these authors contributed equally*

The contributions of the authors Annette Stange-Marten (AS-M), Alisha L. Nabel (ALN), James L. Sinclair (JLS), Matthew Fischl (MF), Olga Alexandrova (OA), Hilde Wohlfrom (HW), Conny Kopp-Scheinpflug (CK-S), Michael Pecka (MP) and Benedikt Grothe (BG) to the study included in this thesis are as follows:

MP and BG designed the research; **ALN**, HW, OA performed and analyzed immunofluorescence in Figure 3. AS-M, JLS, MF performed *in vivo* measurements and *in vitro* electrophysiology; AS-M, OA, CK-S and MP analyzed data; MP and BG jointly supervised this work; and MP and BG wrote the paper.

Input timing for spatial processing is precisely tuned via constant synaptic delays and myelination patterns in the auditory brainstem

Annette Stange-Marten[a,1], Alisha L. Nabel[a,b,1], James L. Sinclair[a], Matthew Fischl[a], Olga Alexandrova[a], Hilde Wohlfrom[a], Conny Kopp-Scheinpflug[a], Michael Pecka[a,2], and Benedikt Grothe[a,2]

[a]Division of Neurobiology, Department Biology II, Ludwig-Maximilians-UniversitaetMunich, 82152Planegg-Martinsried, Germany; and [b]Graduate School of Systemic Neurosciences, Ludwig-Maximilians-Universitaet Munich, 82152 Planegg-Martinsried, Germany

Edited by Eric I. Knudsen, Stanford University School of Medicine, Stanford, CA, and approved May 8, 2017(received for review February 10, 2017)

Precise timing of synaptic inputs is a fundamental principle of neural circuit processing. The temporal precision of postsynaptic input integration is known to vary with the computational requirements of a circuit, yet how the timing of action potentials is tuned presynaptically to match these processing demands is not well understood. In particular, action potential timing is shaped by the axonal conduction velocity and the duration of synaptic transmission delays within a pathway. However, it is not known to what extent these factors are adapted to the functional constraints of the respective circuit. Here, we report the finding of activity-invariant synaptic transmission delays as a functional adaptation for input timing adjustment in a brainstem sound localization circuit. We compared axonal and synaptic properties of the same pathway between two species with dissimilar timing requirements (gerbil and mouse): In gerbils (like humans), neuronal processing of sound source location requires exceptionally high input precision in the range of microseconds, but not in mice. Activity-invariant synaptic transmission and conduction delays were present exclusively in fast conducting axons of gerbils that also exhibited unusual structural adaptations in axon myelination for increased conduction velocity. In contrast, synaptic transmission delays in mice varied depending on activity levels, and axonal myelination and conduction velocity exhibited no adaptations. Thus, the specializations in gerbils and their absence in mice suggest an optimization of axonal and synaptic properties to the specific demands of sound localization. These findings significantly advance our understanding of structural and functional adaptations for circuit processing.

myelination | synaptic transmission delay | sound localization | circuit processing | input timing

Temporal integration of bioelectrical signals via chemical synapses is fundamental to neuronal computations. During circuit processing, neuronal information transfer via action potentials is controlled by exact differences in the occurrence between excitatory and inhibitory inputs (1–5). The arrival time of inputs within circuits in turn is largely shaped by the conduction delay of action potentials along the axons and during synaptic transmission. During ongoing activity, the transmission delays of chemical synapses generally increase in the range of hundreds of microseconds due to short-term adaptations (6–9). However, because temporal integration on postsynaptic neurons usually operates on time scales in the range of milliseconds or even longer (10, 11), sluggishness arising from synaptic mechanisms and axonal conductance is negligible for most of these computations. There are, however, some essential neuronal processing tasks that challenge the temporal precision of our nervous system. For instance, weakly electric fish detect miniature changes in the frequency of a constant electrical field. The neuronal circuits in these animals use electrical instead of chemical synapses in the periphery as a rather unique solution to speed up signal propagation along the first synaptic stages and to allow for stable (i.e., activity invariant) synaptic delays (SDs) (12).

The temporally most precise neuronal computations known in mammals (including humans) occur in the auditory system in circuits processing sound location information (13, 14). Here, individual neurons in the lateral and the medial superior olive (LSO and MSO, respectively) detect coincidences between inputs from the two ears. In both nuclei, this computation is based on precise interactions of glutamatergic excitation and glycinergic inhibition (15, 16), and indeed a subset of the respective inputs is shared between the two circuits (17). One striking shared structural feature is the contralateral inhibitory pathway that is specialized for speed and reliability (Fig. 1A). Globular bushy cells (GBCs) in the cochlear nucleus excite glycinergic cells of the medial nucleus of the trapezoid body (MNTB) via highly myelinated and rapidly conducting axons and the giant calyx of Held synapse (18, 19). However, the functional requirements for precise timing of this inhibitory pathway are different for the LSO and MSO circuit: the LSO predominantly computes differences in the relative level of high-frequency sounds between the ears [interaural level difference (ILD)] and shows temporal input precision in the millisecond range for faithful level measurement (13, 20) (see also Discussion). In the MSO, on the other hand, microsecond differences in the time of arrival of low-frequency sounds at the two ears [interaural time difference (ITD)] are processed and consequently the requirements for input timing are exceptionally higher (5, 21). Importantly, because the inhibitory pathways involve an additional

Significance

Neural computation depends on precisely timed synaptic inputs, but the way that the timing of inputs is tuned to match postsynaptic processing requirements is not well understood. Here, we studied the same brainstem sound localization pathway in two species with dissimilar temporal processing requirements. Two factors that limit precise timing are synaptic delay and axonal conduction time. In gerbils, which depend on precise timing for sound localization, synaptic delays in fast conducting axons are stable across activity level, and axon myelination is adapted to minimize conduction delays. In mice, which do not depend on precise timing, these specializations are absent. Our results suggest that both axonal and synaptic properties are optimized to the specific functional requirements of neural computation, advancing our understanding of the mechanisms that optimize neural circuits.

Author contributions: M.P. and B.G. designed research; A.S.-M., A.L.N., J.L.S., M.F., O.A., and H.W. performed research; A.S.-M., O.A., C.K.-S., and M.P. analyzed data; M.P. and B.G. jointly supervised this work; and M.P. and B.G. wrote the paper.

The authors declare no conflict of interest.

This article is a PNAS Direct Submission.

Freely available online through the PNAS open access option.

[1]A.S.-M. and A.L.N. contributed equally to this work.

[2]To whom correspondence may be addressed. Email: grothe@lmu.de or pecka@bio.lmu.de.

This article contains supporting information online at www.pnas.org/lookup/suppl/doi:10.1073/pnas.1702290114/-/DCSupplemental.

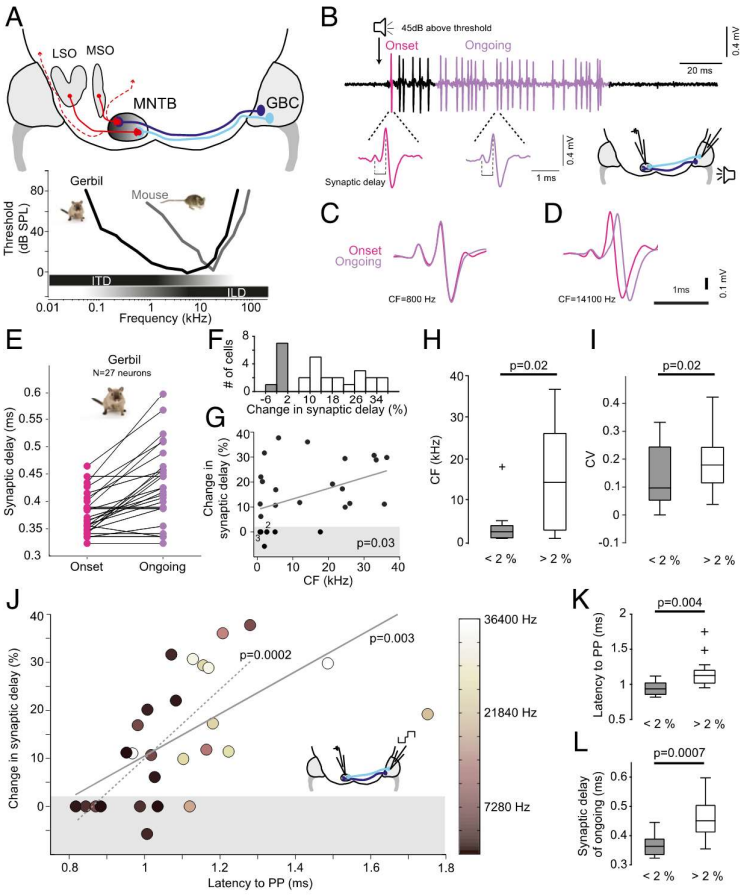

Fig. 1. Constant synaptic delays only in low-frequency-tuned, fast-conducting axons of gerbils. (A) Schematic of the mammalian sound localization circuits. Globular bushy cell (GBC) axons project to the contralateral medial nucleus of the trapezoid body (MNTB) to form one-to-oneconnections via the giant calyx of Held synapses. MNTB neurons then project to many brainstem and midbrain nuclei (dashed red lines), most importantly the lateral and medial superior olive (LSO and MSO, respectively) for binaural computation of sound source location: for high-frequency sounds, interaural level differences (ILDs) are analyzed in the LSO, whereas for low-frequency sounds—due to a lack of ILDs—interaural time differences (ITDs) are detected in the MSO. Both in gerbil and mouse, the MNTB is tonotopically organized with medially terminating GBC axons (light blue) tuned to higher, and laterally terminating axons (dark blue) tuned to lower frequencies. However, due to differences in the absolute hearing range (Bottom), the gerbil, but not the mouse, uses ITDs for sound localization. Typical frequency ranges of ITD and ILD processing are depicted by horizontal bars below the audiograms. (B) Representative example of sound-evoked responses of a single gerbil calyx-to-MNTB synapse/neuron (Upper trace). Below are blowups showing waveforms of the prepotential and the postsynaptic action potential to stimulus onset (pink) and to ongoing stimulus periods (purple). (C) Overlay of the waveforms recorded from a MNTB neuron tuned to low sound frequencies (CF = 800 Hz, the range where ITDs are used for sound localization), revealing identical synaptic delays (SDs) for onset (pink) and ongoing responses (purple). (D) Same display as in C for a neuron tuned to high sound frequencies (CF = 14,100 Hz), exhibiting the expected increase in SD. (E) Mean SD for onset (pink) and ongoing (purple) response plotted for each neuron recorded in the gerbil (n = 27). (F) Distribution of change in SD over the population of neurons (n = 27). Bins with stable SD (<2%) are denoted in gray. (G) The changes in SD significantly correlate (P = 0.03, Pearson correlation) with the postsynaptic MNTB neurons' CFs. Shaded area denotes stable SDs (changes <2%). (H) Neurons with stable SD (gray) show significantly lower CFs (P = 0.02, Mann-Whitney U test). Boxes indicate interquartile range with horizontal bar showing the median. Whiskers extend to the full data range, one outlier indicated by +. (I) Neurons with stable SD (gray) also had a significantly smaller coefficient of variation (CV) for ongoing SDs (P = 0.02, Mann-Whitney U test). Conventions are as in H. (J) Changes in SD strongly depend on the mean conduction latency of the presynaptic GBC axon (P = 0.003, Pearson correlation). The correlation did not depend on the two outliers with latencies > 1.4 ms (dotted line, P = 0.0002, Pearson correlation). The CFs of the postsynaptic MNTB neurons are color coded. The conduction latency was measured by electric stimulation of GBC axons (see schematic). (K and L) In neurons with SD changes <2%, conduction latencies and absolute ongoing SDs are significantly shorter (P = 0.004 and P = 0.0007, respectively, Mann-Whitney U test) than for neurons with SD changes >2%. Conventions are as in H.

synaptic stage compared with the excitatory inputs to the MSO, both absolute and constant relative timing represents a key challenge for this circuit (5, 15, 22–24): Compared with onset information (i.e., action potential firing after longer periods of inactivity) passing through rested and thus less adapted calyx of Held synapses, inhibition would be progressively delayed relative to the excitation during ongoing activity by dozens to hundreds of microseconds due to the increase in synaptic delay (25). This activity-dependent increase in the overall delay of inhibition relative to excitation would corrupt the microsecond precision of inputs required for ITD processing. However, both at the level of single MSO neurons (26) as well as in human psychoacoustics (27), ITD detection does not differ between onset and ongoing sound components.

In addition to this problem of activity-dependent relative timing, ITD processing in MSO neurons is confronted by adapting the absolute timing of the individual inputs originating from the distinct pathways of different axonal lengths (ipsilateral vs. contralateral) and number of synapses. For example, contralateral inhibition via the GBCs and MNTB has been found to reliably precede the contralateral excitation by a few hundred microseconds despite its additional synapse (5, 22). We recently revealed structural adaptations in axonal caliber and the myelination pattern of GBC axons of Mongolian gerbils, providing an anatomical substrate for the observed temporal precedence of the inhibitory pathway (28). Intriguingly, we also discovered pronounced differences in axonal and myelin morphology within subpopulations of GBC axons tuned to low frequencies: although thicker in axon caliber, these GBC neurons exhibit shorter internode length, resulting in significantly faster conductance velocity and enhanced action potential precision (28). However, the MNTB targets not only MSO but many different auditory nuclei (29), including the LSO. It is therefore unclear whether differential myelination patterning and conduction velocity are specific adaptations for ITD processing or simply represent a general variation related to tonotopic organization per se.

Here, we observed activity-invariant relative input timing and examined whether the unusual myelination pattern observed in GBC fibers tuned to low frequencies is specifically related to ITD processing. To this end, we compared GBC axon morphology and synaptic transmission delays at the calyx of Held both in the Mongolian gerbil (an ITD user) and in the mouse (a non-ITD user). We found that the specializations in myelination and conduction velocity are highly specific to the functional requirements of ITD processing. We further revealed that explicitly in low-frequency tuned, fast conducting axons, the calyx of Held to MNTB synapse exhibited activity-invariant and thus stable delays.

Results

First we addressed the question of how activity-dependent increases of the synaptic transmission delay affect the relative timing of inhibition via the MNTB during sound location processing. Such increases would be detrimental for ITD processing in the MSO, where the additional calyx of Held synapse in the contralateral inhibitory pathway would introduce fluctuating and large (compared with the range of ITDs) changes in timing relative to the direct contralateral excitatory inputs. To determine the maximal range of increases that are introduced during high activity levels, we first measured in vivo the SD in the calyx of Held synapse of GBCs targeting MNTB principle neurons (Fig. 1 A and B). To study the specificity to ITD processing, we obtained these data both in gerbils, which possess both a well-developed MSO and LSO for ITD and ILD processing in the low- and high-frequency range, respectively, and mice, which possess only high-frequency hearing and are non-ITD users. We performed extracellular in vivo recordings of presynaptic potentials from the calyx of Held and the postsynaptic MNTB action potential (Fig. 1B) in response to 100-ms sound stimulation at each neuron's characteristic frequency (CF, the sound frequency a neuron responded best to) and rate-saturating intensity (45 dB above the neurons' threshold). To identify maximal changes in SD, we compared the mean SD of the first synaptic event related to the onset of an acoustic stimulus ("onset response") with the mean SD in the ongoing response (>20 ms after the onset response, when changes in SD are fully saturated).

In the gerbil, most cells showed the expected obvious increases in SD in this comparison but, surprisingly, some neurons exhibited no change in SDs (Fig. 1 B–D). Across all 27 neurons tested, the average SD in the onset response was 385.62 ± 46.2 μs (mean ± standard deviation) compared with 439.6 ± 73.0 μs (mean ± standard deviation) in the ongoing response (Fig. 1E). However, roughly one third of the neurons/synapses (8/27) did not exhibit any measurable increase in SD (<2%, Fig. 1F). More detailed analysis revealed a significant correlation of change of SD and sound-frequency tuning ($P = 0.03$, Pearson correlation, Fig. 1G). Particularly, fibers/neurons with stable SD tended to be tuned to lower sound-frequencies (SD change <2%: median CF, 2.35 kHz, 6/8 neurons with CF <3 kHz; SD change >2%: median CF, 14.1 kHz, $P = 0.02$, Mann–Whitney U test, Fig. 1H), and also exhibited less SD variance [coefficient of variation (CV)] (Materials and Methods) throughout the ongoing response component itself (SD change <2%: median CV, 0.097; SD change >2%: median CV, 0.18, $P = 0.02$, Mann–Whitney U test, Fig. 1I). The amount of change in SD correlated with firing rate in response to a CF pure tone (Fig. S1). Importantly, however, overall firing rate was not correlated with frequency tuning and, therefore, independent from phase locking (Fig. S1).

Low-frequency hearing requires ITD processing for sound localization, but not all low-frequency neurons necessarily need to be involved in ITD processing. To better characterize the properties of the recorded SDs, we also determined the conduction latency of the GBC axons that innervated the MNTB neurons by direct electrical stimulation (Fig. 1J and ref. 28). We noticed that neurons with the shortest absolute conduction latency (measured between peak of the stimulus artifact and peak of the prepotential) exhibited the smallest change of SD in the gerbil ($P = 0.003$, Pearson correlation; Fig. 1J, solid line; the correlation further increased to $P = 0.0002$ if two outliers were excluded; Fig. 1J, dashed line). Specifically, the fibers with stable SDs had significantly shorter conduction latencies ($P = 0.004$, Mann–Whitney U test, Fig. 1K) and shorter absolute ongoing SDs ($P = 0.0007$, Mann–Whitney U test, Fig. 1L) compared with fibers with >2% change in SD.

Taken together, in the gerbil, a subgroup of approximately 30% MNTB synapses exhibited constant SDs. These neurons were characterized by comparably lower CFs, shorter axonal conduction latencies, and shorter absolute SDs.

These data suggest that particularly those GBC axons and calyx of Held synapses that are specialized for faster and less variant action potential conduction and transmission are involved in ITD processing within the MSO circuit, where microsecond input precision is crucial. To test this hypothesis, we next repeated the SD measurements in the mouse, which does not use ITDs and thus would not require the specializations we found in the gerbil. We again obtained extracellular single cell recordings from the MNTB using the identical experimental protocol as for the gerbil. Overall, we found a similar overall trend of increasing SD when comparing onset (385.6 ± 46.2 μs, mean ± standard deviation) to ongoing responses (439.6 ±73.0 μs, mean ± standard deviation, Fig. 2A). However, in stark contrast to the gerbil data, there was only one single synapse/neuron in the mouse showing a change of SD smaller than 2% (Fig. 2 B and C). Moreover, changes of SDs in the mouse did not correlate with sound-frequency tuning ($P = 0.85$, Pearson correlation, Fig. 2C) or firing rate (Fig. S1). To facilitate comparisons with the gerbil data, where approximately 30% of the neurons exhibited stable SDs (Fig. 1F), we also compared the CV for ongoing SDs between the 30% of cells with the lowest changes in SD (corresponding to <5.5% change) and the remaining 70% of cells (>5.5% change in SD). In contrast to the gerbil, we found no difference in SD variance for mice between these groups (SD change <5.5%: median CV, 0.13; SD change >5.5%: median CV, 0.13; $P = 0.9$, Mann–Whitney U test; Fig. 2D and Materials and Methods). Finally, firing rate did not correlate with sound-frequency tuning (Fig. S1). Thus, activity-dependent changes in SD in the MNTB of mice were homogeneous across CF. A significant subpopulation with stable SDs was absent.

We had previously established that low-frequency GBC fibers in gerbils exhibit an unusual myelination pattern compared with high-frequency tuned fibers (Fig. 3, replotted from ref. 28) that results in significantly faster conduction velocity. Our physiological results suggest that specializations found in low-frequency fibers are specific to ITD processing. We thus hypothesized that

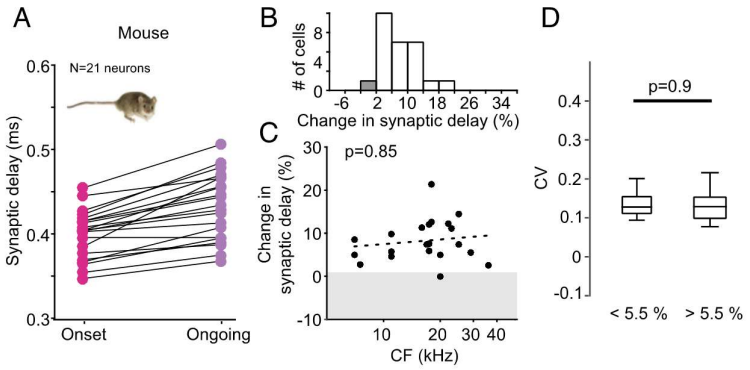

Fig. 2. Homogenouschangesin synaptic delay acrossfrequenciesin mice. (A) Mean SDsfor onset (pink) and ongoing (purple) responsesplotted for each neuron recorded in the mouse (n = 21). (B) Distribution of change in SD over the population of neurons. Convention as in Fig. 1. (C) The changes in SD do not correlate (P = 0.85, Pearson correlation) with the postsynaptic MNTB neurons' CFs. Shaded area denotesstable SDs(changes<2%). Only one neuron fallsinto thisgroup. (D) The coefficient of variation for the ongoing SDs is similar for all neurons irrespective of their change in SD (P = 0.9, Mann–Whitney U test). Conventions are as in Fig. 1H.

these morphological specializations might not be present in mouse GBC fibers. To address this question, we next compared myelination and fiber anatomy in low- and high-frequency GBC fibers in mice. We dye-filled GBC axons innervating the MNTB and counterstained against nodal and juxtaparanodal markers and then 3D-reconstructed single fibers starting from the calyx of Held synapse backward for multiple millimeters toward the GBC soma (Fig. 3A). We took advantage of the tonotopic arrangement of the MNTB and compared fibers terminating in the lateral third of the MNTB (GBClat, low frequency) to those terminating in the medial third of MNTB (GBCmed, high frequency) (Fig. 3B, Left). We quantified nodal and internodal axon diameter as well as internode length in five GBCmed and eight GBClat fibers (Fig. 3B, Right). Similar to our results from gerbils, the internode length in GBC fibers rapidly decreased close to the calyx of Held (Fig. 3G). However, mouse GBC fibers exhibited no significant differences in internodal axon diameter (mean ± SEM: GBCmed, 2.3 ± 0.1 μm; GBClat, 2.52 ± 0.08μm; P = 0.082, two-sided t test, Fig. 3C and D), node diameter (mean ± SEM: GBCmed, 1.58 ± 0.1 μm; GBClat, 1.5 ± 0.06 μm; P = 0.51, two-sided t test, Fig. 3E and F) and internode length in the steady state part (>450 μm from heminode, mean ± SEM: GBCmed, 258.8 ± 19.1 μm; GBClat, 273.7 ± 17.9 μm; P = 0.61, two-sided t test, Fig. 3 G and H). Accordingly, there was also no significant difference in length/diameter(L/d) ratio (mean ± SEM: GBCmed, 123.0 ± 7.2 μm; GBClat, 130 ± 8.8 μm; P = 0.58, two-sided t test, Fig. 3I and J). This finding is a remarkable contrast to the difference reported for GBCmed vs. GBClat values in the gerbil, which we obtained previously using identical methods and are depicted in Fig. 3 for comparison.

In gerbils, low-frequency/laterally terminating GBC fibers not only showed different myelination patterns but also significantly faster conductance velocity in vivo and in vitro (28). Therefore, we tested whether the lack of differences in GBC fibers in myelination in mice also correlated with a lack of difference in conduction velocity between GBClat and GBCmed axons. Electrical stimulation of GBC fibers at two different positions along the trapezoid tract (Fig. 3K, Left), causing pre- and postsynaptic events in the MNTB (Fig. 3K, Right), allowed us to measure absolute conduction speed in acute mouse brain slices (n = 24). In contrast to the gerbil, we found lateral ending fibers not to be faster than medially ending GBC fibers (Fig. 3L). In fact, faster fibers tended to terminate more medially (P = 0.09, Pearson correlation). Thus, in stark contrast to the gerbil, in the mouse, neither myelination patterning nor conduction speed showed any indication of specialized, faster conducting GBCs tuned to lower frequencies.

Together these data indicate that we have identified anatomical and physiological factors for the functionally specific tuning of temporally precise and stable tuning of inputs in circuit processing.

Discussion

The present study discovered structural and functional adaptations in the binaural auditory brainstem circuit. These adaptations facilitated stable and fast timing of inhibitory inputs via GBCs and the calyx of Held synapse onto MNTB glycinergic neurons. Most importantly, we revealed the presence of stable synaptic delays in a significant proportion of calyx of Held synapses in the gerbil, but not the mouse.

The GBC-to-MNTB pathway has already been known to incorporate a number of striking structural and functional adaptations for fast and reliable processing: the end bulb of Held (30, 31), superior phase locking in GBCs compared with their inputs (32), the calyx of Held giant synapse (18) and, discovered most recently, an unusual myelination pattern in GBCs tuned to lower frequencies associated with superior conductance velocity and temporal precision (28). We determined that in mice no such specializations in conduction velocity and precision were present, and mouse GBC axons conformed with standard internode length to axon caliber ratios irrespective of frequency tuning. We conclude that the inhibitory pathway involved in binaural processing of low-frequency sounds (<3 kHz) exhibits unique structural and functional adaptations for ultra-fast, precise, and temporally stable conduction and transmission as it is required for microsecond interaural time difference detection.

The presence of stable synaptic delays in a significant proportion of calyx of Held synapses in the gerbil appears to be a unique feature for chemical synapses in the central nervous system, at least to our knowledge. It is well established that chemical synapses, particularly the calyx of Held, rapidly adapt in transmission efficacy during ongoing activity (mice, rats, and gerbils) in vitro in acute brain slices (18, 33) as well as in vivo (34, 35). This adaptation is generally attributed to rapid changes in the available vesicle pool and calcium stores (36). One possible explanation for stable synaptic delays as described in the present study would be that these synapses resided in a highly pre-adapted stage, either through intrinsic mechanisms or due to constant high spontaneous activity (33). However, this seems unlikely to have been the case. First, probably due the choice of anesthetics, we encountered only little spontaneous activity that

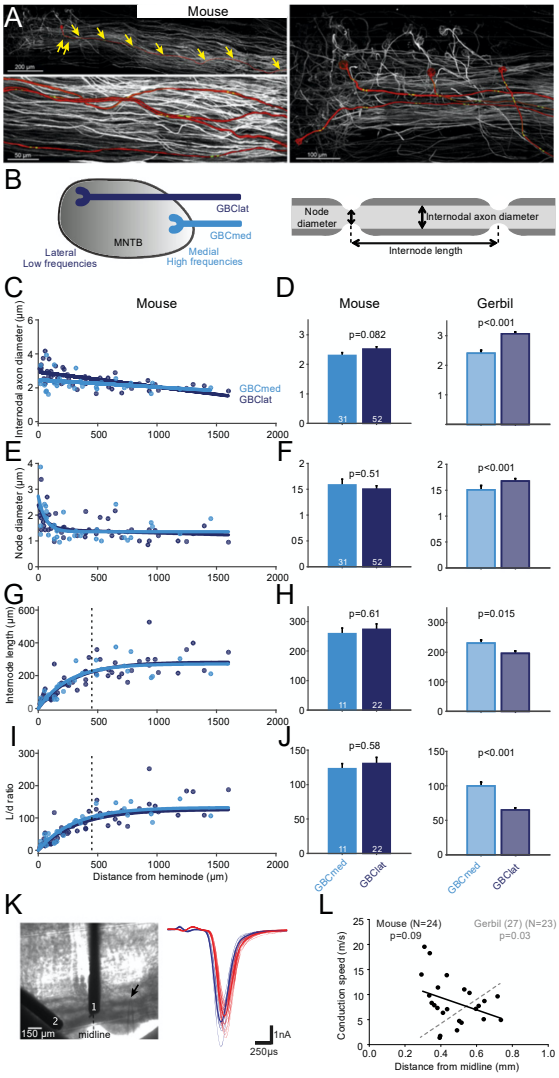

Fig. 3. Absence of structural and physiological specialization in mouse GBC axons. (A) Projections of confocal image stacks of mouse GBC axons innervating the MNTB filled with tetramethylrhodamine dextran. (Top, Left) One axon is highlighted in red and individual nodes of Ranvier are marked with yellow arrows. (Bottom, Left) Magnification of four axons; the position of juxtaparanodal (potassium Kv1.2) immunolabeled channels is shown in green. (Right) The tonotopic identity of axons was determined based on the relative position of calyces of Held along the mediolateral axis of the MNTB. (B) Schematic of the tonotopically organized MNTB (Left) and a myelinated axon illustrating the analyzed parameters (Right). (C, E, G, and I) Internodal axon diameter (C), node diameter (E), internode length (G), and internode length/internodal axon diameter (L/d) ratio (I) plotted against the distance from the heminode for lateral (GBClat, dark blue, n = 8 fibers) and medial (GBCmed, light blue, n = 5 fibers) terminating fibers. (D, F, H, and J) Averages of internodal axon diameter (D), node diameter (F), internode length (H), and L/dratio (J) in GBCmed and GBClat fibers of mouse (Left) and gerbil (Right) (replotted from ref. 28). Data are represented as mean ± SEM. P values are derived from two-sided t tests (number of data points is given in bars). Vertical dashed line in G and I denotes beginning of steady-state section of internode length. Only steady-state values were used for calculation of the average in H and J. In stark contrast to the gerbil, no differences in axon morphology and myelination patterning between medially and laterally ending GBC fibers are present in the mouse. (K) Conduction velocity of mouse GBC fibers was measured by electrical stimulation at two different positions along the trapezoid tract (1, 2: stimulation electrodes, arrow demarks recording electrode, Left), eliciting excitatory postsynaptic currents (EPSCs) in the MNTB in vitro (blue and red EPSCs were elicited by stimulation electrodes 1 and 2, respectively, Right). (L) The mean conduction speed of GBC axons (n = 24) plotted against the mediolateral position of their terminating region in the MNTB. There is no significant correlation for mouse (black regression line), contrasting earlier findings from the gerbil (replotted from ref. 28 in gray).

was insufficient to generate such highly adapted states. More importantly, chronic synaptic adaptation would have caused maximal increases in synaptic delays. However, the subpopulation of synapses with stable synaptic delays we found in the gerbil exhibited significant shorter absolute synaptic delays during the ongoing phase compared with the neurons with nonstable synaptic delays, and thus it is highly unlikely that stable synaptic delays were caused by saturated adaptation before the onset response.

It is further known that the state of a neural network and, hence, anesthesia per se can influence aspects of synaptic short-term plasticity (37). However, differential direct effects of different anesthetics (used for mouse and gerbil) on synaptic adaptations and on synaptic delays in particular, have, to our knowledge, not been reported. Indirect differential effects due to hypothermia (38, 39) can be excluded here because body temperature in both mice and gerbils was tightly controlled. More importantly, the coherent increase of synaptic delays in the ongoing response in both mice and gerbils, and the fact that a very specific subset of synapses in the gerbil showed constant synaptic delays, strongly contradicts any differential effects due to anesthesia.

Insight into the potential mechanisms underlying stable synaptic delays in the MNTB may come from the ribbon synapse of inner hair cells, the only mammalian chemical synapse that also shows stable synaptic delays. Here it is well established that the unusual arrangement of vesicles in the ribbon and specialized proteins are required for fast docking and efficient exocytosis (40, 41). Moreover, specific short-latency calcium channels have been suggested to be involved in allowing rapid vesicle release also in the ongoing response (42) as well as calcium-induced calcium release from specific internal stores (43). Such mechanisms are likely to also play a role in the central nervous system including the MNTB (44). Differential calcium buffering has been suggested for lateral vs. medial calyx of Held synapses, which resulted in larger excitatory postsynaptic currents (EPSCs) in lateral MNTB neurons and might also contribute to more stable transmission in ongoing responses described in this present study (45). Additionally, an elevated state of release probability of synaptic vesicles, recently shown for the onset events in MNTB (46), may also be available in the ongoing response in neurons tuned to lower frequencies of the gerbil. However, because most research on the calyx of Held had been performed in mice or rats but not in ITD-using animals like gerbils (47) or guinea pigs (48), one can only speculate how constant synaptic delays are achieved in the subpopulation described above. A recent study even points to the importance of extracellular matrix, which can be found in the auditory brainstem and midbrain, for rapid synaptic release in the MNTB (49, 50). In any case, a multicausal explanation seems likely.

Functionally, stable synaptic delays seem to represent a specific adaptation for faithful ITD processing, because it would prevent fluctuations in the relative timing of direct excitation and indirect inhibition for responses to onsets vs. ongoing sounds in the range of tens to hundreds of microseconds. Such fluctuations may be negligible for most neuronal computations, but not for microsecond ITD processing of low-frequency sounds.

We have previously shown that in the MSO, ITD sensitivity for onset and ongoing is similar, which corroborates the idea that stable SDs are of functional importance for ITD processing (26). We and others have shown that the onset ITD dominates both perception as well as MSO processing if sharp rising transients are present in the envelope, which is the case for most natural sounds (51, 52). The importance of stable SD is, however, not limited to onset vs. ongoing responses: any changes in the activity level within tens of milliseconds will affect the synaptic delay (figure 5 in ref. 24). This effect is best demonstrated by comparing the onset and ongoing response components during our pure tone stimulation, but not limited to it, as the evaluation of CV for the ongoing SDs has shown, providing further evidence for the functional importance of constant synaptic delays for ITD processing.

Accordingly, stable synapses were, on average, tuned to low sound frequencies, had the shortest conduction latencies, and were characterized by minimal absolute synaptic delays. Most importantly, such synapses were lacking in an animal that does not hear low frequencies and does not use ITDs—the mouse. Whereas the correlation of constant synaptic delays and tuning to low-frequency sounds for the gerbil data were significant, a few high-frequency neurons also had constant synaptic delays and, conversely, a few low-frequency neurons did not. This spreading in the data may be accounted for by the functional variability of the system: Firstly, the MNTB neuron's target not only LSO and MSO (15, 53–56), but also neurons in the superior paraolivary region (54, 57), and the monaural nuclei of the lateral lemniscus (57–59). Moreover, low-frequency LSO neurons exhibit trough-type ITD sensitivity, which has only small response modulation within the physiological range of ITDs and mainly in the periphery of auditory space (60). Hence, subpopulations of the low-frequency MNTB cells contribute to a variety of circuits and computations that do not require submillisecond timing precision. Secondly, mammals that developed low-frequency ITD processing can also detect ITDs in the envelope of high-frequency sounds, albeit to a lesser extent and with inferior accuracy (13, 51, 61). Thus, a subgroup of high-frequency tuned neurons in the gerbil involved in ITD processing is actually not unexpected.

There is good evidence from gerbils that inhibitory inputs to the MSO via the MNTB precede the direct excitatory input originating at the same contralateral cochlear nucleus (5, 22), which is remarkable, given that the inhibitory pathway involves the additional calyx of Held synapse. Recently we showed that the inhibitory pathway conquers this challenge via a two- to threefold thicker axon diameter of GBCs compared with the spherical bushy cells, which comprise the excitatory input (28). Moreover, we revealed the presence of a dramatic decrease of internode length toward the terminal region in both fiber classes. Our present study clarifies that this decrease is a universal feature (at least) of GBC fibers irrespective of species, as a similar decrease in internode length was also found in the mouse. We also previously established that gerbil GBC fibers tuned to low frequencies exhibited an unusual myelination pattern that strongly deviated from the canonical concept of constant internode length to axon diameter ratios of ~100. Although even thicker in axon caliber than high-frequency fibers, these axons exhibit shorter internode length, resulting in internode length/diameter ratios of only ~60 (Fig. 3 and ref. 28). It remained unclear, however, whether this unusual structural feature relates to relative low frequencies within the tonotopic organization of the auditory pathway per se or specifically to absolute low-frequency hearing. The fact that we found "normal" myelination patterns throughout the tonotopic axis in the mouse strongly suggested the latter and thus identifies the morphological specializations in gerbils as adaptations that are specific to ITD processing. It follows that a preceding of inhibition relative to excitation might be of crucial relevance for the computation of ITDs (5, 26). Although the exact way the different MSO inputs are integrated to realize ITD resolution of about 30 μs on a single cell level is still highly controversial (22, 62–64), there is evidence for extraordinary temporal precision of the glycinergic MNTB input to the MSO including an experience-driven developmental selection of very few but strong inputs that show fast inhibitory postsynaptic currents (IPSCs)/inhibitory postsynaptic potentials (IPSPs). Our findings of morphological and physiological specializations in the inhibitory pathway strongly corroborate that not only fast, but precisely timed inhibition to the MSO is of central importance for the ITD processing mechanism.

Materials and Methods

All experiments were approved in accordance with the stipulations of the German animal welfare law (Tierschutzgesetz) (AZ 55.2-1-54.2531.8-211-10). Animals were housed in groups of four to six individuals with 12-h light/dark cycles.

Depending on normality of the distribution, population average data are shown by the mean ± SEM, or the median and the 25% and 75% confidence intervals as box edges with full data ranges depicted by whiskers. Accordingly, parametric or nonparametric tests were used to determine statistical significances. No blinding was done for data analysis; however, identical automated code was used for analysis of all data.

In Vivo Measurements of Synaptic Delays in MNTB and GBC Latency. Identification of MNTB neurons and their GBC input during recordings was assured by the fact that voltage volleys ("prepotentials") were observed preceding the postsynaptic action potential for all neurons included in the dataset. Prepotentials are generated by the giant calyx of Held and thus a clear characteristic of MNTB recordings (65, 66). Likewise, the fact that MNTB neurons receive their calycal input only from GBCs positively identified the anatomical identity of the recorded neurons and presynaptic partner (19, 67, 68).

Gerbil. Methods for part of the dataset were described in detail previously (28). In short, 14 adult [postnatal age (P) 60–120] Mongolian gerbils (Meriones unguiculatus) of both sexes were initially anesthetized with an i.p. injection (0.5 mL/100g body weight) of a mixture of ketamine (20%) and xylazine (2%) diluted in 0.9% NaCl solution. During recording, animals were injected continuously with the same anesthesia via an automatic pump (801 Syringe Pump, Univentor) at a pump rate of 1.6–2.5 μL/min depending on body weight and state of anesthesia, which was measured using the toe pinch reflex. Each animal was mounted in a custom-made stereotaxic instrument (69) that was located in a sound-attenuated chamber, and constant body temperature was maintained at 37 °C. The MNTB was accessed by a craniotomy lateral to the midline above the lambda suture, and the anterior ventral cochlear nucleus (AVCN) by a craniotomy lateral to the midline caudal to the posterior aspect of the transverse sinus. After recording, the animal was killed with pentobarbital (20 mg/mL).

Neurons in the MNTB were acoustically and electrically stimulated and single-unit responses were recorded extracellularly with glass electrodes (3–37 MΩ) filled with 3 M KCl. Recordings were preamplified (patch clamp EPC 10 USB, HEKA), filtered (Humbug 50/60Hz noise eliminator, Quest Scientific), and fed to a computer via a Multi I/O processor (RZ6, Tucker-Davies Technology). The voltage traces were digitized at a sampling rate of 48 kHz and band-pass filtered (0.4–6 kHz). Only neurons with characteristic complex waveforms, consisting of a prepotential and a postsynaptic spike as typical for the MNTB were included.

Acoustic stimuli were digitally generated at a sampling rate of 200 kHz by TDT System III (Tucker-Davies Technology), digitally attenuated, and converted to analog signals (RZ6, Tucker-Davies Technology), and then delivered to earphones (ER 4PT, Etymotic Research). Responses to monaural stimulation with pure tones (100-ms duration plus 5-ms cosine rise/fall time) of predefined frequency/intensity combinations (6 intensities and 9 frequencies, >5 repetitions) were used to determine the CF of the MNTB neuron. Subsequently, pure tones (100-ms duration plus 5-ms cosine rise/fall time) at CF and 11 different sound intensities (5 dB below to 45 dB above threshold, at least 15 repetitions), with 120-ms interstimulus interval were presented to measure SD. The mean SD of the first spike of each repetition was compared with the mean SD of the ongoing spikes at a sound intensity of 45 dB above threshold. Only spikes occurring >20 ms after the initial response were included into the calculation of the mean ongoing SD, as the increase in SD is maximally saturated at this time (25). Values are shown as mean and used to calculate the relative change in synaptic delay. The CV of the ongoing response was calculated by dividing the SD of SDs for all spikes occurring >20 ms (for the 4 highest intensities recorded) by the mean SD. Electric stimuli were biphasic cathodic leading current pulses (120 μs per phase, 40-μs

interphase gap, 2 Hz repeat rate, 0–40 μA amplitude in 2-μA steps, >10 repetitions), that were digitally generated at a sampling frequency of 25 kHz and passed to the electrode channels (RX7-2 stimulator base station and MS16 stimulus isolator, Tucker-Davies Technology) of a 16-channel tungsten electrode microwire array (Omnetics-based electrodes, Tucker-Davies Technology). The time period between the peak of the stimulation artifact and the peak of the prepotential was measured to calculate the axonal action potential propagation latency.

Data analysis was performed by custom-made code in Matlab (Mathworks). Mouse. Five CBA/J mice (P92–P105) of both sexes were used for in vivo recordings. The mice were anesthetized with a s.c. injection of 0.01 mL/g medetomidine-midazolam-fentanyl (MMF) (0.5 mg/kg body weight medetomidine, 5.0 mg/kg body weight midazolam, and 0.05 mg/kg body weight fentanyl). Depth of anesthesia was measured using the toe pinch reflex and responding animals were given supplemental MMF at one-third the initial dose. Anesthesia was maintained using this method for the duration of the experiment. The mice were placed in an experimental setup identical to that described for the gerbils. To access the MNTB, a craniotomy was performed at the rostrocaudal midpoint of the interparietal skull plate lateral to the midline and extracellular responses were recorded with glass electrodes (5–20 MΩ) filled with 3 M KCl. Signals were amplified (Neuroprobe Amplifier Model 1600, A-M Systems), filtered (300–3,000 Hz; Tucker-Davies Technology model PC1) and recorded (~50-kHz sampling rate) with an RZ6 processor (Tucker-Davies Technology) and SPIKE software (Brandon Warren, V. M. Bloedel Hearing Research Center, University of Washington, Seattle, WA). Acoustic stimuli were digitally generated as described for gerbil with SPIKE software and then delivered to earphones (MF1, Tucker-Davies Technology). After recording, the animal was killed with pentobarbital (20 mg/mL). Data for synaptic delay measures were collected and analyzed in a way identically to that described for gerbils. The CV of the ongoing response was calculated by dividing the SD of SDs for all spikes occurring >20 ms by the mean SD.

In Vitro Measurements of Axonal Conduction Velocity. Sixteen CBA/Ca mice of either sex (P16–P35) were anesthetized with isoflurane and killed by decapitation. Coronal brainstem sections (200 μm thick) containing the superior olivary complex were cut in an ice-cold high-sucrose, low-sodium artificial cerebral spinal fluid (ACSF) as previously reported (70). Brainstem slices were maintained after slicing in normal ACSF at 37 °C for 30–45 min, after which they were stored in a slice-maintenance chamber at room temperature (~22 °C). Composition of the normal ACSF (in millimoles): 125 NaCl, 2.5 KCl, 26 $NaHCO_3$, 10 glucose, 1.25 NaH_2PO_4, 2 sodium pyruvate, 3 myo-inositol, 2 $CaCl_2$, 1 $MgCl_2$, and 0.5 ascorbic acid, pH = 7.4, bubbled with 95% O_2 and 5% CO_2. For the low-sodium ACSF, $CaCl_2$ and $MgCl_2$ concentrations were 0.1 and 4 mM, respectively, and NaCl was replaced by 200 mM sucrose. Experiments were conducted at 36 ± 1 °C, maintained by an inline feedback temperature controller and heated stage (TC344B, Warner Instruments) with the recording chamber being continuously perfused with ACSF at a rate of 1–2 mL·min^{-1}. Whole-cell patch-clamp recordings were made from visually identified MNTB neurons (Olympus BX51WI microscope) using an EPC10/2HEKA amplifier, sampling at 50 kHz, and filtering between 2.9 and 10 kHz. Patch pipettes were filled with a patch solution containing (in millimoles): 126 K-gluconate, 4 KCl, 40 Hepes, 5 EGTA, 1 $MgCl_2$, 5 Na_2 phosphocreatine, 0.2% biocytin, and 292 mOsm, (all chemicals from Sigma-Aldrich), pH = 7.2. Electrode resistance was between 2.4 and 6 MΩ. Synaptic potentials were evoked by afferent fiber stimulation with two concentric bipolar electrodes (FHC, Inc.) pushed gently onto the surface of the trapezoid body, one over the midline and another on the contralateral side to the recording patch electrode near the LSO. The latencies of responses were compared and used to calculate conduction speed (28). Voltage pulses were generated by the HEKA amplifier and postamplified by a linear stimulus isolator (PulseStimulator AM-2100). The contralateral electrode was moved around the slice to attain the lowest voltage threshold for stimulation. Latencies for the conduction speed measurements were obtained from the onset of the stimulus artifact to the half-maximum of the postsynaptic response. For each cell, a minimum of nine EPSCs was obtained from each electrode to generate a mean value for EPSC latency in response to stimulation at threshold. Only EPSCs greater than 1 nA were considered calyceal and used for analysis. No explicit information about the caliber size of the stimulated axons was obtainable. However, the largest caliber axons within the trapezoid body have previously been shown to be the GBC axons, which provide MNTB input (71, 72). The distance between the tip of the recording electrode and the midline of the slice and the distance between the tip of the recording electrode and the stimulation electrodes were measured using ImageJ (73).

The conduction speed data here form part of a dataset examining the development of conduction of trapezoid body fibers in mouse.

In Vitro Axon Tracing. Five CBA/Ca mice both sexes aged P25–P30 were deeply anesthetized with pentobarbital (2 mg/kg body weight) and intracardially perfused with ice-cold Ringer's solution containing heparin. After decapitation, the brainstem was quickly removed from the skull under ice-cold ACSF comprising (in millimoles): 125 NaCl, 2.5 KCl, 1 $MgCl_2$, 2 $CaCl_2$, 10 glucose, 1.25 NaH_2PO_4, 26 $NaHCO_3$, 0.5 ascorbic acid, 3 myo-inositol, and 2 pyruvic acid (all chemicals from Sigma-Aldrich). For anterograde tracing of GBC axons, borosilicate micropipettes with a tip diameter of 10–15 μm were filled with a 10% solution of tetramethylrhodamine dextran (3,000 molecular weight; Invitrogen D-3308) and visually guided to the AVCN in brainstem explants using a stereomicroscope. Tracer was pressure injected (15 pounds per square inch) into the GBC area of the AVCN using a picospritzer (Picospritzer III, Parker), followed by several electroporation pulse trains (50-ms pulses at 50 V and 10-Hz repetition rate) using an isolated pulse stimulator (A-M Systems). Subsequently, the explants were transferred to a chamber with oxygenated ACSF and incubated for 2.5 h at room temperature to allow for homogeneous distribution of the tracer in axons. Thereafter, the brainstems were immersion fixed for 2 h at room temperature, and followed overnight at 4 °C in 4% paraformaldehyde solution.

Immunohistochemistry and Confocal Microscopy. Brainstems were sectioned coronally at 120 μm using a vibratome slicer. Immunostaining was carried out as described (28). Primary antibodies for Kv1.2 (NeuroMab; 75-008 clone K14/16; mouse IgG2b; 1:500) and corresponding secondary antibodies (donkey anti-mouse Alexa-488, Dianova) and Fluorescent Nissl BlueTracer (Invitrogen) were applied. Confocal optical sections were acquired with a Leica TCS SP5-2 confocal laser-scanning microscope (Leica Microsystems) equipped with HCX PL APO X63/numerical aperture 1.3 glycerol 37 °C objective. Fluorochromes were visualized with excitation wavelengths of 405 nm (emission filter, 410–430 nm) for Nissl Blue, 488 nm (emission filter, 510–540 nm) for Alexa-488, 561 nm (emission filter, 565–585 nm) for tetramethylrhodamine dextran. Overlapping stacks of images were acquired from coronal brainstem slices (120 μm thick) at the level of the trapezoid body in the area spanning the MNTB and the contralateral tracer injection site (cochlear nucleus); voxel size: 482 × 482 × 290 nm. Red-green-blue (RGB) stacks, montages of RGB optical sections, and maximum-intensity projections were assembled using the ImageJ 1.37 k plugins and Adobe Photoshop 8.0.1 (Adobe Systems) software. GBC fibers were identified by calyces of Held that terminated in the contralateral MNTB and then back tracked across sections toward the cochlear nucleus. On the basis of their exact site of termination in the MNTB, GBC axons were classified as being either medially or laterally terminating. MNTB borders were determined using a counterstain (fluorescent Nissl stain). Morphometric analysis was carried out as described before for gerbil GBC axons (28).

ACKNOWLEDGMENTS. The authors thank Marc C. Ford for discussions and assistance with morphological data analysis. This work was supported by the German Research Association (DFG) Collaborative Research Center (870, B02 to B.G. and M.P. and A10 to C.K.-S.) and Priority Program (1608 to M.P.).

1. Sun YJ, et al. (2010) Fine-tuning of pre-balanced excitation and inhibition during auditory cortical development. Nature 465:927–931.
2. Wehr M, Zador AM (2003) Balanced inhibition underlies tuning and sharpens spike timing in auditory cortex. Nature 426:442–446.
3. Pecka M, Han Y, Sader E, Mrsic-Flogel TD (2014) Experience-dependent specialization of receptive field surround for selective coding of natural scenes. Neuron 84:457–469.
4. Pouille F, Scanziani M (2001) Enforcement of temporal fidelity in pyramidal cells by somatic feed-forward inhibition. Science 293:1159–1163.
5. Brand A, Behrend O, Marquardt T, McAlpine D, Grothe B (2002) Precise inhibition is essential for microsecond interaural time difference coding. Nature 417:543–547.
6. Barrett EF, Stevens CF (1972) The kinetics of transmitter release at the frog neuromuscular junction. J Physiol 227:691–708.
7. Katz B, Miledi R (1965) The measurement of synaptic delay, and the time course of acetylcholine release at the neuromuscular junction. Proc R Soc Lond B Biol Sci 161:483–495.
8. Wu LG, Borst JG (1999) The reduced release probability of releasable vesicles during recovery from short-term synaptic depression. Neuron 23:821–832.
9. Fedchyshyn MJ, Wang L-Y (2007) Activity-dependent changes in temporal components of neurotransmission at the juvenile mouse calyx of Held synapse. J Physiol 581:581–602.
10. Stuart GJ, Spruston N (2015) Dendritic integration: 60 years of progress. Nat Neurosci 18:1713–1721.
11. Krächan EG, Fischer AU, Franke J, Friauf E (2017) Synaptic reliability and temporal precision are achieved via high quantal content and effective replenishment: Auditory brainstem versus hippocampus. J Physiol 595:839–864.

12. Sawtell NB, WilliamsA, Bell CC(2005)From sparksto spikes:Information processingin the electrosensory systemsof fish. Curr Opin Neurobiol 15:437–443.
13. Grothe B, Pecka M, McAlpine D (2010)Mechanismsof sound localization in mammals. Physiol Rev 90:983–1012.
14. Golding NL, Oertel D (2012) Synaptic integration in dendrites: Exceptional need for speed. J Physiol 590:5563–5569.
15. Grothe B, Sanes DH (1994) Synaptic inhibition influences the temporal coding properties of medial superior olivary neurons: An in vitro study. J Neurosci 14:1701–1709.
16. Boudreau JC, Tsuchitani C (1968) Binaural interaction in the cat superior olive S segment. J Neurophysiol 31:442–454.
17. Grothe B, Pecka M (2014) The natural history of sound localization in mammals: A story of neuronal inhibition. Front Neural Circuits 8:116.
18. von Gersdorff H, Borst JGG (2002) Short-term plasticity at the calyx of Held. Nat Rev Neurosci 3:53–64.
19. Smith PH, Joris PX, Carney LH, Yin TC (1991) Projections of physiologically characterized globular bushy cell axonsfrom the cochlear nucleusof the cat. J Comp Neurol 304:387–407.
20. Tollin DJ (2003) The lateral superior olive: A functional role in sound source localization. Neuroscientist 9:127–143.
21. Grothe B (2003) New roles for synaptic inhibition in sound localization. Nat Rev Neurosci 4:540–550.
22. Roberts MT, Seeman SC, Golding NL (2013) A mechanistic understanding of the role of feedforward inhibition in the mammalian sound localization circuitry. Neuron 78: 923–935.
23. Roberts MT, Seeman SC, Golding NL (2014) The relative contributions of MNTB and LNTB neurons to inhibition in the medial superior olive assessedthrough single and paired recordings. Front Neural Circuits 8:49.
24. JorisPX, Smith PH (2008)The volley theory and the spherical cell puzzle. Neuroscience 154:65–76.
25. Tolnai S, Englitz B, Scholbach J, Jost J, Rübsamen R (2009)Spike transmission delay at the calyx of Held in vivo: Rate dependence, phenomenological modeling, and relevance for sound localization. J Neurophysiol 102:1206–1217.
26. Pecka M, Brand A, Behrend O, Grothe B (2008)Interaural time difference processing in the mammalian medial superior olive: The role of glycinergic inhibition. J Neurosci 28:6914–6925.
27. Blauert J (1997)Spatial Hearing: The Psychophysicsof Human Sound Localization (MIT Press, Cambridge, MA).
28. Ford MC, et al. (2015)Tuning of Ranvier node and internode propertiesin myelinated axons to adjust action potential timing. Nat Commun 6:8073.
29. Kulesza RJ, Jr, Grothe B (2015)Yes, there isa medial nucleus of the trapezoid body in humans. Front Neuroanat 9:35.
30. Pliss L, Yang H, Xu-Friedman MA (2009) Context-dependent effects of NMDA receptors on precise timing information at the endbulb of Held in the cochlear nucleus. J Neurophysiol 102:2627–2637.
31. Yang H, Xu-Friedman MA (2009)Impact of synaptic depression on spike timing at the endbulb of Held. J Neurophysiol 102:1699–1710.
32. Joris PX, Carney LH, Smith PH, Yin TC (1994) Enhancement of neural synchronization in the anteroventral cochlear nucleus. I. Responses to tones at the characteristic frequency. J Neurophysiol 71:1022–1036.
33. Hermann J, Pecka M, von Gersdorff H, Grothe B, Klug A (2007) Synaptic transmission at the calyx of Held under in vivo like activity levels. J Neurophysiol 98:807–820.
34. Englitz B, Tolnai S, Typlt M, Jost J, Rübsamen R (2009) Reliability of synaptic transmission at the synapsesof Held in vivo under acoustic stimulation. PLoS One 4:e7014.
35. Kopp-Scheinpflug C, Lippe WR, Dörrscheidt GJ, Rübsamen R (2003) The medial nucleusof the trapezoid body in the gerbil ismore than a relay: Comparison of pre-and postsynaptic activity. J Assoc Res Otolaryngol 4:1–23.
36. Borst JGG, Soria van Hoeve J (2012)The calyx of Held synapse:From model synapse to auditory relay. Annu Rev Physiol 74:199–224.
37. Reig R, Sanchez-Vives MV (2007) Synaptic transmission and plasticity in an active cortical network. PLoS One 2:e670.
38. Hume AL, Durkin MA (1986) Central and spinal somatosensory conduction times during hypothermic cardiopulmonary bypassand some observationson the effectsof fentanyl and isoflurane anesthesia. Electroencephalogr Clin Neurophysiol 65:46–58.
39. Charlet de Sauvage R, da Costa DL, Erre JP, Aran JM (1996) Changes in CM and CAP with sedation and temperature in the guinea pig: Facts and interpretation. Hear Res 102:15–27.
40. Wichmann C, Moser T (2015) Relating structure and function of inner hair cell ribbon synapses. Cell Tissue Res 361:95–114.
41. Trapani JG, Obholzer N, Mo W, Brockerhoff SE, Nicolson T (2009) Synaptojanin1 is required for temporal fidelity of synaptic transmission in hair cells. PLoS Genet 5: e1000480.
42. Zampini V, et al. (2013) Burst activity and ultrafast activation kinetics of CaV1.3 Ca^{2+} channelssupport presynaptic activity in adult gerbil hair cell ribbon synapses.J Physiol 591:3811–3820.
43. Castellano-Muñoz M, Ricci AJ (2014) Role of intracellular calcium stores in hair-cell ribbon synapse. Front Cell Neurosci 8:162.
44. Lin KH, Taschenberger H, Neher E (2017) Dynamics of volume-averaged intracellular Ca(2+) in a rat CNS nerve terminal during single and repetitive voltage-clamp depolarizations. J Physiol 595:3219–3236.
45. Weatherstone JH, et al. (2016) Maintenance of neuronal size gradient in MNTB requires sound-evoked activit. J Neurophysiol 117:756–766.
46. Taschenberger H, Woehler A, Neher E (2016) Superpriming of synaptic vesicles as a common basis for intersynapse variability and modulation of synaptic strength. Proc Natl Acad Sci USA 113:E4548–E4557.
47. Lesica NA, Lingner A, Grothe B (2010) Population coding of interaural time differences in gerbils and barn owls. J Neurosci 30:11696–11702.
48. McAlpine D, Jiang D, Palmer AR (2001) A neural code for low-frequency sound localization in mammals. Nat Neurosci 4:396–401.
49. Blosa M, et al. (2015) The extracellular matrix molecule brevican is an integral component of the machinery mediating fast synaptic transmission at the calyx of Held. J Physiol 593:4341–4360.
50. Hilbig H, Nowack S, Boeckler K, Bidmon H-J, Zilles K (2007) Characterization of neuronal subsets surrounded by perineuronal nets in the rhesus auditory brainstem. J Anat 210:507–517.
51. Dietz M, Marquardt T, Salminen NH, McAlpine D (2013) Emphasis of spatial cues in the temporal fine structure during the rising segments of amplitude-modulated sounds. Proc Natl Acad Sci USA 110:15151–15156.
52. Dietz M, et al. (2014) Emphasis of spatial cues in the temporal fine structure during the rising segments of amplitude-modulated sounds II: Single-neuron recordings. J Neurophysiol 111:1973–1985.
53. Moore MJ, Caspary DM (1983)Strychnine blocksbinaural inhibition in lateral superior olivary neurons. J Neurosci 3:237–242.
54. Kuwabara N, Zook JM (1991) Classification of the principal cellsof the medial nucleus of the trapezoid body. J Comp Neurol 314:707–720.
55. Kapfer C, Seidl AH, Schweizer H, Grothe B (2002) Experience-dependent refinement of inhibitory inputs to auditory coincidence-detector neurons. Nat Neurosci 5: 247–253.
56. Zarbin MA, Wamsley JK, Kuhar MJ (1981) Glycine receptor: Light microscopic autoradiographic localization with [3H]strychnine. J Neurosci 1:532–547.
57. Sommer I, Lingenhöhl K, Friauf E (1993)Principal cellsof the rat medial nucleusof the trapezoid body: An intracellular in vivo study of their physiology and morphology. Exp Brain Res 95:223–239.
58. Spangler KM, Warr WB, Henkel CK (1985) The projections of principal cells of the medial nucleus of the trapezoid body in the cat. J Comp Neurol 238:249–262.
59. Smith PH, Joris PX, Yin TC (1998) Anatomy and physiology of principal cells of the medial nucleus of the trapezoid body (MNTB) of the cat. J Neurophysiol 79: 3127–3142.
60. Tollin DJ, Yin TCT (2005) Interaural phase and level difference sensitivity in low-frequency neurons in the lateral superior olive. J Neurosci 25:10648–10657.
61. Bernstein LR (2001) Auditory processing of interaural timing information: new insights. J Neurosci Res 66:1035–1046.
62. Franken TP, Bremen P, Joris PX (2014) Coincidence detection in the medial superior olive: Mechanistic implications of an analysis of input spiking patterns. Front Neural Circuits 8:42.
63. van der Heijden M, et al. (2013) Directional hearing by linear summation of binaural inputs at the medial superior olive. Neuron 78:936–948.
64. Myoga MH, Lehnert S, Leibold C, Felmy F, Grothe B (2014)Glycinergic inhibition tunes coincidence detection in the auditory brainstem. Nat Commun 5:3790.
65. Guinan JJ, Jr, Li RY (1990) Signal processing in brainstem auditory neurons which receive giant endings(calycesof Held) in the medial nucleusof the trapezoid body of the cat. Hear Res 49:321–334.
66. Mc Laughlin M, van der Heijden M, Joris PX (2008) How secure is in vivo synaptic transmission at the calyx of Held? J Neurosci 28:10206–10219.
67. Spirou GA, Brownell WE, Zidanic M (1990) Recordings from cat trapezoid body and HRP labeling of globular bushy cell axons. J Neurophysiol 63:1169–1190.
68. Kuwabara N, DiCaprio RA, Zook JM (1991) Afferents to the medial nucleus of the trapezoid body and their collateral projections. J Comp Neurol 314:684–706.
69. Schuller G, Radtke-Schuller S, Betz M (1986) A stereotaxic method for small animals using experimentally determined reference profiles. J Neurosci Methods 18:339–350.
70. Barnes-Davies M, Forsythe ID (1995) Pre-and postsynaptic glutamate receptors at a giant excitatory synapse in rat auditory brainstem slices. J Physiol 488:387–406.
71. Morest DK (1968) The collateral system of the medial nucleus of the trapezoid body of the cat, its neuronal architecture and relation to the olivo-cochlearbundle. Brain Res 9:288–311.
72. Brownell WE (1975) Organization of the cat trapezoid body and the discharge characteristics of its fibers. Brain Res 94:413–433.
73. Schneider CA, Rasband WS, Eliceiri KW (2012) NIH Image to ImageJ: 25 yearsof image analysis. Nat Methods 9:671–675.

3. DEVELOPMENT OF AXONS FOR PRECISE TEMPORAL AUDITORY PROCESSING: LATE AXON GROWTH DETERMINES MYELINATION PATTERN

3.1. AUTHOR CONTRIBUTIONS

Alisha L. Nabel, Hilde Wohlfrom, Olga Alexandrova, Paula Gundi, Annalenia Malzacher, Sina Bleis, Martin Heß, Michael Pecka and Benedikt Grothe. **Development of Axons for Precise Temporal Auditory Processing: Late Axon Growth Determines Myelination Patterns**. *Manuscript under revision.*

The contributions of the authors Alisha L. Nabel (ALN), Olga Alexandrova (OA), Hilde Wohlfrom (HW), Paula Gundi (PG), Annalenia Malzacher (AM), Sina Bleis (SB), Martin Heß (MH), Michael Pecka (MP) and Benedikt Grothe (BG) to the study included in this thesis are as follows:

ALN, HW, OA, MP and BG designed research; **ALN,** HW, OA, PG, AM, SB, MH performed research; **ALN**, HW, OA revised experiments, **ALN**, OA, PG, AM, SB, MH analyzed data. **ALN**, HW, OA, MP and BG interpreted data. **ALN** prepared figures; MP and BG jointly supervised this work; **ALN** wrote the manuscript with help the of BG.

Development of Axons for Precise Temporal Auditory Processing: Late Axon Growth Determines Myelination Patterns

Alisha L. Nabel[a,c], Hilde Wohlfrom[a], Olga Alexandrova[a], Paula Gundi[a,c], Annalenia Malzacher[a] , Sina Bleis[a], Martin Heß[b], Michael Pecka[a] and Benedikt Grothe[a*]

[a]*Division of Neurobiology, Faculty of Biology, Ludwig-Maximilians-Universität Munich, 82152 Planegg-Martinsried, Germany*

[b]*Division of Systematic Zoology, Faculty of Biology, Ludwig-Maximilians-Universität Munich, 82152 Planegg-Martinsried, Germany*

[c]*Graduate School of Systemic Neurosciences, Ludwig-Maximilians-Universität Munich, 82152 Planegg-Martinsried, Germany*

** Corresponding author*

Abstract

In myelinated axons, the ratio of internode length to axon diameter (L/d) is fundamental for adjusting conduction velocity and timing of action potentials. However, how the L/d-ratio is developmentally determined is unclear. We investigated this crucial question by studying the longitudinal development of specific auditory brainstem axons with superior speed and hyper-accurate timing owing to unusual L/d-ratios. Already days before hearing onset, Nodes-of-Ranvier emerged and, thereby, defined internodal length according to the canonical L/d-ratio of ~100. However, the molecular composition of nodes matured only after hearing-onset successively along the axon from soma to synaptic terminals and, intriguingly, the axon diameter increased overproportionally in some axons, altering their L/d ratio from around 100 to 60. Our findings demonstrate for the first time that myelination patterning results from a complex interplay of oligodendrocytes initially myelinating axons according to their transient axon caliber and a subsequent differential axon thickening.

Introduction

Myelination patterns play a vital role in determining the conduction, shape, propagation velocity and temporal precision of action potentials, all of which are key features of neuronal processing (1–3). Thus, conduction velocity (CV) in myelinated axons crucially depends on axonal diameter, myelin thickness, and the lengths of individual myelin sheaths, also referred to as internodes (4, 5). More specifically, the ratio of internode length to axon diameter (L/d ratio) has been shown to play a key role in setting the CV (6).

Despite its functional significance for almost all neuronal circuits in the brains of higher vertebrates, it is still unclear how specific myelination patterns are established and whether axons or oligodendrocytes (the myelinating cells) define the L/d ratio (7, 8).

Generally speaking, internode length scales positively with axon diameter, and most axons measured have an L/d ratio of around 100 (1,9). There are, however, significant exceptions to this rule, which may shed light on the question of how the L/d ratio is modulated. In the Mongolian gerbil (*Meriones unguiculatus*), a subset of globular bushy cell (GBC) axons, which are essential components of the mammalian sound localization circuit, exhibit such an unusual myelination pattern. More specifically, GBC axons terminating in the lateral third nucleus of the trapezoid body (MNTB) exhibit an unusually low L/d ratio that has been shown to increase conduction velocity and action potential precision relative to other GBCs. Laterally terminating GBCs are known to be tuned to low sound frequencies, and constitute a crucial component of the interaural time difference circuit that is responsible for the most precise temporal computation in the mammalian brain – comparison of the arrival times of sounds at the two ears with a precision on the order of only microseconds (10). GBC axons terminating more medially in the MNTB are tuned to high sound frequencies that are localized by other means. Their axons are, hence, not specialized for interaural time difference processing and appear ordinary in myelin configuration and physiology (6).

We have studied the development of the GBC axons and their myelination schedule. The initial node formation started around day postnatal 7 (P7) continuing until about a week after hearing onset. Nodes developed sequentially along the axon with node near the some

maturating first, nodes close to the axonal terminal maturating latest. Initially L/d ratios were similar in all GBC axons close to the canonical value of around 100. Only after hearing onset, and in parallel with the completion of node development the caliber of GBC axons increased differentially. This was most evident in low-frequency GBC axons, which accounts for their unusually low L/d ratio.

Results

In order to assess how and when the deviation of the L/d ratio in GBC axons tuned to low sound frequencies occurs we evaluated the development of myelination including that of Nodes of Ranvier in GBC axons in Mongolian gerbils (*M. unguiculatus*) in general (Figure 1a). We visualized axons and Nodes of Ranvier by intracellularly filling GBCs with biocytin combined with immunohistochemical labeling of nodal (AnkG), paranodal (CASPR) and juxtaparanodal (Kv1.2) markers. By following single labelled axons and determining their termination in a calyx of Held within the MNTB, we distinguished low-frequency fibers (lateral 1/3 of the MNTB) from high-frequency fibers (medial 1/3 of the MNTB; Fig. 1b). This is possible since the monosynaptic connection of GBC fibers to MNTB neurons via the Calyx of Held synapses follows a strict tonotopic arrangement from lateral (tuned to low frequencies) to medial positions (tuned to high sound frequencies; compare (6, 11)). Figure 1c shows an overview of a biocytin-filled GBC cell and fibers projecting from the AVCN to the contralateral MNTB in a transversal brain section at P8, and a schematic overview of the auditory brainstem (inset). First indications of nodes appeared around P6 (about 6 days before the onset of hearing; see below), first indications for myelination (via the myelin basic protein; MBP) at around P7 (see below). By P8 coverage with myelin sheaths along the entire axon was essentially completed. Therefore, we compared the development of axonal and myelination morphology and of the node of Ranvier in detail from P6/P7 up to >P49 (adult).

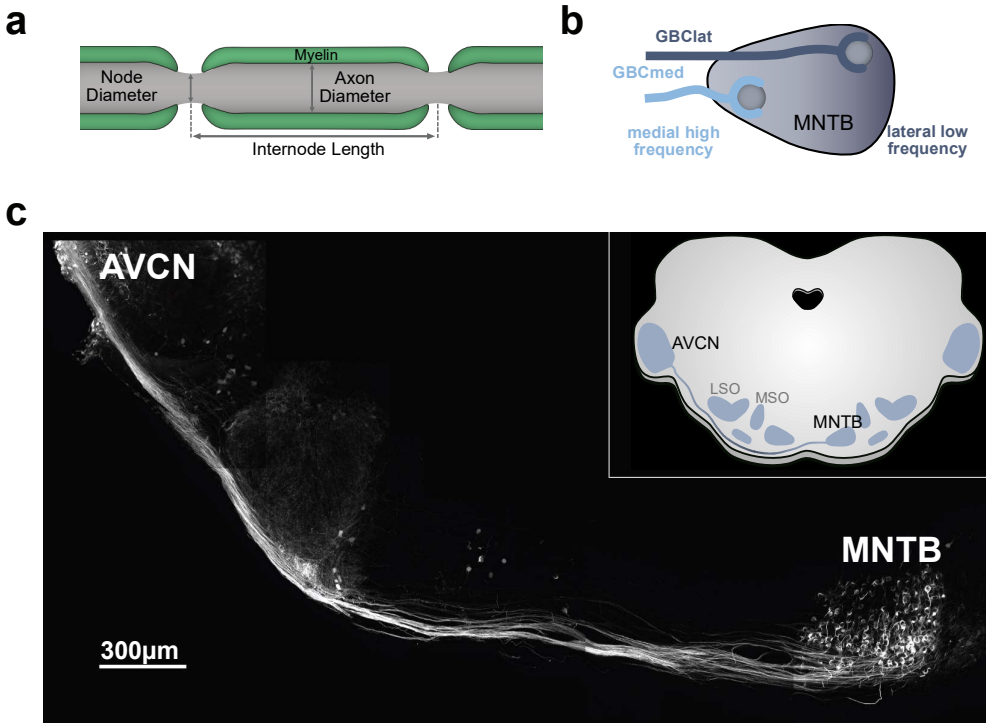

Figure 1: GBC Axons in the AVCN to MNTB Connections. a, Schematic depiction of a myelinated axon with definitions of the parameters analyzed. **b,** The tonotopically organized MNTB. **c,** Confocal image (maximum projection of several optical sections) of a coronal section of the brainstem at P8. Cell bodies of biocytin-labeled GBC axons originate in the AVCN and terminate on principal cells of the MNTB. The inset shows a schematic of the pathway (AVCN: Anterior ventral cochlear nucleus, MSO: Medial superior Olive, LSO: Lateral Superior Olive, MNTB: Medial nucleus of the trapezoid body). Scale bar: 300 µm.

Nodes of Ranvier appear days before onset of hearing but continue to mature for another week

First, we investigated the appearance and development of nodes by determining their molecular composition throughout their postnatal development. Therefore, we immunolabeled the nodal scaffolding protein ankyrin G (AnkG), the paranodal adhesion molecule contactin-associated protein 1 (CASPR) and the juxtaparanodal (delayed rectifier) voltage-gated potassium channel $K_v1.2$ in brainstem sections with biocytin-filled GBC fibers of gerbils at P6/P7 (the earliest stage at which we could identify developing nodes), P8 (onset of myelination), P12 (around hearing onset), P15 (3 days after hearing onset), P26 (an age at which most auditory brainstem structures are adult-like; (12) and around P50 (P49/50/51; mature stage). Although AnkG, CASPR and $K_v1.2$ are characteristic for distinct compartments of the nodes of Ranvier in adults (P26, P50), at the earlier developmental stages (P6/P7 to P15) we observed a considerable degree of colocalization of these proteins (Fig. 2). Clusters of CASPR

(green), in association with more diffuse zones of AnkG (red), first appeared on P6/P7 (Fig. 2b, top). During the second postnatal week (P8 to P15), several distinct patterns of CASPR and AnkG clusters were detected, whereas at P26 and ~P50 fully mature nodes strongly predominate (Fig. 2b, bottom).

Figure 2a depicts the color code used for the identified patterns of immunostaining (node categories) shown in Fig.2b (*left*). Areas solely stained for AnkG, CASPR and $K_v1.2$ are shown in red, green and blue, respectively. Overlapping of AnkG and CASPR is depicted in yellow, colocalization of CASPR and $K_v1.2$ is represented in turquoise. Colocalization of all three markers is shown in white. To classify the identified nodes into different developmental stages, we measured the lengths of the CASPR and AnkG clusters and quantified the degree of overlap. Based on this, we were able to distinguish six categories of nodes. (1) A '*single*' cluster of overlapping AnkG and CASPR. (2) A *'binary'* cluster of two adjacent single clusters. (3) An *'extended'* pattern comprised of a central AnkG expression zone and two bordering paranodal CASPR clusters, in which the broad AnkG clusters continued into the paranodal regions and fully or partly overlapped with CASPR. (4) A *'triple'* expression pattern with a focal AnkG zone and two adjacent clusters overlapping with CASPR. Sometimes the lateral and focal parts exhibited different intensities. (5) A *'semi-mature'* pattern consisting of a narrow AnkG cluster in the center with two adjacent paranodal CASPR clusters, but with a small overlap between AnkG and CASPR. (6) This last category, which corresponds to the well-known *'mature'* configuration, is characterized by a focal AnkG cluster in the nodal region with two flanking CASPR clusters at the paranodes. In this category, AnkG and CASPR clusters never overlapped.
Overall, we identified and classified a total of 66 nodes at P6/P7 (n = 3; n= number of animals), 450 nodes at P8 (n = 4), 278 at P12 (n = 5), 345 at P15 (n = 4), 140 at P26 (n = 2) and 144 at P49-P51 (n = 3).

At P6/P7, the vast majority of nodes (86.4%) showed immature clusters of AnkG and CASPR (Cat.1). At P8, this is still the most frequent class (57.8%), while 13.8% of nodes belonged to Cat. 2, and 25.8% to Cat. 3. Clusters assigned to Cat. 4 accounted for only 0.7% of nodes, and no examples of Cat.5 or Cat. 6 were found in animals of this age. Some 2% of nodes could not be categorized and were classified as "other" (Fig. 2c). At P12 (around the onset of hearing), the incidence of Cat. 1 nodes decreased

sharply to only 2.2%, whereas categories 2 (20.5%), 3 (31.6%) and 4 (19.1%) were most frequent. At this age, a few Cat. 5 (11.2%) and Cat. 6 (14.8%) nodes were also present.

No Cat. 1 nodes were found at P15, and only 13% of the total were of Cat. 2. The most frequent clusters were now of categories 3 (30.7%) and 6 (30.3%), while 11.3% of nodes belonged to Cat. 4 and 14.8% to Cat. 5. In young adults, at P26, the more immature clusters (Cat.1-3) were almost entirely absent. However, Cat. 4 (12.9%) and Cat. 5 (5.7%) nodes were still identifiable at this age, although the majority of nodes (78.6%) were assigned to Cat. 6. At ~P50 (P49-P53), 90.3% of nodes were classified as Cat. 6, and 8.3% as Cat.5. Less mature nodes were barely detectable.

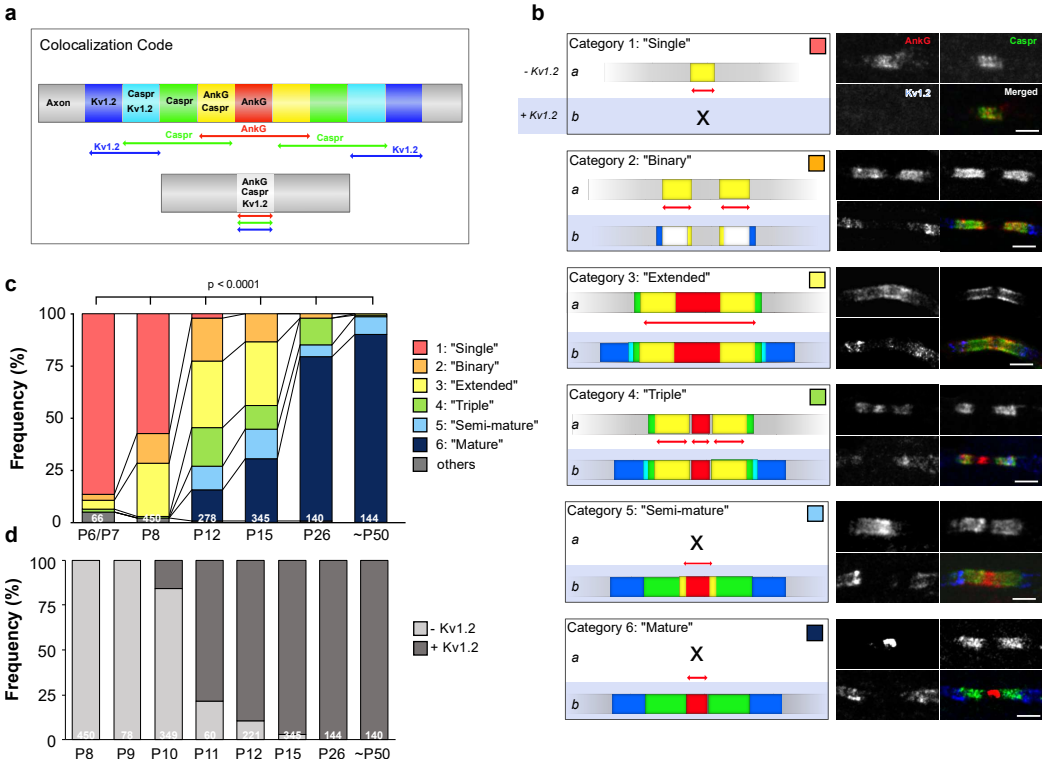

Figure 2: Developmental clustering of nodal, paranodal and juxtaparanodal components along GBC axons. GBC axons were immunostained with antibodies specific for the nodal marker AnkG (red), the paranodal marker CASPR (green) and the juxtaparanodal marker $K_v1.2$ (blue). **a,** Colocalization code for AnkG, CASPR and $K_v1.2$ clusters. Colors correspond to the additive RGB color model. Non-colocalized immunostaining of AnkG, CASPR and and $K_v1.2$ are depicted in red, green, and blue respectively. Overlap of AnkG and CASPR results in yellow, co-expression of CASPR and $K_v1.2$ appears as turquoise. All three colors together result in white. **b,** Schematic depictions (left) of different stages of node formation from 1-6. Representative images of the corresponding category are shown in the right panel. Scale bars: 2.5 µm. The development of nodes of Ranvier proceeds from category 1 to 6, as demonstrated below (see **c** and text). **c,** Quantitative analysis of each category of nodal stage at different ages. Numbers on bars are numbers of analyzed nodes. Numbers of animals: P6/P7: two, P8: four; P12: five; P15: four, P26: two, P49-P51 (~P50): three. P-values are derived from Chi^2 tests. **d,** Expression of $K_v1.2$ at nodes of Ranvier during development. $K_v1.2$ is detectable starting from P10. The percentage of nodes immunolabeled for $K_v1.2$ increases starting from P11. Numbers on the bars represent the number of nodal clusters analyzed.

The voltage-gated potassium channel $K_v1.2$ appeared to localize to nodes independently of the developmental categories we identified (Fig. 2d), with the exception of Cat. 1, in which it was never observed. Thus, $K_v1.2$ is not expressed in nodes of Ranvier at P8, and was expressed in only 15.7% of nodes at P10. Surprisingly, a large proportion of nodes at P11 (78%) and P12 (89%) were $K_v1.2$ immunopositive. At P15, almost all nodes (98%) had $K_v1.2$ expression. Interestingly, in both P12 and P15, we found nodes of categories 2, 3 and 4 with and without $K_v1.2$. However, $K_v1.2$ was not always restricted to the juxtaparanodal region but extended into the paranodal region and often showed asymmetric distributions by P15. At P26 and later, $K_v1.2$ was expressed in all juxtaparanodal regions of the identified nodes.

These data show that morphologically and molecularly mature nodes appear almost exclusively after hearing onset.

Nodes of Ranvier develop sequentially according to their location along GBC axons.

The distribution of node developmental categories did not occur uniformly or randomly along the axon, but rather in a specific developmental sequence, as visible via dividing the axonal tract that runs from the AVCN (GBC somata) towards the calyx of Held in the contralateral MNTB into three distinct areas (Fig. 3; for a higher resolution see supplemental Fig. 1). Area A extends from close to the AVCN/somata to the ipsilateral LSO, B from adjacent to the ipsilateral MSO to the midline (B) and C from close to the contralateral MNTB to the calyx of Held. We reduced the previous six nodal categories (see Fig. 2) to three developmental stages (Fig. 3a): immature (Cat. 1), intermediate (Cat. 2-4) and mature (Cat. 5 and 6). At P8-P15 we found a clear differential distribution of nodal categories, with the more developed nodes lying closer to the somata and the less mature nodes closer to the synaptic terminal (calyx of Held; for details, see Fig. 5c). For instance, at P8 the proportions of immature stage I (48.9%) and intermediate stage II (48.91%) nodes in area A clearly differed from those found in area C, which is most remote from the somata (stage I: 70.8%, stage II: 25.8%; $p=0.0025$, Chi^2 test). At P12, mature stage III accounted for half (44.7%) of the nodes in area A, while in area C all analyzed nodes were classified as intermediate stage II ($p=0.0017$). We observed the same trend after the onset of hearing: At P15, 70.5% of the nodes in area A were classified as stage III (mature), while in areas B (80%; with

respect to A: p<0.000, Chi^2-Test) and C (100%; with respect to A: p<0.0001, Chi^2-Test) nodes were almost exclusively in stage II (intermediate). In young adults (P26) and adults (~P50), the majority of nodes were stage III (mature) with few or no regional differences.

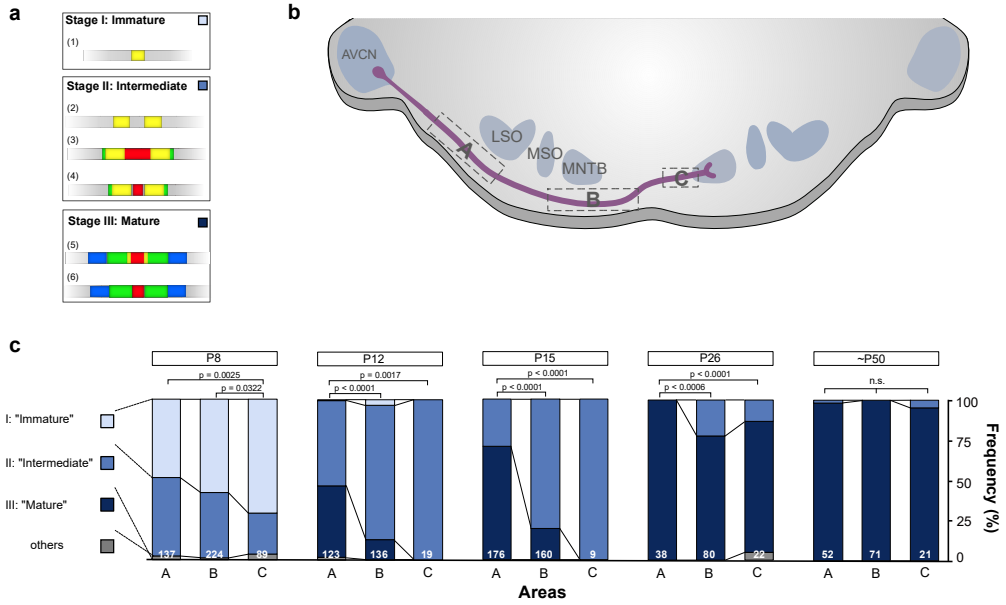

Figure 3: Development of nodal clusters in distinct regions along the AVCN-MNTB tract. a, The categories in Fig. 4 were reduced to three developmental stages. Cat. 1 are classified as immature stage I; Cat. 4 corresponds to immature stage II; and Cat. 5 and Cat. 6 are mature stage III nodes. **b,** Schematic depiction of the auditory brainstem including the AVCN-MNTB with analyzed regions boxed. AVCN – iLSO (ipsilateral LSO, A), iMSO-midline (B), cMNTB (contralateral MNTB, C). **c,** Quantification of nodal stages according to their location at P8, P12, P15, P26 and ~P50. Numbers on the bars represent the number of nodal clusters analyzed. P-values are derived from Chi^2 tests.

Internode length is established before onset of hearing and is similar in laterally and medially ending GBC fibers

We then quantified the internode length of either laterally (GBClat) or medially (GBCmed) terminating fibers at animals on P10/P15 (young animals), time points around the onset of hearing. We analyzed the internode length for P10 and P15 individually, but having observed no significant differences between these ages for GBClat and GBCmed, we did not discriminate between these age groups and pooled the data, and compared them to the data for young adults (P25). The data from the young adult (P25) age group used in this study are re-analyzed and replotted from (6) (identical methods).

We found that the mean internode length at P10/15 decreased consistently towards the calyx of Held terminal in both GBClat and GBCmed fibers (Fig. 4a), as in the case of P25 animals (6). The mean internode length in GBClat fibers decreased progressively by more than half from 181.2 ± 13.42 µm (7th internode from calyx; n = 15, n = number of internodes) to 78.74 ± 13.08 µm (last internode before calyx; n = 18, p<0.0001, Mann-Whitney *U* test; Fig. 4b). Similarly, in GBCmed fibers of young animals the internode length decreased by as much as 75%, from 226.7 ± 25.15 µm (7th internode from calyx; n = 9) to 55.42 ± 16.30 µm (last internode before calyx; n=15, p<0.0001, Mann-Whitney *U* test).

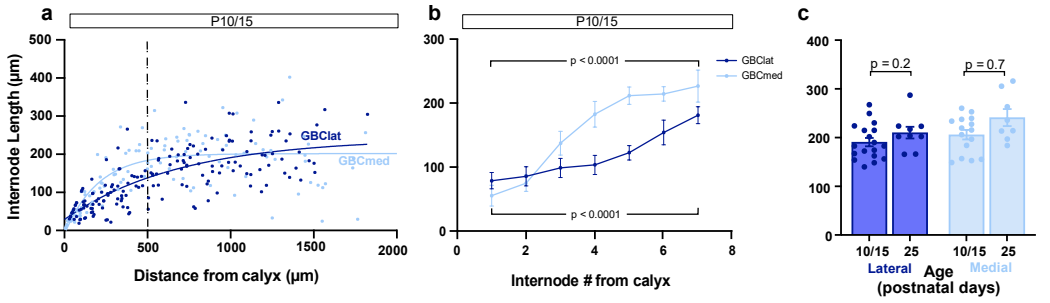

Figure 4: Internode length of GBC fibers remains virtually constant throughout development. **a,** Internode length plotted against the distance from the heminode in young animals (P10/15). Each data point represents a single internode length of all analyzed axons, and the x-value displays the position of the center of the internode. The vertical dashed line indicates the beginning of the steady-state section of internode length. **b**, Internode length plotted as a function of internode number from calyx at P10/15. Data are presented as mean ± SEM. The mean internode length in young animals decreases from the 7th internode from the calyx to the internode closest to the calyx in GBCmed and GBClat fibers (p<0.0001, Mann-Whitney U-test). **c,** Mean internode length in GBClat and GBCmed fibers in young animals (P10/15) and young adults (P25). Only values from the steady-state section >500 µm (for P10/15) and >700 µm (P25) from calyx were used. Data are presented as mean ± SEM and every data point represent the average internode length of a single axon. P-values are derived from student's t-test.

However, internode lengths far from the calyx, in the steady-state area (<500 µm from the calyx; Fig. 4c) of GBClat, did not differ significantly between young animals (190.8 ± 8.54 µm; n = 18/7, number of axons/number of animals) and young adults for GBClat (210.2 ± 12 µm, n = 9/3; p=0.2, Student's *t*-test) nor for GBCmed (P10/15: 205.9 ± 9,86 µm, n = 15/11; P25: 241.2 ± 17.43 µm, n = 8/2; p=0.07, Student's *t*-test). Moreover, internode length far from calyx did not statistically differ between GBClat and GBCmed either at P10/15 (p=0.2519, Student's *t*-test) or at P25 (p=0.1564, Student's *t*-test). This indicates that the internodal length is determined during myelination, which occurs before hearing onset.

Initially nodal and internodal diameters do not differ between laterally and medially ending GBC axons but differentially grow after onset of hearing in laterally ending GBCs

To further asses the development of the relevant structural parameters of GBC axons, we next determined the diameters of the nodes of Ranvier and compared animals on P10/P15, to young adults on P25 (Fig. 5a). As for the internode length, we also merged the data of P10 and P15 for the node diameter. We found that the mean nodal diameter of GBClat in young animals (P10/15: 1.27 ± 0.07 µm, n = 18/7; n = number of axons/number of animals) at around hearing onset had increased significantly by P25 (1.9 ± 0.06 µm; n = 8/2; p<0.0001, Mann-Whitney *U* test). Likewise, the nodal diameter of GBCmed increased from 1.25 ± 0.07 µm (n = 15/11) at P10/P15 to 1.56 ± 0.12 µm (n=8/2) at P25 (p=0.0254; Student's *t*-test). Hence, while nodal diameter did not differ between GBClat and GBCmed at P10/15 (p=0.9501, Mann-Whitney *U* test), a clear difference becomes apparent by P25 (p=0.0159, Student's t-test).

As in the case of P25 animals (see (6)), in P10/P15 animals, node diameter also increases in the direction of the calyx of Held (Fig. 5b). The mean nodal diameter of GBClat fibers increased by 28.57% from 1.19 ± 0.09 µm at the 5th node before heminode) to 1.53 ± 0.12 µm at the last node before heminode (p=0.029, Student's *t*-test; total number of nodes, 15) and by 30.36% in GBCmed – from 1.12 ± 0.12 µm (5th node before heminode) to 1.46 ± 0.15 µm (last node before heminode; p=0.0453, Mann-Whitney *U* test; n=15).

Since not only the nodes of Ranvier and the internode length, but rather the ratio of internodal length to axon caliber, has an essential impact on action potential shape and conductance velocity (see (6)), we examined the axon diameter of GBClat and GBCmed at different developmental stages.

Figure 5c shows representative confocal images of immunohistochemically labeled GBC axons at P10 (*left*) and P25 (*right*). Even on sight, the axon caliber appears much smaller at P10 than at P25 (Fig. 5c, *top*; for quantification, see next section). We also observed a marked increase in the inner axon diameter upon comparing P10 and P25 sections obtained by transmission electron microscopy (TEM; Fig. 5c, *bottom*). We calculated axon diameters in TEM images from measurements of the circumferences

of individual axons (without their myelin sheaths). Despite their methodological differences, the range and minima and maxima of measured axon diameter at P10 obtained by the TEM and IHC approaches were comparable (data not shown). Together with earlier validations of the method (6, 13), these results led us to retain the IHC approach in subsequent experiments.

Using this strategy, we were able to determine axon calibers of GBClat and GBCmed at different developmental stages on P8 (shortly after the onset of myelination), P10 (about 3 days before hearing onset but already with consistent evidence for nodes of Ranvier), P15 (3 days after hearing onset), P17 (at which time structural and functional refinements in the auditory brainstem are known to be highly dynamic (14), P25 (an age at which most auditory brainstem structures are adult-like; (12), and around P50 (P49/P53) as a mature stage. Since our approach required the tracing and reconstruction of GBC axons with a length of approximately 1 mm in a complex 3D structure, the number of reconstructed axons is limited, but yielded sufficient numbers of measured points (with at least two GBCmed axons and two GBClat axons from at least two different animals in each age group).

Figure 5d shows the internodal axon diameter at different ages (postnatal days) for GBClat (dark blue) and GBCmed (light blue). Each data point represents the mean of the internodal axon diameter of an individual axon, assessed by averaging numerous internodal measurements along the reconstructed axon. For each individual internode, 5-10 independent measurements were obtained, and 7-12 internodes were quantified from every axon.

The average internodal axon diameter of GBClat (Fig. 5d, dark blue) at P8 was 1.28 ± 0.09 µm (mean ± SEM; n = 5/2) and had increased only slightly (statistically not significant) by P10 (1.41 ± 0.13 µm, n = 7/2; $p>0.9999$, one-way ANOVA with Bonferroni's *post-hoc* test) and from P10 to P15 (1.52 ± 0.10 µm; n = 11/4; $p>0.9999$). However, at P17, only two days later, the axon caliber of GBClat was significantly larger (2.51 ± 1.20 µm, n=6/2; $p<0.0001$) and increased further until P25 (3.18 ± 0.11 µm; n=9/3; $p=0.0114$). In mature animals, at around P50 (P49/P53), the diameter of GBClat (3.42 ± 0.11 µm; n = 6/2) was comparable to the value on P25 ($p>0.9999$). Hence, axon diameter in GBClat increases markedly after hearing onset.

We observed a similar, albeit statistically insignificant, trend toward increasing axon caliber in GBCmed (Fig. 5d, light blue) from P8, with an average internodal diameter of 1.20 ± 0.07 µm (n = 5/2), to P10 (1.55 ± 0.13 µm, n = 7/5; p=0.436, one-way ANOVA with Bonferroni's *post-hoc* test). However, the diameter of GBCmed increased significantly from P15 (1.26 ± 0.05 µm; n = 8/6; p=0.5627) to P17 (2.08 ± 0.08 µm, n=5/2; p<0.0001). In contrast to GBClat, the diameter of GBCmed did not increase significantly after this developmental stage, reaching and was 2.39 ± 0.13 µm (n = 8/2; p=0.66841) at P25 and 2.41 ± 0.08 µm (n = 6/2; p>0.9999) at ~P50. Comparison of GBClat with GBCmed (Fig. 5e) at the time points described above showed that the diameters of the two fiber types did not differ significantly from each other at P8-P15, but had diverged strongly by P25 (P8: p=0.50, Student's *t*-test; P10: 0.3829, Mann-Whitney *U* test; P15: p=0.541, t-test; P17: p=0.0975, *t*-test; P25: p=0.0004, *t*-test). Moreover, this difference in axon caliber persisted into adulthood at ~P50 (p<0.0001, *t*-test). Therefore, axon caliber of GBClat and GBCmed did not begin to differ until P17, but then a dramatic increase in the diameter of GBClat occured over the following week.

Comparison of the development of axonal and nodal diameter (Fig. 5f) shows that they are similar in young animals at P10/15 (GBClat: axon diameter: 1.48 ± 0.09 µm, node diameter: 1.27 ± 0.07 µm; GBCmed: axon diameter: 1.40 ± 0.09 µm, node diameter: 1.25 ± 0.07 µm). In contrast to the axon caliber (see above), the nodal diameter increases only slightly between P15 and P25 (see above).

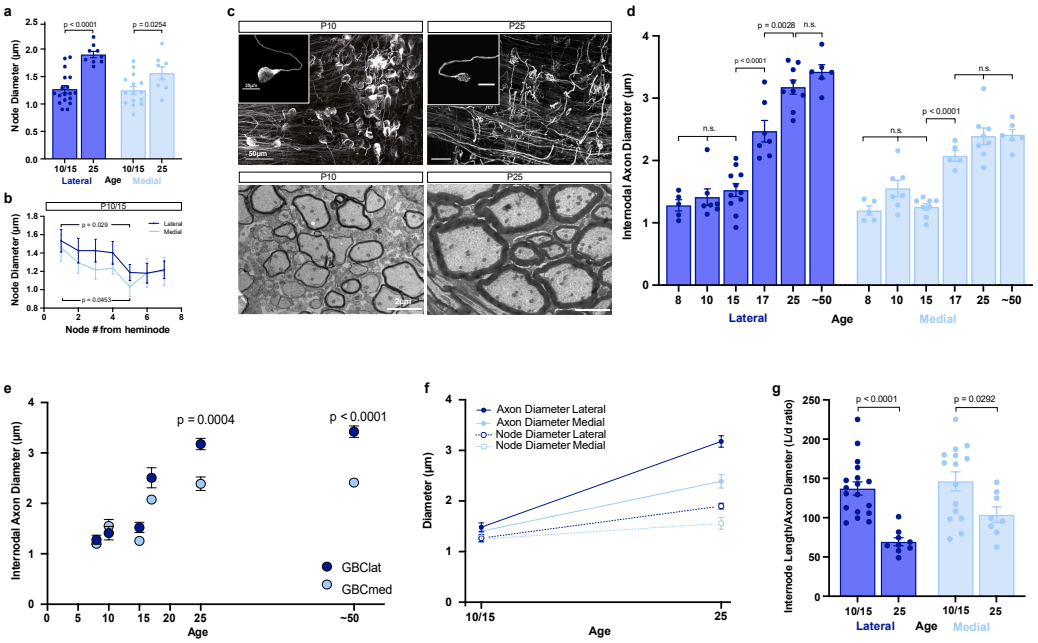

Figure 5: The internodal axon diameter of laterally ending GBCs grows differentially after hearing onset. a, The average diameter of nodes of Ranvier on GBC axons increases from P10/15 (young animals) to P25 (young adults). **b,** Nodal diameter plotted as a function of node number starting from heminode at P10/15. In young animals (P10/15), the mean diameter of nodes of Ranvier on GBClat and GBCmed fibers increases from the 5th node from heminode to the first node from heminode. Data are presented as mean ± SEM and P-values derive from Student's t-test or the Mann-Whitney U test, depending on the distribution of the data. **c,** Representative image (maximum projection of several optical sections) of biocytin-filled GBC axons (*top*) innervating the MNTB at P10 (*left*) and P25 (*right*). Scale bars: 50 µm. Insets show magnifications of single digitally extracted GBClat. Scale bars: 25µm. Transmission electron micrograph (*bottom*) of parasagittal section through the GBC fiber tract at P10 (*left*) and P25 (*right*). Scale bar: 2 µm. **d,** The average internodal axon diameter of GBClat and GBCmed increased from P8 to P50. P-values are derived from one-way ANOVA with Bonferroni's post-hoc test. Each data point in represents the mean of a single axon. **e,** Comparison of the internodal axon diameter between GBClat and GBCmed during postnatal development. P-values are derived from Student's t-test. **f,** Axonal (solid line) and nodal (dashed line) diameters are similar at P10/15. Axon diameter later increases dramatically, whereas node diameter does so only moderately. **g,** The mean internode length to axon diameter (L/d) ratio in GBClat and GBCmed fibers in young animals (P10/15) and young adults (P25). Only values from the steady-state section >500 µm (for P10/15) and >700 µm (P25) from calyx were used. Data are presented as mean ± SEM and every data point represent the L/d ratio of a single axon. P-values are derived from student's t-test.

Delayed and differential axon diameter growth causes an unusual L/d ratio in laterally ending GBC fibers only

The developmental increase in axon diameter observed following hearing onset (in particular in the GBClat fibers) combined with the stable internode length, leads to a differential developmental reduction in the ratio of internode length to axon diameter (L/d) (Fig. 5g) in GBClat only. Far from the calyx, GBClat axons in young animals (P10/15) exhibited a mean L/d ratio of 137.2 ± 8.38 µm (n = 18/7), which fell by almost half to 69.42 ± 5.06 µm in young adults (n = 9/3, p<0.0001, Student's *t*-test) solely as a result of the change in axon caliber. The L/d ratio in GBCmed only showed an insignificant trend in axon caliber from animals (139.7 ± 13 µm, n = 15/11) to young

adults (103.8 ± 9.89 µm, n=8/2; p=0.066 Student's *t*-test). Therefore, the increase in the axon caliber of GBClat relative to GBCmed during the initial period after hearing onset leads to a highly significant difference between the L/d ratios of the two cell types in young adults at P25 (P10/15: p=0.8648; P25: p=0.0059, Student's *t*-test).

Taken together, the results of our morphometrical analysis show that internode length is stable and does not differ between young animals and young adults, and that the increase in axon caliber after hearing onset, particularly in GBClat, leads to the unusually low L/d ratio in low-frequency GBClat fibers.

Discussion

Myelination patterns and axonal morphology can affect and shape the transmission of action potentials along myelinated fibers and thereby tune their conduction timing to meet specific requirements (15–17). Two central factors that determine action potential velocity and fidelity are the lengths of myelin sheaths (18) and the axon diameter (19–21). Moreover, at least for GBC axons, it is the relationship of internode length to axon diameter (L/d ratio) that is the key factor in shaping the arrival times of action potential at target nuclei (6). How myelination patterns are established, and to what extent the axon itself and/or the oligodendrocyte contribute to determining the L/d ratio are therefore a crucial question for understanding neuronal circuit adaptation of temporally precise processing.

We therefore traced the development of internode length and axon diameter in the sound localization circuit of the Mongolian gerbil, in which refined control of timing is crucial for sound localization. Here, we have shown that at GBC axons, irrespective of their frequency tuning, the internode length is set prior to maturation of the axon diameter. Our analyses revealed that, while myelin sheath length before hearing onset already conforms to adult-like patterns, the axon diameter – in particular in low-frequency GBC axons – increases after hearing onset. As a consequence, the L/d ratio decreases to unusually low values in low-frequency GBCs (6), which are required for encoding of the exact arrival times of inputs at the MSO (10). Thus, our findings show that, at least at GBC axons, it is the axon itself that retrospectively modifies the L/d ratio to accommodate its specific demands. Our data support the hypthesis that internodal length and axon caliber can be independently regulated 12. Moreover, we

were able to show that the regulation of axon diameter is the essential mechanism for the refinement of the AVCN-MNTB tract to ensure rapid action-potential conduction. Given that internode length is set early during postnatal development and at a time that precedes acoustic experience, although spontaneous activity is present (22), it appears that oligodendrocyte-intrinsic programs are underlying the early determination of myelin sheath length. The presence of heterogeneous oligodendrocyte populations (7, 23–26) with distinct functions (26, 27) has been reported previously. Moreover, oligodendrocytes are able to form myelin sheaths along inert fibers in the absence of any axonal signals, and the lengths of sheaths are equivalent to in-vivo lengths (7). Thus, oligodendrocyte-intrinsic signals based on distinct populations could indeed account for the establishment of myelination patterns at GBC axons. Since the myelin sheath lengths on GBC axons are established before the oligodendrocyte can sense the final axon diameter, we can rule out the possibility that different oligodendrocytes sense the diameter of an axon, and differentially use this information to direct the formation of sheaths in accordance with the axon diameter in low- and high-frequency fibers (1, 7, 9, 28). The fact that the timing of the increase in axon diameter occurs after hearing onset, and considering that inputs at the MSO are structurally refined at the same time and in response to acoustic experience (14, 29), indicates that sound-evoked activity is involved in modifying the structural parameters. Moreover, GBC axons in mice have been shown to increase in diameter after hearing onset, and this increase depends on sensory activity (13). It remains to be determined whether or not acoustic experience plays a role in differentially adjusting the diameter (and thus the L/d ratio) in low- and high-frequency GBCs. Although it is still not fully understood how myelination patterns are established, our findings provide direct anatomical evidence that supports the theory of a ‘hard-wired’ myelination pattern established by intrinsic properties, which is then modified by the axon (8).

Secondly, the present study provides evidence that maturation of nodes of Ranvier along GBC fibers correlates with the maturation of the axon diameter. We have shown that, shortly after hearing onset, most nodes display immature clusters of nodal markers, and the axon diameter has not yet matured. Node maturation continues until the 3rd and 4th postnatal week, as does that of the axon diameter. In general, we found that nodes of Ranvier exhibit similar clusters of nodal components during development, comparable to those seen in other species and systems (30–35), although the general

time course seem to be postponed and prolonged in the gerbil's sound-localization system. This delayed development, relative to rats and mice, also holds for eye opening, weaning and hearing onset (36). Our data support the idea that, in order to form mature nodes, immature clusters consisting of nodal components first appear adjacent to the early myelin sheaths. These are termed 'heminodes', which approach each other by lateral movement of the myelin sheath and eventually fuse to form mature nodes (30, 37, 38). The immature stage I in our study possibly corresponds to the 'heminode'. Our intermediate stage II would then represent the fusion phase of two 'heminodes', until the mature stage III – the formation of mature nodes – when adjacent 'heminodes' fuse.

Finally, we have, to our knowledge, for the first time provided evidence for a sequential maturation of nodes of Ranvier along the axons, starting from the cell soma and advancing towards the synapse, such that nodes closer to the soma are older than those close to the synaptic terminal. We found that the proportion of mature nodes is higher close to the AVCN (which includes the cell bodies of GBC axons) than it is in the vicinity of the MNTB (where the calyx of Held forms), especially at P12 and P15. This maturation timetable is compatible with the fact that axons grow from soma to synapse (39–41). Axon-intrinsic factors that initiate node formation (42) probably accumulate earlier near the cell body, since nodal scaffolding proteins such as AnkG must be transported in vesicles from the soma of neurons to the developing node (43, 44). However, before the onset of hearing, spontaneous activity propagating along auditory pathways (22, 45) refines auditory brainstem nuclei (46–48), and spontaneous activity can influence myelination as well (49–51).

Overall, the present study provides a more detailed description of when and how specific axonal and myelin characteristics are established during development. It also demonstrates – once again – that specialized circuits in the auditory brainstem in which the timing of action potentials is crucial remain a worthwhile model system in which to study general questions relating to myelination.

Methods

Mongolian gerbils (*Meriones unguiculatus)* were housed in a temperature-controlled room (23°C) with a fixed 12-h light/dark cycle. A total number of 38 animals of either sex and of specified age (P6-P53) were used for this study. All experiments were approved in accordance with the stipulations of the German Animal Welfare Law (*Tierschutzgesetz*).

In Vitro Axon Tracing

Animals were deeply anesthetized with pentobarbital (5 µg/g body weight) and intracardially perfused with ice-cold Ringer's solution containing heparin. Animals were decapitated and the brainstem was quickly removed from the skull under ice-cold ACSF comprising (in millimoles): 125 NaCl, 2.5 KCl, 1 $MgCl_2$, 2 $CaCl_2$, 10 glucose, 1.25 NaH_2PO_4, 26 $NaHCO_3$, 0.5 ascorbic acid, 3 *myo*-inositol, and 2 pyruvic acid (all chemicals from Sigma-Aldrich). For anterograde tracing of GBC axons, two different approaches were used. The first was carried out as described previously (6, 11). For the second tracing approach, a biocytin crystal (Sigma-Aldrich, B4261) was placed on the anteroventral cochlear nucleus (AVCN) on one side of the brain. All subsequent steps were the same for both approaches. Explants were transferred to a chamber with oxygenated ACSF and incubated for 2.5-3 h at room temperature to allow for homogeneous distribution of the tracer in the axons. The brainstems were then immersion-fixed in 4% paraformaldehyde solution for 2 h at room temperature, and stored in the fixative overnight at 4°C.

Immunohistochemistry and Confocal Microscopy

Brainstems were sectioned coronally at 180 µm for axon tracing, and at 80-100 µm for node development experiments, using a vibratome slicer (Leica VT 1200S). Sections were rinsed with PBS and transferred to a blocking solution containing 1% bovine serum albumin, 0.5-2% Triton X-100 (depending on the grade of myelination and slice thickness) and 0.1% saponin in PBS. Multiple immunofluorescence labeling was performed with the following primary antibodies: ankyrinG (AnkG; Synaptic Systems; 386-003; rabbit IgG; 1:500); L+K1.2 (NeuroMab, USA; 75-008 clone K14/16; mouse IgG2b; 1:500); myelin basic protein (MBP; ab7349, abcam; rat IgG; 1:150), contactin-associated protein1 (CASPR; NeuroMab, USA; 75-001 clone 65/35; mouse IgG1;

1:500). Corresponding secondary antibodies (donkey anti-rat Alexa-488, 1:200; goat anti-mouse IgG1 Alexa-488, 1:300; donkey anti-rabbit Alexa-488, 1:200; donkey anti-rabbit Alexa-647, 1:300; donkey anti-mouse (H+L) A-647, 1:200; goat anti-mouse IgG2b Alexa-594, 1:200; donkey anti-rabbit Alexa-594, 1:200; all from Dianova), Streptavidin-Cy3 (Dianova, 1:300) and Fluorescent Neurotrace blue (Life Technologies, N21479; 1:200) were applied. Sections were mounted in Vectashield antifade medium (Vector Laboratories) under coverslips and sealed with nail polish. All antibodies used are validated by their suppliers. Confocal optical sections were acquired with a Leica TCS SP5-2 confocal laser-scanning microscope (Leica Microsystems) equipped with HCX PL APO X63/numerical aperture 1.3 glycerol 37°C objective. Fluorochromes were visualized with excitation wavelengths of 405 nm (emission filter, 410–430 nm) for Nissl Blue, 488 nm (emission filter, 510–540 nm) for Alexa-488, 561 nm (emission filter, 565–585 nm) for tetramethylrhodamine dextran and Streptavidin-Cy3, 594 (emission filter 605–625 nm) for Alexa-594 or Texas Red, and 633 nm (emission filter 640–760 nm) for Alexa-647. For axon tracing experiments, overlapping stacks of images were acquired from coronal brainstem slices at the level of the trapezoid body in the area spanning the MNTB and the contralateral tracer injection site (ACVN); voxel size: 482×482×500 nm. For node development experiments, stacks were acquired at distinct regions along the area from the AVCN to the MNTB; voxel size: 96.29×96.29×293.73nm. Red-green-blue (RGB) stacks, montages of RGB optical sections, and maximum-intensity projections were assembled using the ImageJ 1.37k plug-ins and Adobe Photoshop 8.0.1 (Adobe Systems) software. For axon tracing experiments, GBC fibers were identified by calyces of Held that terminated in the contralateral MNTB and then back tracked across sections toward the cochlear nucleus. On the basis of their exact site of termination in the MNTB, GBC axons were classified as being either medially or laterally terminating. MNTB borders were determined using a counterstain (Fluorescent Neurotrace blue).

Morphometry

Using the Paintbrush tool, individual axons of GBCs filled with tetramethylrhodamine dextran or biocytin were manually labeled by following a single axon successively through each optical section of the confocal image stack. Subsequently, the neighboring axons were digitally deleted. The same axon was identified in the neighboring overlapping confocal image stacks and digitally extracted. Nodes of

Ranvier were identified on the basis of immunohistochemical labeling (IHC) of nodal and paranodal or juxtaparanodal marker proteins (AnkG and CASPR or $K_v1.2$). Distances between nodes of Ranvier (measured mid-node to mid-node) were measured in three dimensions in confocal image stacks using the ImageJ 1.37k Sync Measure three-dimensional tool. Internodal axon diameter and nodal diameter measurements were assessed in two dimensions from maximum-intensity projections of confocal image stacks. Axon diameter was assessed by multiple measurements of internodal axon segments of intracellularly labelled axons in between immunostained nodes of Ranvier, and the average diameter per axon across several measurements was used for analysis.

Electron microscopy

Two gerbils aged P10 were deeply anesthetized with pentobarbital (5 µg/g body weight) and intracardially perfused with Ringer's solution followed by perfusion with 2.5% glutaraldehyde plus 2% PFA in 0.075 M cacodylate buffer (CB). Brainstems were removed from the skull and post-fixed in the same fixative overnight at 4°C. Brainstems were washed in CB and sectioned parasagittally at 500 µm using a vibratome slicer and a 1 mm × 1 mm block containing the trapezoid body fibers was extracted using a razor blade. Tissue was washed in CB and post-fixed in 1% OsO_4 in 0.1 M CB for 1–2 h. After washing and dehydrating in a graded series of acetone, tissue was embedded in resin and ultrathin sections were cut. The sections were mounted on formvar coated copper grids, contrasted with lead citrate and uranyl acetate, and photographed with a FEI Morgagni transmission electron microscope at 80 kV.

Statistics

Data were analyzed using GraphPad Prism8 (GraphPad Software, La Jolla, CA), IgorPro 5.02 (Wavemetrics) and MS Excel 2021 (Microsoft, Redmond, WA). Data are represented as mean±SEM. Tests for normal distribution were performed using the Kolmogorov–Smirnov test. *P* values were derived from two-sided Student's *t*-tests, or one-way ANOVA with Tukey's *post-hoc* test, provided the dataset passed the normality test. Otherwise, significance was tested using either the Mann-Whitney *U* test or the Kruskal-Wallis test with Dunn's *post-hoc* test (*P* values are significant if they are less than 0.05). *P* values in Fig. 4b and Fig. 5c derive from Chi^2 tests. Data presented in Fig. 3a and C were fit with exponential functions. No blinding was done for data

analysis of axon diameter, node diameter and internode length, simply because one cannot measure the length of single labelled axons without starting at the region of termination in the MNTB. However, measuring persons were ignorant of the details of the ITD circuit and, hence, the conceptional issues of the study. Quantitatively identical measurements were used for analysis of all data.

Data availability

The data that support the findings of this study will be available at:

…..

References

1. J. B. Hursh, Velocity and diameter. *American Journal of Physiology* **127**, 131–139 (1939).
2. A. H. Seidl, Regulation of conduction time along axons. *Neuroscience* **276**, 126–134 (2014).
3. L.-A. Ranvier, Contributions à l'histologie et à la physiologie des nerfs périphériques. *C R Acad Sci* **73**, 1168–1171 (1871).
4. A. F. Huxley, R. Stampfli, Evidence for Saltatory Conduction in. *J. Physiol.* **108**, 315–339 (1949).
5. R. S. Smith, Z. J. Koles, Myelinated nerve fibers: computed effect of myelin thickness on conduction velocity. *American Journal of Physiology* **219**, 1256–1258 (1970).
6. M. C. Ford, *et al.*, Tuning of Ranvier node and internode properties in myelinated axons to adjust action potential timing. *Nature Communications* **6**, 1–14 (2015).
7. M. E. Bechler, L. Byrne, C. Ffrench-Constant, CNS Myelin Sheath Lengths Are an Intrinsic Property of Oligodendrocytes. *Current Biology* **25**, 2411–2416 (2015).
8. M. E. Bechler, M. Swire, C. Ffrench-Constant, Intrinsic and adaptive myelination—A sequential mechanism for smart wiring in the brain. *Developmental Neurobiology* **78**, 68–79 (2017).
9. W. A. H. Rushton, A Theory of the Effects of Fibre Size in Medullated Nerve. *J. Physiol.* **115**, 101–122 (1951).
10. B. Grothe, M. Pecka, D. McAlpine, Mechanisms of Sound Localization in Mammals. *Physiological Reviews* **90**, 983–1012 (2010).
11. A. Stange-Marten, *et al.*, Input timing for spatial processing is precisely tuned via constant synaptic delays and myelination patterns in the auditory brainstem.

Proceedings of the National Academy of Sciences of the United States of America **114** (2017).

12. K. Kandler, A. Clause, J. Noh, Tonotopic reorganization of developing auditory brainstem circuits. *Nature Neuroscience* **12**, 711–717 (2009).
13. J. L. Sinclair, *et al.*, Sound-evoked activity influences myelination of brainstem axons in the trapezoid body. *Journal of Neuroscience* **37**, 8239–8255 (2017).
14. A. K. Magnusson, C. Kapfer, B. Grothe, U. Koch, Maturation of glycinergic inhibition in the gerbil medial superior olive after hearing onset. *Journal of Physiology* **568**, 497–512 (2005).
15. A. H. Seidl, E. W. Rubel, D. M. Harris, Mechanisms for adjusting interaural time differences to achieve binaural coincidence detection. *Journal of Neuroscience* **30**, 70–80 (2010).
16. A. H. Seidl, E. W. Rubel, Systematic and differential myelination of axon collaterals in the mammalian auditory brainstem. *Glia* **64**, 487–494 (2016).
17. R. G. Almeida, D. A. Lyons, On Myelinated Axon Plasticity and Neuronal Circuit Formation and Function. *The Journal of Neuroscience* **37**, 10023–10034 (2017).
18. D. Suminaite, D. A. Lyons, M. R. Livesey, Myelinated axon physiology and regulation of neural circuit function. *Glia* **67**, 2050–2062 (2019).
19. J. A. Murray, W. F. Blakemore, The Relationship between Internodal Length and Fibre Diameter in the Spinal Cord of the Rat. *Journal of Neurological Sciences* **45**, 29–41 (1980).
20. M. Ibrahim, A. M. Butt, M. Berry, Relationship between myelin sheath diameter and internodal length in axons of the anterior medullary velum of the adult rat. *Journal of the Neurological Sciences* **133**, 119–127 (1995).
21. B. Y. a L. Hodgkin, Ii, Along Vi. 221–224 (1954).
22. M. Sonntag, B. Englitz, C. Kopp-Scheinpflug, R. Rübsamen, Early postnatal development of spontaneous and acoustically evoked discharge activity of principal cells of the medial nucleus of the trapezoid body: An in vivo study in mice. *Journal of Neuroscience* **29**, 9510–9520 (2009).
23. N. Kessaris, *et al.*, Competing waves of oligodendrocytes in the forebrain and postnatal elimination of an embryonic lineage. *Nature Neuroscience* **9**, 173–179 (2006).
24. V. Tripathi, *et al.*, The nuclear-retained noncoding RNA MALAT1 regulates alternative splicing by modulating SR splicing factor phosphorylation. *Molecular Cell* **39**, 925–938 (2010).
25. D. H. Rowitch, A. R. Kriegstein, Developmental genetics of vertebrate glial-cell specification. *Nature* **468**, 214–222 (2010).
26. J. C. Murtie, W. B. Macklin, G. Corfas, Morphometric Analysis of Oligodendrocytes in the Adult Mouse Frontal Cortex. *Journal of Neuroscience Research* **85**, 2080–2086 (2007).
27. R. Marisca, *et al.*, Functionally distinct subgroups of oligodendrocyte precursor cells integrate neural activity and execute myelin formation. *bioRxiv* **23**, 363–374 (2020).

28. S. Lee, *et al.*, A culture system to study oligodendrocyte myelination- processes using engineered nanofibers Seonok. *Nature Methods* **9**, 917–922 (2012).
29. C. Kapfer, A. H. Seidl, H. Schweizer, B. Grothe, Experience-dependent refinement of inhibitory inputs to auditory coincidence-detector neurons. *Nature Neuroscience* **5**, 247–253 (2002).
30. V. Brivio, C. Faivre-Sarrailh, E. Peles, D. L. Sherman, P. J. Brophy, Assembly of CNS Nodes of Ranvier in Myelinated Nerves Is Promoted by the Axon Cytoskeleton. *Current Biology* **27**, 1068–1073 (2017).
31. D. P. Schafer, A. W. Custer, P. Shrager, M. N. Rasband, Early events in node of Ranvier formation during myelination and remyelination in the PNS. *Neuron Glia Biology* **2**, 69–79 (2006).
32. I. Vabnick, S. D. Novaković, S. R. Levinson, M. Schachner, P. Shrager, The clustering of axonal sodium channels during development of the peripheral nervous system. *Journal of Neuroscience* **16**, 4914–4922 (1996).
33. M. N. Rasband, *et al.*, Dependence of nodal sodium channel clustering on paranodal axoglial contact in the developing CNS. *Journal of Neuroscience* **19**, 7516–7528 (1999).
34. K. Susuki, *et al.*, Three mechanisms assemble central nervous system nodes of ranvier. *Neuron* **78**, 469–482 (2013).
35. J. Xu, E. Berret, J. H. Kim, Activity-dependent formation and location of voltage-gated sodium channel clusters at a CNS nerve terminal during postnatal development. *Journal of Neurophysiology* **117**, 582–593 (2017).
36. F. Wilkinson, EYE AND BRAIN GROWTH IN THE MONGOLIAN GERBIL (Meriones unguiculatus). *Behavioural Brain Research* **19**, 59–69 (1986).
37. K. Feinberg, *et al.*, A glial signal consisting of Gliomedin and NrCAM clusters axonal Na+ channels during the formation of nodes of Ranvier. *Neuron* **65**, 490–502 (2010).
38. L. Pedraza, J. K. Huang, D. R. Colman, Organizing principles of the axoglial apparatus. *Neuron* **30**, 335–344 (2001).
39. J. L. Goldberg, How does an axon grow? *Genes and Development* **17**, 941–958 (2003).
40. B. K. Mueller, Growth cone guidance: First steps towards a deeper understanding. *Annual Review of Neuroscience* **22**, 351–388 (1999).
41. F. De Castro, Chemotropic molecules: Guides for axonal pathfinding and cell migration during CNS development. *News in Physiological Sciences* **18**, 130–136 (2003).
42. M. N. Rasband, E. Peles, The nodes of Ranvier: Molecular assembly and maintenance. *Cold Spring Harbor Perspectives in Biology* **8**, 1–15 (2016).
43. M. R. Kaplan, *et al.*, Induction of sodium channel clustering by oligodendrocytes. *Nature* **386**, 724–728 (1997).
44. C. Zhang, K. Susuki, D. R. Zollinger, J. L. Dupree, M. N. Rasband, Membrane domain organization of myelinated axons requires βII spectrin. *Journal of Cell Biology* **203**, 437–443 (2013).

45. N. X. Tritsch, *et al.*, Calcium action potentials in hair cells pattern auditory neuron activity before hearing onset Nicolas. *Nat Neurosci.* **13**, 1050–1052 (2010).
46. G. Kim, K. Kandler, Elimination and strengthening of glycinergic/GABAergic connections during tonotopic map formation. *Nature Neuroscience* **6**, 282–290 (2003).
47. G. Kim, K. Kandler, Synaptic changes underlying the strengthening of GABA/ glycinergic connections in the developing lateral superior olive Gunsoo. *Neuroscience* **171**, 924–933 (2010).
48. A. Clause, *et al.*, The Precise Temporal Pattern of Prehearing Spontaneous Activity Is Necessary for Tonotopic Map Refinement. *Neuron* **82**, 822–835 (2014).
49. S. Mensch, *et al.*, Synaptic vesicle release regulates the number of myelin sheaths made by individual oligodendrocytes in vivo Sigrid. *Nat Neurosci.* **18**, 628–630 (2015).
50. S. Mitew, *et al.*, Pharmacogenetic stimulation of neuronal activity increases myelination in an axon-specific manner. *Nature Communications* **9**, 1–16 (2018).
51. S. Koudelka, *et al.*, Individual Neuronal Subtypes Exhibit Diversity in CNS Myelination Mediated by Synaptic Vesicle Release. *Current Biology* **26**, 1447–1455 (2016).

Acknowledgements

This study was supported by the Deutsche Forschungsgemeinschaft DFG (SFB 870, project B02 to MP and BG). We thank T. Czopka and P. Hardy for valuable comments on earlier versions of the manuscript.

Author Contributions

ALN, MP and BG conceived the study and ALN, HW and OA designed the experiments. ALN, HW, OA, PG, AM, SB, MH performed research; ALN, OA, PG, AM, SB, MH analyzed data. ALN prepared figures and wrote the manuscript with supervision from B.G.; MP and BG jointly supervised this work; All authors provided comments and approved the manuscript.

Competing interests

The authors declare no competing interests.

Supplementary Information

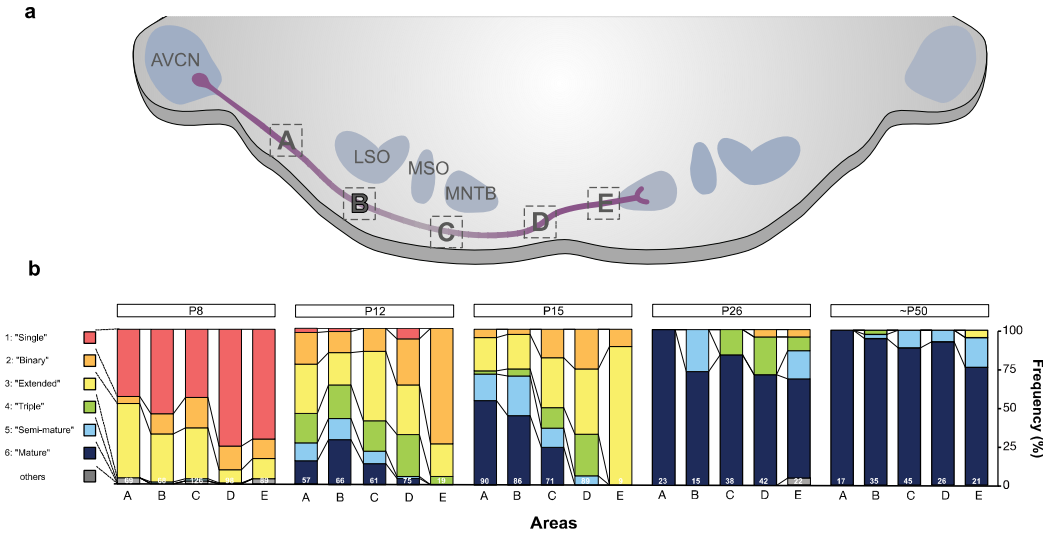

Supplemental Figure 1: Development of nodal clusters at distinct regions along the AVCN-MNTB pathway. a, Schematic of the auditory brainstem including the AVCN-MNTB with analyzed regions. AVCN - iLSO(A), iLSO - iMSO(B), iMSO - iMNTB(C), midline(D), and cMNTB (E). **b,** Quantification of different nodal stages according to their location. Numbers in the bars represent number of analyzed clusters.

4. DISCUSSION

It has long been known that the ability of myelin to ensheath and insulate axons allows for efficient action potential propagation through saltatory conductance (Hursh, 1939; Huxley & Stampfli, 1949; Tasaki, 1939). Most recently it has become evident that faster is not always better and that it is the exact timing of action potentials rather than the maximum speed that needs to be optimized to realize specific functions in the CNS (Ford et al., 2015; Pajevic et al., 2014; Seidl, 2014). Specific patterns of myelin can affect and shape the transmission of action potentials and thereby tune their conduction timing (Almeida & Lyons, 2017; Ford et al., 2015; Armin H. Seidl et al., 2010; Armin H. Seidl & Rubel, 2016). Powerful factors that largely control conduction velocity are the thickness and length of myelin sheaths (Suminaite et al., 2019) as well as the axon diameter (Hodgkin, 1954; Ibrahim et al., 1995; Murray & Blakemore, 1980).
An ideal model system to study structure-function relations of myelinated axons is the mammalian ITD circuit. In order to process microsecond differences in the time of arrival of sound at the two ears, neurons of the MSO need highly precise inputs (Grothe et al., 2010; Myoga et al., 2014; Seidl, 2014), and thus well-tuned conduction time is required.

4.1. LOW L/*D* RATIOS AS FUNCTIONAL ADAPTATION

Axons in the CNS can display variable myelination patterns of which not all functions have been completely identified yet (Hill et al., 2018; Micheva et al., 2016; Stedehouder et al., 2018; Tomassy et al., 2014). Such unique myelination patterns and axon morphology are evident along GBC axons involved in the binaural auditory brainstem circuit.
GBC axons tuned to low frequencies (< 2kHz) transmit highly precise signals concerning the fine-structure as well as the envelope of sounds from the ipsilateral ear to the binaural comparator neurons in the MSO. Their remarkably thick axons with comparably short internodes lead to unexpected low ratios of myelin sheath length to axon diameter (L/*d* ratios) which in turn result in significant faster conduction velocity and enhanced action potential precision (Ford et al., 2015). These structural deviations might provide the anatomical basis that could explain the temporal precedence of the main inhibitory pathway to the MSO (Brand et al., 2002; Roberts et al., 2013). However, besides projecting to the MSO, neurons of the MNTB also target different auditory nuclei including the LSO, a nucleus best known for computing ILDs of primarily high frequency sounds (Tollin, 2003). Thus, it is unclear whether the unique axonal and myelination morphology of low-frequency GBC axons are specific

adaptations for ITD processing or whether they are simply correlated with the tonotopic organization *per se* and thus represent a general variation.

To assess whether these structural variations are of functional relevance for ITD coding, we compared the findings in the gerbil (Ford et al., 2015) to mice – a species with poor low-frequency hearing (< 3kHz) and that can hardly use ITDs as a binaural cue (Grothe & Pecka, 2014). Our data show that unlike gerbils, mice do not exhibit the differential axon diameter or internode length along their GBC fibers and furthermore exhibit a 'normal' L/*d* ratio comparable to the canonical value of around 100 (Hursh, 1939; Rushton, 1951). This indicates that low-frequency GBCs in the gerbil indeed demand faster and well-timed conduction along their axons. Considering that computational modeling predicted even smaller L/*d* ratios than the observed for maximum speed – a situation with high energy costs – GBC axons may not be simply tuned to reach the highest conduction velocity but rather to attain a specific arrival time whilst minimizing energy consumption (Ford et al., 2015). Such specific adaptations in the inhibitory auditory brainstem circuit to meet temporal demands have been reported previously. The developmental refinement of inhibitory MSO synapses (Kapfer et al., 2002) and the sharpening of inhibitory kinetics (Magnusson et al., 2005) take place in various ITD users such as cat (Clark, 1969), chinchilla (Perkins, 1973), baboon (Kim et al., 2014) and was even found human (R.J. Kulesza, personal communication), but not in animals not utilizing ITDS (rat, opossum, bat (Kapfer et al., 2002) and mouse (Fischl et al., 2016)).

Here, we have shown that the length of internodes in a region with stable internode length (<700µm from calyx) displays a species-specific adjustment. However, GBC axons in the gerbil exhibit a further structural feature, that is a dramatic decrease of internode length towards the calyx of Held (Ford et al., 2015). Unlike in axons in the PNS (Quick et al., 1979), this shortening of internode length along GBC axons in gerbils alone is not sufficient for large and rapid depolarization of the giant synaptic terminal. To ensure propagation of action potentials into the calyx, additional spatial variation of nodal and internodal diameters as well as the large size of the calyx process are crucial (Ford et al., 2015). We found that the characteristic shortening of internode length near the calyx is also present in mice, and thus this structural feature may be a common characteristic of GBC fibers to depolarize the giant synapse. We have not directly tested whether variation of the structural parameters influence the depolarization of the calyx in mice, but our observation that nodal and axonal diameter vary in mice as well suggests that these variations might be crucial in GBC axons as such.

The concept of optimizing conduction and arrival time of action potentials by regulating myelination patterns is not new. Myelination of olivocerebellar fibers in rats results in uniform conduction time essential for normal expression of complex spike synchrony (Lang & Rosenbluth, 2003). Similarly, in mouse thalamocortical afferents myelin can be held accountable for conquering with the variability of different travel. Here, myelination realizes a constant latency from thalamus to cortical cells across the

cortex regardless of different traveling distances (Salami et al., 2003). Furthermore, observations in the avian and mammalian auditory system show that different axonal diameter between axon branches of the same neuron are associated with the tuning of conduction time to allow simultaneous arrival of action potentials (Seidl et al., 2010; Seidl & Rubel, 2016).
However, with their deviation of the L/*d* ratio to unusual low values, low-frequency GBC axons reveal a novel and more complex strategy for enhancing conduction of action potentials.

4.2. DEVELOPMENT OF MYELINATION PATTERNS AND AXONAL MORPHOLOGY

The discovery that the adjustment of the L/*d* ratio in fact ensures the exact timing of inputs has raised several unanswered questions. First, when and how are these unique myelination patterns and L/*d* ratios of low frequency GBC axons established? And furthermore, who determines the configuration of internode length to axon diameter – the oligodendrocyte, the axons, or both?

By elucidating the development of axonal and myelin properties of GBC axons we found that the length of myelin sheath (far from the calyx) is established well before the axon diameter significantly increases, irrespective of the frequency tuning (see Figure 7). Moreover, we found the characteristic shortening of internodes towards the calyx of Held also already in juveniles (P10/P15). Contrary to the already mature-like myelination patterns, the axon diameter is only half the size in juveniles compared to adult animals at P25 as reported in Ford et al., (2015) and reanalyzed in here. Our findings that internode length is set prior to the increase of the axon caliber and that the differential axon diameter of high, and low-frequency GBC axons is delayed, is in line with observations of the excitatory inputs in the gerbil ITD circuit. Here, the establishment of internode length along spherical bushy cell (SBC) axon branches transmitting excitatory inputs to the MSO precedes the axon diameter increase, and the differential axon diameter of contralateral and ipsilateral axon branches lags (Armin H. Seidl & Rubel, 2016). This indicates that the axon diameter in general increases relatively late during development and that the myelination of axons is determined comparably early, at least in the gerbil ITD circuit. A late axon diameter growth is also apparent in the sound localization circuit in mice with axons of trapezoid body fibers reaching mature-like thickness only between P25-P35 (Sinclair et al., 2017).

However, the crucial determinants in adjusting the conductance timing of low frequency GBC axons are not solely the length of myelin sheaths or the axon diameter

as such, but rather their ratio (Ford et al., 2015). We found that the L/*d* ratio was more than twice as large in juveniles (P10/15) compared to the expected small values at P25, suggesting the involvement of mechanisms that alter the L/*d* ratio. Given that GBC axon diameter, regardless of its frequency tuning, increase only during the second and third postnatal week, we hypothesize that this diameter increase is primarily responsible for the retrospective adjustment of the L/*d* ratio.

4.2.1. The role of sound activity

In the auditory systems, like in other sensory systems, activity plays a major role in shaping and refining neuronal connections. Taking into consideration that the increase of axon diameter and hence the decrease of L/*d* ratio happens several days after the onset of hearing indicates that sound-evoked activity might shape the system to meet the required conduction timing. The impact of activity onto the increase of axon diameter has been shown previously in unmyelinated axons (Chéreau et al., 2017). Moreover, in mice sound-evoked activity leads to an increase of axon diameter and myelin thickness in trapezoid body axons (Sinclair et al., 2017).
In general, hearing onset and thus acoustic experience has been shown to play an instructive role in refining especially structural parameters of other SOC nuclei as well (Ford et al., 2009; Kapfer et al., 2002; Magnusson et al., 2005; Seidl, 2014). In the MNTB-LSO connection, structural refinements largely happen after hearing onset, such as axonal pruning and structural elimination of synaptic boutons (Sanes et al., 1990; Sanes & Siverls, 1991) as well as structural reorganization of connections and pruning of dendritic arbors (Sanes et al., 1990). Similarly, structural refinements in the MNTB-MSO connection are observed after hearing onset marked by a decrease of axonal spread and branch points of MNTB axons to enhance the precision of the circuit (Werthat et al., 2008). Moreover, inhibitory synapses initially innervate both the soma and dendrites of MSO neurons before hearing onset and are restricted solely to the soma in response to acoustic experience (Kapfer et al., 2002). This is consistent with the observed experience-dependent development of fast kinetics of evoked inhibitory postsynaptic currents (IPSCs) and potentials (IPSPs) in the MSO, presumably to improve the encoding of ITDs (Magnusson et al., 2005). Thus, hearing-experience represents a potential contributing factor that could also influence the L/*d* ratio decrease. However, the role of activity-independent processes and the influence of spontaneous action potentials before the onset of hearing have also to be taken into consideration. Already before birth, axons from the CN start to innervate targets within the SOC (Kandler & Friauf, 1993) and processes independent of activity also regulate the size and mono-innervation of the calyx of Held (Xiao et al., 2013). Shortly after birth spontaneous action potentials are elicited in the cochlea propagating throughout the auditory pathway (Sonntag et al., 2009) and thereby, for instance, refining

tonotopic maps of the LSO as well as functionally pruning and strengthening inputs at the LSO (Kim & Kandler, 2003, 2010).

We have not tested the impact of spontaneous or sound-evoked activity onto the development of structural parameters directly. Sound-depriving gerbils by using ear plugs might clarify whether and to what extent acoustic experience affects the substantial decrease of the L/d ratio. Further, to assess whether axons themselves adjust their L/*d* ratios elsewhere than in sound localization circuits, similar analyses in different neuronal circuits would be needed.

Interestingly, P17 in particular seems to represent a critical timepoint during development in the inhibitory sound localization circuit of gerbils. Synaptic glycinergic currents of MSO neurons become mature at P17 (Magnusson et al., 2005) and analogously, neurons in the LSO reach their fast kinetics in the gerbil also around P17 (Sanes, 1993). Consistent with these observations, we found that GBC axons had a significantly thicker diameter for the first time at P17 compared to earlier time points. Notably, the diameter of the high-frequency GBC axons has already reached its final diameter at this point, whereas low-frequency fibers continue to increase until they reach a plateau at P25. The reason for this could simply be explained by the smaller diameter of the high-frequency axons by itself, which is naturally reached earlier. However, given that calyces in the high-frequency area of the MNTB mature earlier compared with the low-frequency calyces (Ford et al., 2009) and the dendritic arbors in the high-frequency region of the LSO are refined before those in the low-frequency area (Sanes et al., 1992), frequency-dependent axon maturation might be possible.

4.2.2. Evidence for oligodendrocyte-intrinsic programs

In addition to the influence of sound-evoked activity we addressed the question of whether the axon or oligodendrocytes determine the myelination pattern and thus the ratio of internode length to axon diameter. However, it is important to note that those two possibilities are not mutually exclusive. Indeed, both can operate at the same time, with both cortical and spinal cord oligodendrocytes responding to fiber diameter as well as forming shorter and longer sheaths respectively (Bechler et al., 2015).

However, considering that in our system the specific length and patterning of myelin sheaths is established before the expected axon diameter is reached, oligodendrocytes myelinating GBCs must, at least in part, have an intrinsic program that is independent of morphological parameters of the axon. The existence of such oligodendrocyte-intrinsic instructions has been shown previously (Bechler et al., 2015, 2017) and two main possibilities have been proposed explaining the influence of oligodendrocyte-intrinsic mechanisms onto myelin sheath variation in the CNS. The first possibility is

that oligodendrocytes sense the axonal diameter and respond according to physical cues. In light of the succeeding increase of GBC axon diameter, we can exclude the possibility that oligodendrocytes respond to the diameter. A second theory proposes the existence of different oligodendrocyte populations with heterogenous intrinsic programs (Bechler et al., 2017). The presence of such heterogeneity of oligodendrocytes has been reported previously by genetic lineage tracing and molecular profiling (Bechler et al., 2015; Kessaris et al., 2006; Murtie et al., 2007; Rowitch & Kriegstein, 2010; Tripathi et al., 2010). Most recently, Marisca et al., (2020) provided evidence that different subgroups of oligodendrocytes have distinct functions. For example, a small population of oligodendrocytes in the mouse prefrontal cortex forms considerably short internodes (Murtie et al., 2007). In support of this, oligodendrocytes are able to form myelin sheaths along artificial fibers in the absence of any axonal signals, and the lengths of sheaths are equivalent to in vivo lengths (Bechler et al., 2015). Together, these studies suggest that oligodendrocyte-intrinsic signals based on distinct populations can indeed determine the myelination of axons. Different oligodendrocyte populations with distinct function, i.e., different sheath lengths, could be accountable for the early establishment of myelination patterns found in GBCs. But it remains unclear whether such oligodendrocyte-specific instructions are indeed at play in our system.

4.2.3. Evidence for axon-intrinsic programs

Axon-intrinsic programs could also be accountable for determining myelination patterns. In the PNS, axonal signals can regulate both, whether an axon is myelinated by Schwann cells *per se* and the thickness of the myelin sheath (Michailov et al., 2004; Taveggia et al., 2005). In contrast, in the CNS no signals from the axon being solely responsible to initiate myelination have been identified yet. Nonetheless, axonal signals can contribute to the initiation of myelination (Benninger et al., 2006; Câmara et al., 2009), lead to myelin thickness increase (Brinkmann et al., 2008), and can enhance myelination (de Biase et al., 2011). The absence of an axonal master initiation signal together with the ability of oligodendrocytes to generate compact, multilaminar myelin membranes around inert artificial fibers (Bechler et al., 2015; S. Lee et al., 2012b), suggests that axon signals are not required for initial myelin formation in the CNS, however they display important roles in the subsequent modification of myelination. Axon-intrinsic signals can predetermine the length of individual myelin sheaths by expressing specific ‘stop’- signals for the myelin sheath elongation. Such signals were found in the zebrafish spinal cord where the cell adhesion molecule (CAM) Neurofascin186 is formed early during development and accumulate in premature cluster at unmyelinated axon. These early clusters seem to predetermine later positions of nodes of Ranvier (Auer, 2019; T. Czopka, personal communication). Thus, axon intrinsic signals might additionally control, or contribute to controlling

myelin sheath length during early postnatal development and the involvement of both, axonal and oligodendrocyte-intrinsic signals to determine myelin-sheath length might be likely.

However, taken together and the importance of the L/d ratio into consideration which is adjusted by the increase in axon diameter and not by modifying the internodal length, our findings indicate that at least in GBC axons, the axon itself is the crucial determinant in adjusting its specific configuration. Since the increase of axon diameter and thus the decrease of L/d ratio happen after the onset of hearing and together with previous observations in the sound localization circuit, we speculate that hearing-experience might influence these adjustments.
Our observations fit well with the theory proposed by Bechler et al. (2017) of a 'hard-wired' oligodendrocyte-intrinsic program (*here: specific internode length*) followed by extrinsic cues to modify and adjust (*here: increase of axon diameter to decrease L/d ratio*) the system for its specific temporal requirements, possibly in an activity-dependent manner (*here: hearing experience*).

4.3. DEVELOPMENT OF NODES OF RANVIER ALONG GBC AXONS

Another prominent structural component of myelinated axons that is crucial for proper action potential velocity is the node of Ranvier. To gain a deeper understanding of how neural systems develop in general, we once again took advantage of the fact that GBC axons represent a well-suited model system to study myelination. To understand how different morphological parameters develop and whether their maturation is linked, we elaborated to what extent the development of nodes accompanies that of GBC axon morphology. To this end, we performed detailed analysis of well-defined nodal, paranodal and juxtaparanodal markers and discovered several distinct clusters that depended strongly on maturation state.

4.3.1. Temporal sequence of node development

In total, we have identified and chronologically classified six clusters, ranging from premature (Cat. 1) to a mature cluster (Cat. 6). Most of these categorized clusters show striking similarity to clusters described in the PNS (Brivio et al., 2017; Schafer et al., 2006; Vabnick et al., 1996) and in different circuits in the CNS (Rasband et al., 1999; Susuki et al., 2013), and it is thus interesting to observe this in our system as well. Moreover, we found that the overall time course of GBC node development seems to be concurrent with the development of nodes in the optic nerves of rats (Rasband et

al., 1999; Susuki et al., 2013). This indicates that the developmental sequence of nodes of Ranvier is a rather universal process, regardless of system and species in the CNS. Further, we found that the maturation GBC nodes persists throughout the whole postnatal development, starting with the first premature clusters before the onset of hearing when myelination of the GBC-MNTB connection is initiated (P6/P7) and from P12 on, around hearing onset, gradually proceeds up until the 3rd and 4th postnatal week.

Surprisingly, even at P15, three days after hearing onset, most nodes still display premature clusters. This corresponds well to our finding that axon diameter matures only after P15, indicative of a highly dynamic state at this age. The fact that we found most nodes mature only at P26 together with the observation that nodes in the rat optic nerve becoming mature already between P13 and P17 (Rasband et al., 1999; Susuki et al., 2013), suggests a postponed and extended maturation progresses at GBC axons in gerbils. In support to this suggestion and contrary to most earlier studies, we have identified two supplementary clusters which have not or barely been described before (Cat. 3 and Cat. 5). These additional transient clusters could be required as intermediate steps in a prolonged maturation duration. Alternatively, their identification could be simply explained by the usage of different quantification and qualification approaches that we used in comparison to previous studies. However, a general delayed development of gerbils compared to other rodents, such as mice and rats, has been reported, evident by the fact that eye-opening, weaning and hearing onset happens a few days later (Wilkinson, 1986). Moreover, in the auditory system, the connection of the CN-to-LSO and MNTB-to-LSO are formed and functional earlier in rats (Kandler & Friauf, 1995) than in gerbils (Sanes, 1993). Consistent with this, GBC axon diameter in mice starts to increase already at P10 (Sinclair et al., 2017), while in gerbils we have shown that the increase is not detectable before P17. Noteworthy, clusters of K_v1.2 at first occur sparsely at developing nodes at P10 and within only two days all nodal clusters showed K_v1.2 expression (see Figure 7). As we could not detect a temporal relationship between the occurrence of K_v1.2 and the six distinct nodal clusters, Kv1.2 seem to be regulated independently of AnkG and CASPR and might rather be expressed based on the age as such.

Similar to the axon diameter of GBCs nodes exhibit mature morphology during the 4th postnatal week, thus well after the onset of hearing (see Figure 7). As discussed earlier, hearing-activity might be involved in structurally refining GBC axons. Given that node assembly seems to be associated with myelination onset (Brivio et al., 2017; Rasband et al., 1999; Susuki et al., 2013) and given that myelination can be modified in response to experience (Bechler et al., 2017; Gibson et al., 2014; Liu et al., 2012, 2016; McKenzie et al., 2014; Scholz et al., 2010; Xiao et al., 2017), that may indicate that node formation is influenced by activity. Various studies have analyzed whether and to what extent neuronal activity influences node and node-like structures. Upon sound-

induced hearing loss, nodes of Ranvier become elongated and the length and thickness of paranodes as well as juxtaparanodes change (Tagoe et al., 2014). Neuronal activity leads to an altering of mitochondria distribution in nodes of Ranvier (Ohno et al., 2011). Further, upon neuronal activity, the length and location of axon initial segments (AIS) is modified and the increase in AIS length is accompanied by an increase of Na_v channels (Susuki & Kuba, 2016) which are associated with AnkG. Moreover, Na_v channels at GBCs fail to cluster at heminodes in deaf mice (Xu et al., 2017). Together, these studies indicate that nodes, node-like structures, and nodal components are in general susceptible to neuronal activity.
However, while there is good evidence for the susceptivity of nodes to sensory activity, various observations have highlighted that intrinsic cytoskeletal and scaffolding proteins interact with each other to form proper nodes. In addition, the axoglial interaction seem to induce the clustering of Na_v channels, independent of neuronal activity (Rasband & Peles, 2016). Against the hypothesis of an activity-driven node formation in our systems would argue that myelination patterns are established prior to hearing experience. Hence, at least the position of nodes is already determined before sound-evoked activity. However, spontaneous activity must not be disregarded which is already present before hearing onset (Sonntag et al., 2009) and which might affect the node formation.

In summary, we have described Ranvier nodes along GBC show similar maturation compared to other neuronal circuits and species. The developmental time course of our findings supports the current understanding of node development. That is that first, premature clusters consisting of nodal components appear adjacent to the early myelin sheaths. These clusters are termed ‘heminodes’ which move towards each other by lateral movement of the myelin sheath and eventually fuse to mature nodes (Brivio et al., 2017; Feinberg et al., 2010; Pedraza et al., 2001). Since the clusters we discovered on GBC axons mirror clusters found in previous studies, our findings further support this mechanism which is illustrated in Figure 6 based AnkG and CASPR. We did not elucidate when and to what extent other components are assembled, for instance NF186 or Na_v channels. For a deeper insight into how nodes develop and form at GBC axons, other components in respect to AnkG remain determined. Furthermore, the association of clusters with myelin also needs to be elucidated. We have not validated whether single clusters are already linked to myelin. However, the appearance of myelination already at P6 is indicative of an association of the premature clusters with myelin sheath.

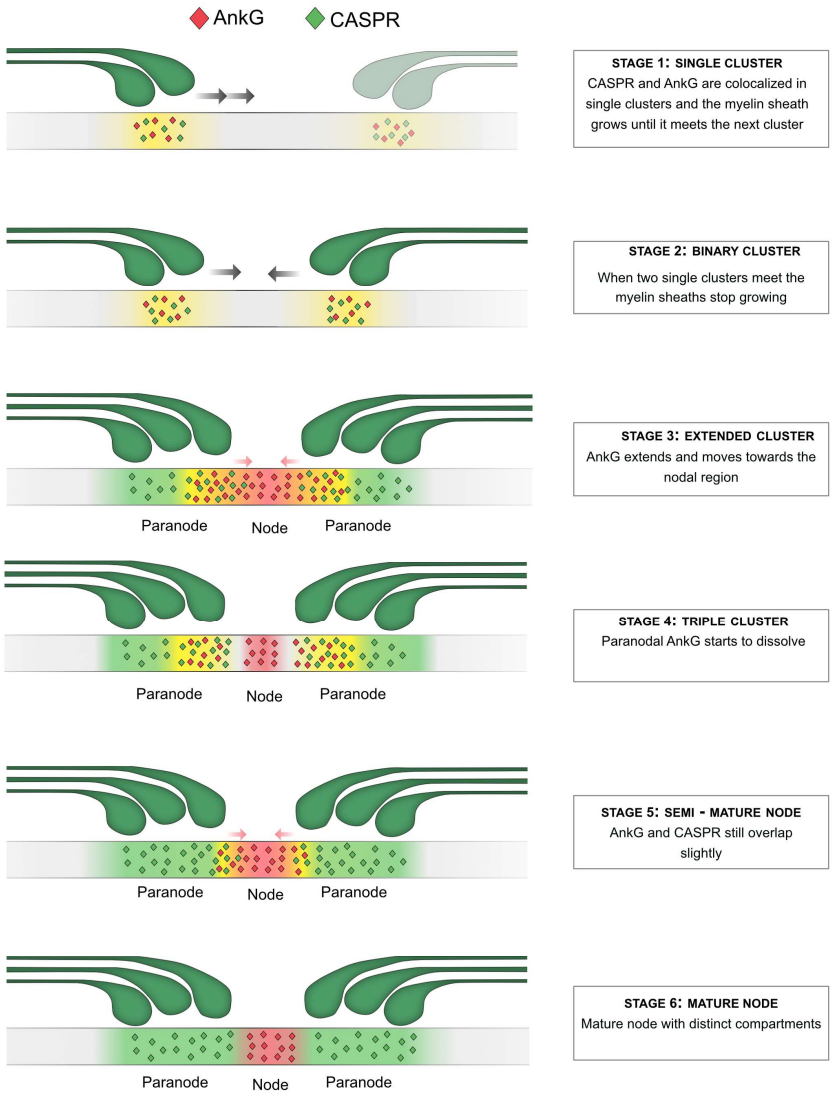

Figure 6: Schematic node development along globular bushy cell axons. First, AnkG and CASPR are co-expressed in single clusters (stage 1). Subsequently, binary clusters of AnkG and CASPR (stage 1) occur, presumably moving towards each other to form extended clusters (stage 3) with AnkG and CASPR expression in their supposed compartments (node and paranode respectively), yet with AnkG extending into the paranodal region. Next, AnkG becomes clustered more distinctively in the nodal region and the paranodal AnkG starts to dissolve (stage 4). Subsequently nodes of Ranvier become mature (stage 5 and stage 6).

4.3.2. Spatial sequence of node development

Axons connect different neurons over long distances and thus can reach lengths of up to one meter (as for axons of the human sciatic nerve) (Muzio & Cascella, 2021). GBC axons extend over a distance of several millimeters from AVCN to MNTB and we therefore asked whether or not nodes of Ranvier develop uniformly along the length of the axons. Interestingly, we found that a higher proportion of mature nodes are present close to the soma compared to close to the calyx, especially at P12 and P15. These findings indicate an earlier maturation of nodes that are located closer to the cell body of GBCs. This observation is, to our knowledge, the first in proposing a sequential development of nodes according to their position along axons. Given that axons grow from soma to synapse (De Castro, 2003; Goldberg, 2003; Mueller, 1999) nodes of Ranvier might just follow the same trend of directional maturation and axon intrinsic factors initiating node formation (Rasband & Peles, 2016) could accumulate earlier at the cell body. In support of this hypothesis, nodal scaffolding proteins such as AnkG must be trafficked to the developing node in vesicles from the soma of neurons. Clustering of AnkG at the developing node in CNS and PNS was blocked upon inhibition of the vesicular transport (Kaplan et al., 1997; Zhang et al., 2013). Furthermore, when axons were separated from their cell bodies PNS nodes lack clusters of AnkG and ßIV-spectrin (Zhang et al., 2013), indicating that AnkG is dependent on the vesicular transport from the neuronal cell body. This mechanism (Kaplan et al., 1997; Zhang et al., 2013) could explain our observation of earlier maturation close to the soma. However, the involvement of spontaneous action potentials and sound-evoked activity might also be accountable of the earlier maturation of nodes close to the soma.
Determining the role of acoustic experience onto the overall node development *per se* and onto the sequential maturation would be an important next step. For instance, ear-plugging gerbils before hearing onset and analyzing nodal clustering after the onset of hearing could provide insight into the role of sound-evoked activity on node maturation. Further validations would be compulsory to determine whether this sequential maturation also occurs in other systems and species, thus providing a general mechanism of consecutive maturation or whether it is specific for the sound localization system in gerbils. The simplest way would be by analyzing nodes of Ranvier in the same system, yet in a different rodent such as mice. Given that for mice, unlike for gerbils, genetic tools are available, the most reasonable approach elucidating the influence of acoustic experience onto node maturation might represent the use of sound-deprived mice for further analysis.

By studying the development of Ranvier nodes along GBC axons we have observed that they mature in a similar temporal sequence concurrent to the maturation of the axon diameter: whereas at P15, shortly after hearing onset, both nodes and axons are still immature, the maturation of both progresses until the 4th postnatal week exhibiting mature morphologies. In addition, we showed that node maturation at GBC axons

mirror the development in other systems and species, yet the period during which nodes mature appear to be prolonged and shifted at GBC fibers. We show, based on our information, for the first time a sequential maturation of nodes, with nodes located more proximally along the axon showing more mature appearance compared to nodes at distally positions along the axon.
To understand the influence of nodal maturation on action potential properties, electrophysiological recordings are needed at time points when a high proportion of nodes still have an immature appearance (P8-P15).

4.3.3. Correlation of the developmental timing between Ranvier nodes and axon morphology

Structural refinements along GBC axons happen over several weeks during postnatal development. The temporal correlation between the maturation of nodes of Ranvier and the development of axonal and myelin morphology is summarized in Figure 7. While the internode length is already set early during development (Fig. 7, *pink* and *violet*, high- and low-frequency GBCs respectively) and before hearing onset (shaded area between P12 and P13), the axon diameter (Fig. 7, *light blue* and *dark blue*, high- and low-frequency GBCs respectively) and nodal clustering (*red*) reach maturity after hearing onset during the 3rd and 4th postnatal weeks. The expression of $K_v1.2$ at nodal clusrers (*green*) was sparsely detected at P10 and by P12, $K_v1.2$ was expressed at all nodes.
To relate our findings with previous observed refinements in the auditory brainstem, the time points of structural refinements of the calyx of Held (*gray* arrow), LSO (*orange* arrow) and MSO (*yellow* arrow) are displayed on top In the LSO, structural refinements largely happen after the onset of hearing as evidenced by tonotopic sharpening through axonal and dendritic pruning (Kandler & Gillespie, 2005). These structural changes occur during the 3rd postnatal week, thus shortly after hearing onset (Sanes et al., 1992; Sanes & Siverls, 1991). In the MSO, a decrease of dendritic complexity that begins from before hearing onset (Chirila et al., 2007) progresses until the end of the 3rd postnatal week (Sanes et al., 1992). In parallel with the dendritic pruning, inhibitory synapses refine spatially to the soma (Kapfer et al., 2002), accompanied by a sharpening of inhibitory kinetics (Magnusson et al., 2005). In the calyx of Held most refinements happen early during development with the initial contact formed before birth and mono-innervation occurring between P2-P5 (Hoffpauir et al., 2006; Holcomb et al., 2013). The morphology of the calyx itself changes during the first postnatal weeks with a transition of a cup-shaped to a highly fenestrated morphology (Hoffpauir et al., 2006; Kandler & Friauf, 1993). This structural change begins around hearing onset an progresses up until postnatal week four (Ford et al., 2009). By and large, GBC axon diameter and node maturation appear to parallel the structural refinements that occur in the LSO and MSO, as well as in the calyx Held.

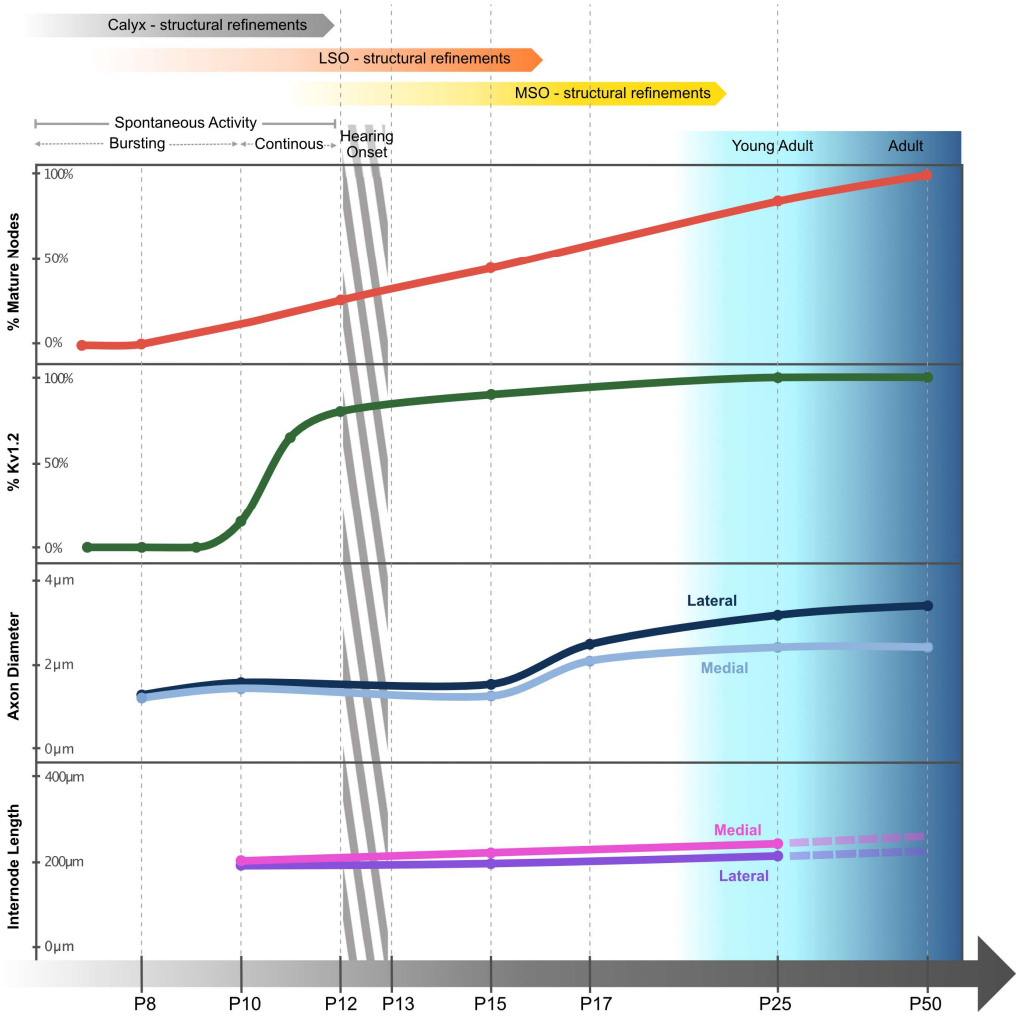

Figure 7: Postnatal development of GBC axon parameters: From bottom to top: internode lengt (high-frequency axons: *pink*; low-frequency axons: *violet*), axon diameter (high-frequenc axons: *light blue*; low-frequency axons: *dark blue*), occurrence of $K_v1.2$ at nodal cluste (*green*) and the frequency of mature nodes (Cat. 5 and Cat. 6; *red*) are displayed durin postnatal ages from P8 to P50 (arrow on the bottom). The dashed lines of internode lengt represent the presumed further development. The colored arrows on top indicate structura refinements of the calyx of Held (*gray*), LSO (*orange*) and MSO (*yellow*). Hearing onse (shaded area) in gerbils happen between P12-P13 and before spontaneous activity is presen first in a bursting and later in a continuous firing pattern. The transition of young adult to adu is demonstrated by the light to dark blue gradient.

4.4. CONCLUSION

Fine-tuning of structural parameters such as myelination patterns, axon morphology and node of Ranvier formation along axons is a key determinant for proper neural circuit function. GBC axons in the auditory brainstem involved in sound localization circuits represent a well-suited model system to analyze the development of specific structural features. In the auditory brainstem, low-frequency GBC axons are involved in ITD processing and exhibit unique myelination patterns, exceptionally thick axons and thus low L/*d* ratios. Our findings show that the unusual low L/*d* ratios are specific for the ITD circuit in Mongolian gerbils and thus represent functional adaptations to meet the temporal demands in this circuit. Given that internode length is established early during postnatal development (P10) and axon diameter only increases during late postnatal development (P17), the axon diameter increase is the key factor leading to the required low L/*d* ratio in the ITD circuit. Therefore, it is the axon itself determining its specific low L/*d* ratio. Whether this retrospective modification by the axon might represent a common mechanism to meet specific needs for conduction velocity and timing also in other systems and mammals will be an interesting question to address. Furthermore, an unresolved question is whether and to what extent sensory-evoked activity is involved in adjusting the structural adaptations of GBC axons. Our findings highlight the role of the axon in determining the relation of myelin sheath length to axon diameter. Moreover, we provided new insights into the general developmental time course of structural features along myelinated axons involved in central brain circuits. These findings may contribute to understanding and identifying the underlying mechanisms of myelination in the CNS. Understanding how neuronal systems determine their appropriate myelination and identifying signals involved in proper myelin formation may be important in order to cope with myelin deficit disease. To study general questions of myelination the specialized time-demanding circuits in the auditory brainstem remain a worthwhile model system.

REFERENCES

Aggarwal, S., Yurlova, L., & Simons, M. (2011). Central nervous system myelin: Structure, synthesis and assembly. *Trends in Cell Biology*, *21*(10), 585–593.

Almeida, R. G., & Lyons, D. A. (2017). On Myelinated Axon Plasticity and Neuronal Circuit Formation and Function. *The Journal of Neuroscience*, *37*(42), 10023–10034.

Auer, F. (2019). *Investigating mechanisms of myelin sheath length regulation and plasticity*. Doctoral dissertation, Ludwig-Maximilians-Universität München.

Auer, F., Vagionitis, S., & Czopka, T. (2018). Evidence for Myelin Sheath Remodeling in the CNS Revealed by In Vivo Imaging. *Current Biology*, *28*(4), 549-559.

Bakhti, M., Snaidero, N., Schneider, D., Aggarwal, S., Möbius, W., Janshoff, A., Eckhardt, M., Nave, K. A., & Simons, M. (2013). Loss of electrostatic cell-surface repulsion mediates myelin membrane adhesion and compaction in the central nervous system. *Proceedings of the National Academy of Sciences of the United States of America*, *110*(8), 3143–3148.

Baraban, M., Koudelka, S., & Lyons, D. A. (2017). Ca 2+ activity signatures of myelin sheath formation and growth in vivo. *Nature Neuroscience*, *21*(January).

Bechler, M. E., Byrne, L., & Ffrench-Constant, C. (2015a). CNS Myelin Sheath Lengths Are an Intrinsic Property of Oligodendrocytes. *Current Biology*, *25*(18), 2411–2416.

Bechler, M. E., Byrne, L., & Ffrench-Constant, C. (2015b). CNS Myelin Sheath Lengths Are an Intrinsic Property of Oligodendrocytes. *Current Biology*, *25*(18), 2411–2416.

Bechler, M. E., Swire, M., & Ffrench-Constant, C. (2017). Intrinsic and adaptive myelination—A sequential mechanism for smart wiring in the brain. *Developmental Neurobiology*, *78*(2), 68–79.

Bekesy, G. V. (1970). Traveling Waves as Frequency Analysers in the Cochlea. *Nature*, *225*, 1207–1209.

Boiko, T., Rasband, M. N., Levinson, S. R., Caldwell, J. H., Mandel, G., Trimmer, J. S., & Matthews, G. (2001). Compact myelin dictates the differential targeting of two sodium channel isoforms in the same axon. *Neuron*, *30*(1), 91–104.

Borst, J. G. G., & Sakmann, B. (1996). Calcium influx and transmitter release in fast CNS synapse. *Nature*, *383*, 431–434.

Brand, A., Behrend, O., Marquardt, T., McAlpine, D., & Grothe, B. (2002). Precise inhibition is essential for microsecond interaural time difference coding. *Nature*, *417*(6888), 543–547.

Brivio, V., Faivre-Sarrailh, C., Peles, E., Sherman, D. L., & Brophy, P. J. (2017). Assembly of CNS Nodes of Ranvier in Myelinated Nerves Is Promoted by the Axon Cytoskeleton. *Current Biology*, *27*(7), 1068–1073.

Bullock, T., & Horrdige, G. A. *Structure and Function in the Nervous System of Invertebrates*. Freeman.

Bunge, M. B., Bunge, R. P., & Ris, H. (1961). Ultrastructural study of remyelination in an experimental lesion in adult cat spinal cord. *The Journal of Biophysical and Biochemical Cytology*, *10*, 67–94.

Butt, A. M., & Berry, M. (2000). Oligodendrocytes and the control of myelination in vivo: New insights from the rat anterior medullary velum. *Journal of*

Neuroscience Research, *59*(4), 477–488.
Chambers, D., Huang, C., & Matthews, G. (2015). Nerve action potential and propagation. In *Basic Physiology for Anaesthetists* (pp. 221–227). Cambridge University Press.
Chang, K. J., Redmond, S. A., & Chan, J. R. (2016). Remodeling myelination: Implications for mechanisms of neural plasticity. *Nature Neuroscience*, *19*(2), 190–197.
Chéreau, R., Saraceno, G. E., Angibaud, J., Cattaert, D., & Nägerl, U. V. (2017). Superresolution imaging reveals activity-dependent plasticity of axon morphology linked to changes in action potential conduction velocity. *Proceedings of the National Academy of Sciences of the United States of America*, *114*(6), 1401–1406.
Chirila, F. V., Rowland, K. C., Thompson, J. M., & Spirou, G. A. (2007). Development of gerbil medial superior olive: Integration of temporally delayed excitation and inhibition at physiological temperature. *Journal of Physiology*, *584*(1), 167–190.
Chiu, S. Y., & Ritchie, J. M. (1980). Potassium Channels in the Nodal and Internodal Axonal Membrane of Mammalian Myelinated Fibers. *Nature*, *284*, 170–171.
Chomiak, T., & Hu, B. (2009). What is the optimal value of the g-ratio for myelinated fibers in the rat CNS? A theoretical approach. *PLoS ONE*, *4*(11).
Clark, G. M. (1969). The ultrastructure of nerve endings in the medial superior olive of the cat. *Brain Research*, *14*(2), 293–305.
Czopka, T., ffrench-Constant, C., & Lyons, D. A. (2013). Individual oligodendrocytes have only a few hours in which to generate new myelin sheaths invivo. *Developmental Cell*, *25*(6), 599–609.
De Castro, F. (2003). Chemotropic molecules: Guides for axonal pathfinding and cell migration during CNS development. *News in Physiological Sciences*, *18*(3), 130–136.
Del Río Hortega, P. (1921). La glía de escasa radiaciones (Oligodendroglia). *Boletín de La Real Sociedad Española de Historia Natural*, *21*, 63–92.
Del Río Hortega, P. (1922). Son homologables la glía de escasas radiaciones y la célula de Schwann? *Boletín de La Sociedad Española de Biología*, *10*, 25–28.
Del Río Hortega, P. (1928). Tercera aportación al conocimiento morfológico e interpretación funciónal de la oligodendroglía. *MemReal Soc Espan Hist Nat*, *14*, 5–122.
Dondzillo, A., Sätzler, K., Horstmann, H., Altrock, W. D., Gundelfinger, E. D., & Kuner, T. (2010). Targeted three-dimensional immunohistochemistry reveals localization of presynaptic proteins Bassoon and Piccolo in the rat calyx of held before and after the onset of hearing. *Journal of Comparative Neurology*, *518*(7), 1008–1029.
Eaton, A., & Robert, C. (1984). Neural Mechanisms of Startle Behavior. In *Plenum Press, New York*.
Feinberg, K., Eshed-Eisenbach, Y., Frechter, S., Amor, V., Salomon, D., Sabanay, H., Dupree, J. L., Grumet, M., Brophy, P. J., & Peles, E. (2010). A glial signal consisting of Gliomedin and NrCAM clusters axonal Na+ channels during the formation of nodes of Ranvier. *Neuron*, *65*(4), 490–502.
Fettiplace, R. (2017). Hair cell transduction, tuning and synaptic transmission in the mammalian cochlea. *Comprehensive Physiology*, *7*(4), 1197–1227.

Fischl, M. J., Burger, R. M., Schmidt-Pauly, M., Alexandrova, O., Sinclair, J. L., Grothe, B., Forsythe, I. D., & Kopp-Scheinpflug, C. (2016). Physiology and anatomy of neurons in the medial superior olive of the mouse. *Journal of Neurophysiology*, *116*(6), 2676–2688.

Ford, M. C., Alexandrova, O., Cossell, L., Stange-Marten, A., Sinclair, J., Kopp-Scheinpflug, C., Pecka, M., Attwell, D., & Grothe, B. (2015). Tuning of Ranvier node and internode properties in myelinated axons to adjust action potential timing. *Nature Communications*, *6*, 1–14.

Ford, M. C., Grothe, B., & Klug, A. (2009). Fenestration of the calyx of held occurs sequentially along the tonotopic axis, is influenced by afferent activity, and facilitates glutamate clearance. *Journal of Comparative Neurology*, *514*(1), 92–106.

Fünfschilling, U., Supplie, L. M., Mahad, D., Boretius, S., Saab, A. S., Edgar, J., Brinkmann, B. G., Kassmann, C. M., Tzvetanova, I. D., Möbius, W., Diaz, F., Meijer, D., Suter, U., Hamprecht, B., Sereda, M. W., Moraes, C. T., Frahm, J., Goebbels, S., & Nave, K. A. (2012). Glycolytic oligodendrocytes maintain myelin and long-term axonal integrity. *Nature*, *485*(7399), 517–521.

García-Mateo, N., Pascua-Maestro, R., Pérez-Castellanos, A., Lillo, C., Sanchez, D., & Ganfornina, M. D. (2018). Myelin extracellular leaflet compaction requires apolipoprotein D membrane management to optimize lysosomal-dependent recycling and glycocalyx removal. *Glia*, *66*(3), 670–687.

Gibson, E. M., Purger, D., Mount, C. W., Goldstein, A. K., Lin, G. L., Wood, L. S., Inema, I., Miller, S. E., Bieri, G., Zuchero, J. B., Barres, B. A., Woo, P. J., Vogel, H., & Monje, M. (2014). Neuronal activity promotes oligodendrogenesis and adaptive myelination in the mammalian brain. *Science*, *344*(6183), 1–27.

Goldberg, J. L. (2003). How does an axon grow? *Genes and Development*, *17*(8), 941–958.

Golding, N. L., Robertson, D., & Oertel, D. (1995). Recordings from slices indicate that octopus cells of the cochlear nucleus detect coincident firing of auditory nerve fibers with temporal precision. *Journal of Neuroscience*, *15*(4), 3138–3153.

Grothe, B., & Pecka, M. (2014). The natural history of sound localization in mammals - a story of neuronal inhibition. *Frontiers in Neural Circuits*, *8*(October), 1–19.

Grothe, B., Pecka, M., & McAlpine, D. (2010). Mechanisms of Sound Localization in Mammals. *Physiological Reviews*, *90*(3), 983–1012.

Hartline, D. K., & Colman, D. R. (2007). Rapid Conduction and the Evolution of Giant Axons and Myelinated Fibers. *Current Biology*, *17*(1), 29–35.

Hildebrand, C., Remahl, S., Persson, H., & Bjartmar, C. (1993). Myelinated nerve fibres in the CNS. *Progress in Neurobiology*, *40*(3), 319–384.

Hill, R., Alice, L. M., & Grutzendler, J. (2018). Lifelong cortical myelin plasticity and age-related degeneration in the live mammalian brain Robert. *Nature Neuroscience*, *21*(5), 683–695.

Hodgkin, B. Y. a L. (1954). *Ii, Along Vi. I 954*, 221–224.

Hoffpauir, B. K., Grimes, J. L., Mathers, P. H., & Spirou, G. A. (2006). Synaptogenesis of the calyx of Held: Rapid onset of function and one-to-one morphological innervation. *Journal of Neuroscience*, *26*(20), 5511–5523.

Holcomb, P. S., Hoffpauir, B. K., Hoyson, M. C., Jackson, D. R., Deerinck, T. J., Marrs, G. S., Dehoff, M., Wu, J., Ellisman, M. H., & Spirou, G. A. (2013). Synaptic inputs compete during rapid formation of the calyx of held: A new model system for neural development. *Journal of Neuroscience*, *33*(32), 12954–12969.

Hursh, J. B. (1939). Velocity and diameter. *American Journal of Physiology*, *127*, 131–139.

Huxley, A. F., & Stampfli, R. (1949). Evidence for Saltatory Conduction in. *J. Physiol.*, *108*(1946), 315–339.

Ibrahim, M., Butt, A. M., & Berry, M. (1995). Relationship between myelin sheath diameter and internodal length in axons of the anterior medullary velum of the adult rat. *Journal of the Neurological Sciences*, *133*(1–2), 119–127.

Jarjour, A. A., Velichkova, A. N., Boyd, A., Lord, K. M., Torsney, C., Henderson, D. J., & ffrench-Constant, C. (2020). The formation of paranodal spirals at the ends of CNS myelin sheaths requires the planar polarity protein Vangl2. *Glia ,* 68(9), 1840-1858.

Kandler, K., & Friauf, E. (1993). Pre- and postnatal development of efferent connections of the cochlear nucleus in the rat. *Journal of Comparative Neurology*, *328*(2), 161–184.

Kandler, K., & Friauf, E. (1995). Development of glycinergic and glutamatergic synaptic transmission in the auditory brainstem of perinatal rats. *Journal of Neuroscience*, *15*(10), 6890–6904.

Kandler, K., & Gillespie, D. C. (2005). Developmental refinement of inhibitory sound-localization circuits. *Trends in Neurosciences*, *28*(6), 290–296.

Kandler, K., Lee, J., & Pecka, M. (2020). The Superior Olivary Complex. In *The Senses: A Comprehensive Reference* (Second Edi, Vol. 2, pp. 533–555). Elsevier.

Kapfer, C., Seidl, A. H., Schweizer, H., & Grothe, B. (2002). Experience-dependent refinement of inhibitory inputs to auditory coincidence-detector neurons. *Nature Neuroscience*, *5*(3), 247–253.

Kaplan, M. R., Meyer-Franke, A., Lambert, S., Bennett, V., Duncan, I. D., Levinson, S. R., & Barres, B. A. (1997). Induction of sodium channel clustering by oligodendrocytes. *Nature*, *386*(6626), 724–728.

Kasischke, K. A., Vishwasrao, H. D., Fisher, P. J., Zipfel, W. R., & Webb, W. W. (2004). Neural activity triggers neuronal oxidative metabolism followed by astrocytic glycolysis. *Science*, *305*(5680), 99–103.

Kessaris, N., Fogarty, M., Iannarelli, P., Grist, M., Wegner, M., & Richardson, W. D. (2006). Competing waves of oligodendrocytes in the forebrain and postnatal elimination of an embryonic lineage. *Nature Neuroscience*, *9*(2), 173–179.

Kim, G., & Kandler, K. (2003). Elimination and strengthening of glycinergic/GABAergic connections during tonotopic map formation. *Nature Neuroscience*, *6*(3), 282–290.

Kim, G., & Kandler, K. (2010). Synaptic changes underlying the strengthening of GABA/ glycinergic connections in the developing lateral superior olive Gunsoo. *Neuroscience*, *171*(3), 924–933.

Kim, S. E., Lee, S. Y., Blanco, C. L., & Kim, J. H. (2014). Developmental profiles of the intrinsic properties and synaptic function of auditory neurons in preterm and term baboon neonates. *Journal of Neuroscience*, *34*(34), 11399–11404.

Krasnow, A. M., Ford, M. C., Valdivia, L. E., Wilson, S. W., & Attwell, D. (2018). Regulation of developing myelin sheath elongation by oligodendrocyte calcium transients in vivo. *Nature Neuroscience*, *21*(1), 24–30.

Kuhn, S., Gritti, L., Crooks, D., & Dombrowski, Y. (2019). Oligodendrocytes in Development, Myelin Generation and Beyond. *Cells*, *8*(1424), 1–23.

Kuwabara, N., & Zook, J. M. (1991). Classification of the principal cells of the medial nucleus of the trapezoid body. *Journal of Comparative Neurology*, *314*(4), 707–720.

Lang, E. J., & Rosenbluth, J. (2003). Role of myelination in the development of a uniform olivocerebellar conduction time. *Journal of Neurophysiology*, *89*(4), 2259–2270.

Lee, S., Leach, M. K., Redmond, S. A., Chong, S. Y. C., Mellon, H., Tuck, S. J., Feng, Z., Corey, J. M., & Chan, J. R. (2012). A culture system to study oligodendrocyte myelination- processes using engineered nanofibers Seonok. *Nature Methods*, *9*(9), 917–922.

Lee, Y., Morrison, B. M., Li, Y., Lengacher, S., Farah, M. H., Hoffman, P. N., Liu, Y., Tsingalia, A., Jin, L., Zhang, P. W., Pellerin, L., Magistretti, P. J., & Rothstein, J. D. (2012). Oligodendroglia metabolically support axons and contribute to neurodegeneration. *Nature*, *487*(7408), 443–448.

Lingner, A., Pecka, M., Leibold, C., & Grothe, B. (2018). A novel concept for dynamic adjustment of auditory space. *Scientific Reports*, *8*(1), 1–12.

Liu, J., Dietz, K., DeLoyht, J. M., Pedre, X., Kelkar, D., Kaur, J., Vialou, V., Lobo, M. K., Dietz, D. M., Nestler, E. J., Dupree, J., & Casaccia, P. (2012). Impaired adult myelination in the prefrontal cortex of socially isolated mice. *Nature Neuroscience*, *15*(12), 1621–1623.

Liu, J., Dupree, J. L., Gacias, M., Frawley, R., Sikder, T., Naik, P., & Casaccia, P. (2016). Clemastine enhances myelination in the prefrontal cortex and rescues behavioral changes in socially isolated mice. *Journal of Neuroscience*, *36*(3), 957–962.

Liu, P., Du, J. L., & He, C. (2013). Developmental pruning of early-stage myelin segments during CNS myelination in vivo. *Cell Research*, *23*(7), 962–964.

Magnusson, A. K., Kapfer, C., Grothe, B., & Koch, U. (2005). Maturation of glycinergic inhibition in the gerbil medial superior olive after hearing onset. *Journal of Physiology*, *568*(2), 497–512.

McKenzie, I. A., Ohayon, D., Li, H., De Faria, J. P., Emery, B., Tohyama, K., & Richardson, W. D. (2014). Motor skill learning requires active central myelination. *Science*, *346*(6207), 318–322.

Micheva, K. D., Wolman, D., Mensh, B. D., Pax, E., Buchanan, J., Smith, S. J., & Bock, D. D. (2016). A large fraction of neocortical myelin ensheathes axons of local inhibitory neurons. *ELife*, *5*, 1–29.

Morrison, B. M., Lee, Y., & Rothstein, J. D. (2013). Oligodendroglia metabolically support axons and maintain structural Structural integrity. *Trends in Cell Biology*, *23*(12), 1–17.

Mueller, B. K. (1999). Growth cone guidance: First steps towards a deeper understanding. *Annual Review of Neuroscience*, *22*, 351–388.

Murray, J. A., & Blakemore, W. F. (1980). The Relationship between Internodal Length and Fibre Diameter in the Spinal Cord of the Rat. *Journal of Neurological Sciences*, *45*, 29–41.

Murtie, J. C., Macklin, W. B., & Corfas, G. (2007). Morphometric Analysis of Oligodendrocytes in the Adult Mouse Frontal Cortex. *Journal of Neuroscience Research*, *85*, 2080–2086.

Muzio, M. R., & Cascella, M. (2021). Histology , Axon. *StatPearls. StatPearls Publishing*.

Myoga, M. H., Lehnert, S., Leibold, C., Felmy, F., & Grothe, B. (2014). Glycinergic inhibition tunes coincidence detection in the auditory brainstem. *Nature Communications*, *5*(May), 1–13.

Nave, K. A. (2010). Myelination and support of axonal integrity by glia. *Nature*, *468*(7321), 244–252.

Oertel, D. (1997). Encoding of timing in the brain stem auditory nuclei of vertebrates. *Neuron*, *19*(5), 959–962.

Oertel, D., Bal, R., Gardner, S. M., Smith, P. H., & Joris, P. X. (2000). Detection of synchrony in the activity of auditory nerve fibers by octopus cells of the mammalian cochlear nucleus. *Proceedings of the National Academy of Sciences of the United States of America*, *97*(22), 11773–11779.

Ohno, N., Kidd, G. J., Mahad, D., Kiryu-Seo, S., Avishai, A., Komuro, H., & Trapp, B. D. (2011). Myelination and axonal electrical activity modulate the distribution and motility of mitochondria at CNS nodes of Ranvier. *Journal of Neuroscience*, *31*(20), 7249–7258.

Pajevic, S., Basser, P. J., & Fields, R. D. (2014). Role of myelin plasticity in oscillations and synchrony of neuronal activity. *Neuroscience*, *276*, 135–147.

Pecka, M., Brand A., Behrend, O., & Grothe, B (2008). Interaural time difference processing in the mammalian medial superior olive: the role of glycinergic inhibition. *Journal of Neuroscience, 28(27),* 6914-6925.

Pecka, M., & Encke, J. (2020). Coding of Spatial Information. In *The Senses: A Comprehensive Reference* (Vol. 2, pp. 713–731).

Pedraza, L., Huang, J. K., & Colman, D. R. (2001). Organizing principles of the axoglial apparatus. *Neuron*, *30*(2), 335–344.

Pellerin, L., & Magistretti, P. J. (1994). Glutamate uptake into astrocytes stimulates aerobic glycolysis: A mechanism coupling neuronal activity to glucose utilization. *Proceedings of the National Academy of Sciences of the United States of America*, *91*(22), 10625–10629.

Perkins, R. E. (1973). An electron microscopic study of synaptic organization in the medial superior olive of normal and experimental chinchillas. *Journal of Comparative Neurology*, *148*(3), 387–415.

Philips, T., & Rothstein, J. D. (2017). Oligodendroglia: metabolic supporters of neurons. *The Journal of Clinical Investigation*, *127*(9), 3271–3280.

Poliak, S., & Peles, E. (2003). The local differentiation of myelinated axons at nodes of ranvier. *Nature Reviews Neuroscience*, *4*(12), 968–980.

Privat, A., Jacque, C., Bourre, J. M., Dupouey, P., & Baumann, N. (1979). Absence of the major dense line in myelin of the mutant mouse “shiverer.” *Neuroscience Letters*, *12*(1), 107–112.

Pumphrey, R. J., & Young, J. Z. (1938). The Rates Of Conduction Of Nerve Fibres Of Various Diameters In Cephalopods. *Journal of Experimental Biology*, *15*(4), 453–466.

Quick, D. C., Kennedy, W. R., & Donaldson, L. (1979). Dimensions of myelinated nerve fibers near the motor and sensory terminals in cat tenuissimus muscles.

Neuroscience, *4*(8), 1089–1096.
Ranvier, L.-A. (1871). Contributions à l'histologie et à la physiologie des nerfs périphériques. *C R Acad Sci*, *73*, 1168–1171.
Rasband, M. N. (2011). Composition, Assembly, and Maintenance of Excitable Membrane Domains in Myelinated Axons. *Semin Cell Dev Biol*, *22*(2), 178–184.
Rasband, M. N., & Peles, E. (2016). The nodes of Ranvier: Molecular assembly and maintenance. *Cold Spring Harbor Perspectives in Biology*, *8*(3), 1–15.
Rasband, M. N., Peles, E., Trimmer, J. S., Levinson, S. R., Lux, S. E., & Shrager, P. (1999). Dependence of nodal sodium channel clustering on paranodal axoglial contact in the developing CNS. *Journal of Neuroscience*, *19*(17), 7516–7528.
Rayleigh, Lord. (1907). XII. On Our Perception of Sound Direction. *Philos. Mag.*, *13*, 214–232.
Readhead, C., Popko, B., Takahashi, N., Saavedra, R. A., Sidman, R. L., & Hood, L. (1987). Expression of a myelin basic protein gene in transgenic shiverer mice: Correction of the dysmyelinating phenotype. *Cell*, *47*(4), 703–712.
Remahl, S., & Hildebrand, C. (1982). Changing relation between onset of myelination and axon diameter range in developing feline white matter. *Journal of the Neurological Sciences*, *54*(1), 33–45.
Roberts, M. T., Seeman, S. C., & Golding, N. L. (2013). A mechanistic understanding of the role of feedforward inhibition in the mammalian sound localization circuitry. *Neuron*, *78*(5), 923–935.
Rosenbluth, J. (1980). Central myelin in the mouse mutant shiverer. *Journal of Comparative Neurology*, *194*(3), 639–648.
Rosenbluth, J. (2009). Multiple functions of the paranodal junction of myelinated nerve fibers. *Journal of Neuroscience Research*, *87*(15), 3250–3258.
Rowitch, D. H., & Kriegstein, A. R. (2010). Developmental genetics of vertebrate glial-cell specification. *Nature*, *468*(7321), 214–222.
Rushton, W. A. H. (1951). A Theory of the Effects of Fibre Size in Medullated Nerve. *J. Physiol.*, *115*, 101–122.
Salami, M., Itami, C., Tsumoto, T., & Kimura, F. (2003). Change of conduction velocity by regional myelination yields constant latency irrespective of distance between thalamus and cortex. *Proceedings of the National Academy of Sciences of the United States of America*, *100*(10), 6174–6179.
Salzer, J. L. (2003). Polarized Domains of Myelinated Axons. *Neuron*, *40*(2), 297–318.
Sanes, D. H. (1993). The development of synaptic function and integration in the central auditory system. *Journal of Neuroscience*, *13*(6), 2627–2637.
Sanes, D. H., Goldstein, N. A., Ostad, M., & Hillman, D. E. (1990). Dendritic morphology of central auditory neurons correlates with their tonotopic position. *Journal of Comparative Neurology*, *294*(3), 443–454.
Sanes, D. H., & Siverls, V. (1991). Development and specificity of inhibitory terminal arborizations in the central nervous system. *Journal of Neurobiology*, *22*(8), 837–854.
Sanes, D. H., Song, J., & Tyson, J. (1992). Refinement of dendritic arbors along the tonotopic axis of the gerbil lateral superior olive. *Developmental Brain Research*, *67*(1), 47–55.
Sätzler, K., Söhl, L. F., Bollmann, J. H., Borst, J. G. G., Frotscher, M., Sakmann, B.,

& Lübke, J. H. R. (2002). Three-dimensional reconstruction of a calyx of Held and its postsynaptic principal neuron in the medial nucleus of the trapezoid body. *Journal of Neuroscience*, *22*(24), 10567–10579.
Schafer, D. P., Custer, A. W., Shrager, P., & Rasband, M. N. (2006). Early events in node of Ranvier formation during myelination and remyelination in the PNS. *Neuron Glia Biology*, *2*(2), 69–79.
Scholz, J., Klein, M. C., Behrens, T. E. J., & Johansen-berg, H. (2010). Europe PMC Funders Group Training induces changes in white matter architecture. *Nat Neurosci.*, *12*(11), 1370–1371.
Seidl, A. H. (2014). Regulation of conduction time along axons. *Neuroscience*, *276*, 126–134.
Seidl, A. H., & Rubel, E. W. (2016). Systematic and differential myelination of axon collaterals in the mammalian auditory brainstem. *Glia*, *64*(4), 487–494.
Seidl, A. H., Rubel, E. W., & Harris, D. M. (2010). Mechanisms for adjusting interaural time differences to achieve binaural coincidence detection. *Journal of Neuroscience*, *30*(1), 70–80.
Sherman, D. L., & Brophy, P. J. (2005). Mechanisms of axon ensheathment and myelin growth. *Nature Reviews Neuroscience*, *6*(9), 683–690.
Simons, M., & Lyons, D. A. (2013). Axonal selection and myelin sheath generation in the central nervous system. *Current Opinion in Cell Biology*, *25*(4), 512–519.
Simons, M., & Nave, K. A. (2016). Oligodendrocytes: Myelination and axonal support. *Cold Spring Harbor Perspectives in Biology*, *8*(1).
Sinclair, J. L., Fischl, M. J., Alexandrova, O., Heβ, M., Grothe, B., Leibold, C., & Kopp-Scheinpflug, C. (2017). Sound-evoked activity influences myelination of brainstem axons in the trapezoid body. *Journal of Neuroscience*, *37*(34), 8239–8255.
Smith, R. S., & Koles, Z. J. (1970). Myelinated nerve fibers: computed effect of myelin thickness on conduction velocity. *American Journal of Physiology*, *219*(5), 1256–1258.
Snaidero, N., & Simons, M. (2014). Myelination at a glance. *Journal of Cell Science*, *127*(14), 2999–3004.
Sobottka, B., Ziegler, U., Kaech, A., Becher, B., & Goebels, N. (2011). CNS live imaging reveals a new mechanism of myelination: The liquid croissant model. *Glia*, *59*(12), 1841–1849.
Sonntag, M., Englitz, B., Kopp-Scheinpflug, C., & Rübsamen, R. (2009). Early postnatal development of spontaneous and acoustically evoked discharge activity of principal cells of the medial nucleus of the trapezoid body: An in vivo study in mice. *Journal of Neuroscience*, *29*(30), 9510–9520.
Stadelmann, C., Timmler, S., Barrantes-Freer, A., & Simons, M. (2019). Myelin in the central nervous system: Structure, function, and pathology. *Physiological Reviews*, *99*(3), 1381–1431.
Stange-Marten, A., Nabel, A. L., Sinclair, J. L., Fischl, M., Alexandrova, O., Wohlfrom, H., Kopp-Scheinpflug, C., Pecka, M., & Grothe, B. (2017). Input timing for spatial processing is precisely tuned via constant synaptic delays and myelination patterns in the auditory brainstem. *Proceedings of the National Academy of Sciences of the United States of America*, *114*(24).
Stedehouder, J., Brizee, D., Shpak, G., & Kushner, S. A. (2018). Activity-dependent myelination of parvalbumin interneurons mediated by axonal morphological

plasticity. *Journal of Neuroscience*, *38*(15), 3631–3642.
Suminaite, D., Lyons, D. A., & Livesey, M. R. (2019). Myelinated axon physiology and regulation of neural circuit function. *Glia*, *67*(11), 2050–2062.
Susuki, K., Chang, K. J., Zollinger, D. R., Liu, Y., Ogawa, Y., Eshed-Eisenbach, Y., Dours-Zimmermann, M. T., Oses-Prieto, J. A., Burlingame, A. L., Seidenbecher, C. I., Zimmermann, D. R., Oohashi, T., Peles, E., & Rasband, M. N. (2013). Three mechanisms assemble central nervous system nodes of ranvier. *Neuron*, *78*(3), 469–482.
Susuki, K., & Kuba, H. (2016). Activity-dependent regulation of excitable axonal domains. *Journal of Physiological Sciences*, *66*(2), 99–104.
Tagoe, T., Barker, M., Jones, A., Allcock, N., & Hamann, M. (2014). Auditory nerve perinodal dysmyelination in noise-induced hearing loss. *Journal of Neuroscience*, *34*(7), 2684–2688.
Tasaki, I. (1939). The Electro-Saltatory Transmission of the Nerve Impulse and the Effect of Narcosis upon the Nerve Fiber. *The American Journal of Physiology*, *127*(211–227), 1246.
Taschenberger, H., Leão, R. M., Rowland, K. C., Spirou, G. A., & Von Gersdorff, H. (2002). Optimizing synaptic architecture and efficiency for high-frequency transmission. *Neuron*, *36*(6), 1127–1143.
Taschenberger, H., & Von Gersdorff, H. (2000). Fine-tuning an auditory synapse for speed and fidelity: Developmental changes in presynaptic waveform, EPSC kinetics, and synaptic plasticity. *Journal of Neuroscience*, *20*(24), 9162–9173.
Tollin, D. J. (2003). The lateral superior olive: A functional role in sound source localization. *Neuroscientist*, *9*(2), 127–143.
Tolnai, S., Beutelmann, R., & Klump, G. M. (2017). Exploring binaural hearing in gerbils (Meriones unguiculatus) using virtual headphones. *PLoS ONE*, *12*(4), 7–12.
Tomassy, G. S., Berger, D. R., Chen, H., Kasthuri, N., Hayworth, K. J., Vercelli, A., Seung, H. S., Lichtman, J. W., & Arlotta, P. (2014). Distinct profiles of myelin. *Science*, *344*(6181), 319–324.
Tripathi, V., Ellis, J. D., Shen, Z., Song, D. Y., Pan, Q., Watt, A. T., Freier, S. M., Bennett, C. F., Sharma, A., Bubulya, P. A., Blencowe, B. J., Prasanth, S. G., & Prasanth, K. V. (2010). The nuclear-retained noncoding RNA MALAT1 regulates alternative splicing by modulating SR splicing factor phosphorylation. *Molecular Cell*, *39*(6), 925–938.
Vabnick, I., Novaković, S. D., Levinson, S. R., Schachner, M., & Shrager, P. (1996). The clustering of axonal sodium channels during development of the peripheral nervous system. *Journal of Neuroscience*, *16*(16), 4914–4922.
Velumian, A. A., Samoilova, M., & Fehlings, M. G. (2011). Visualization of cytoplasmic diffusion within living myelin sheaths of CNS white matter axons using microinjection of the fluorescent dye Lucifer Yellow. *NeuroImage*, *56*(1), 27–34.
Virchow, R. (1856). *Gesammelte Abhandlungen zur wissenschaftlichen Medicin*. Meidinger.
von Gersdorff, H., & Borst, J. G. G. (2002). Short-term plasticity at the calyx of held. *Nature Reviews Neuroscience*, *3*(1), 53–64.
Waxman, S. G. (1980). Determinants of conduction velocity in myelinated nerve fibers. *Muscle & Nerve*, *3*(2), 141–150.

Waxman, S. G., & Bennett, M. V. I. (1972). Relative conduction velocities of small myelinated and non-myelinated fibres in the central nervous system. *Nature New Biology*, *238*(85), 217–219.

Weil, M. T., Heibeck, S., Töpperwien, M., Tom Dieck, S., Ruhwedel, T., Salditt, T., Rodicio, M. C., Morgan, J. R., Nave, K. A., Möbius, W., & Werner, H. B. (2018). Axonal ensheathment in the nervous system of lamprey: Implications for the evolution of myelinating glia. *Journal of Neuroscience*, *38*(29), 6586–6596.

Werthat, F., Alexandrova, O., Grothe, B., & Koch, U. (2008). Experience-dependent refinement of the inhibitory axons projecting to the medial superior olive. *Developmental Neurobiology*, *68*(13), 1454–1462.

Wimmer, V. C., Horstmann, H., Groh, A., & Kuner, T. (2006). Donut-like topology of synaptic vesicles with a central cluster of mitochondria wrapped into membrane protrusions: A novel structure-function module of the adult calyx of held. *Journal of Neuroscience*, *26*(1), 109–116.

Wu, L. M. N., Williams, A., Delaney, A., Sherman, D. L., & Brophy, P. J. (2012). Increasing internodal distance in myelinated nerves accelerates nerve conduction to a flat maximum. *Current Biology*, *22*(20), 1957–1961.

Xiao, L., Michalski, N., Kronander, E., Gjoni, E., Genoud, C., Knott, G., & Schneggenburger, R. (2013). BMP signaling specifies the development of a large and fast CNS synapse. *Nature Neuroscience*, *16*(7), 856–864.

Xiao, L., Ohayon, D., Mckenzie, I. A., Sinclair-wilson, A., & Jordan, L. (2017). *Europe PMC Funders Group Rapid production of new oligodendrocytes is required in the earliest stages of motor skill learning*. *19*(9), 1210–1217.

Xu, J., Berret, E., & Kim, J. H. (2017). Activity-dependent formation and location of voltage-gated sodium channel clusters at a CNS nerve terminal during postnatal development. *Journal of Neurophysiology*, *117*(2), 582–593.

Zalc, B., & Coleman, D. R. (2000). Origins of Vertebrate Success. *Science*, *288*(5464), 271–272.

Zalc, B., Goujet, D., & Colman, D. (2008). The origin of the myelination program in vertebrates. *Current Biology*, *18*(12), 511–512.

Zhang, C., Susuki, K., Zollinger, D. R., Dupree, J. L., & Rasband, M. N. (2013). Membrane domain organization of myelinated axons requires βII spectrin. *Journal of Cell Biology*, *203*(3), 437–443.

LIST OF ABBREVIATIONS

AIS	axon initial segment
AnkG	AnkyrinG
AP	action potential
ATP	adenosine triphosphate
AVCN	anteroventral cochlear nucleus
CAMS	cell adhesion molecules
CASPR	contacin associated protein
CN	cochlear nucleus
CNS	central nervous system
Cntn	contactin
ECM	extracellular matrix
GBC	globular bushy cell
ILD	interaural level difference
ITD	interaural time difference
JXP	juxtaparanode
kHz	kilohertz
K_v	voltage gated potassium channel
L/d	internode length to axon diameter ratio
LNTB	lateral nucleus of the trapezoid body
LSO	lateral superior olive
MBP	myelin basic protein
MCT1	monocarboxylate transporter 1
MCT2	monocarboxylate transporter 2
MNTB	medial nucleus of the trapezoid body
MSO	medial superior olive
Na_v	voltage gated sodium channel
NF155	Neurofascin 155
NF186	Neurofascin 186
OPC	oligodendrocyte precursor cell
P	postnatal day
PLP	proteolipid protein
PNJ	paranodal junction
PNS	peripheral nervous system
SBC	spherical bushy cell

ACKNOWLEDGEMENTS

First and foremost, thank you, Benedikt, for giving me the opportunity to work in your lab. You convincingly guided and encouraged me to become an independent and responsible researcher. You have always giving me the freedom to pursue my own ideas and put such great trust in my work. Thank you for always making time whenever I needed help and for always keeping your door open no matter what my requests were. Thank you for the many lively discussions, new ideas, and your helpful advice. I wouldn't be where I am today without you, and I couldn't have asked for a better supervisor.

I would also like to thank my other TAC members. Thank you, Tim, for sharing your expertise and giving me new ideas from a different perspective. I have always enjoyed listening to your in-depth knowledge of myelin and I am grateful for all the helpful advice you have given me. Thank you, Misku, for your constant insightful comments and suggestions, and for always making great stories out of my data. And thank you, Conny, for your constructive inputs and warm encouragement.

I cannot begin to express my gratitude to Hilde and Olga, without whose support this work would not have been possible. I am beyond grateful for everything you have done for me and helped me with, basically throughout my entire PhD. You have always been my rock whenever I needed you and you always knew what to do even when the road got tough.

Thank you to the former Felmy-crew, who welcomed me so warmly the moment I entered the office that I would not leave for the next seven years. Thanks to Sarah and Felix, for awakening my enthusiasm for neuroscience and to Delwen, Franzi and Alex for being the best office mates I could imagine.

Thank you to Paula, Leni and Sina for their thorough and reliable work, which provided me with important data.

I would like to thank everyone in the Neurobiology department for numerous discussions and always being willing to help. Special thanks to Eli, Ela, Ella, Sarah, Magdalena, Gregory, Diana and Basti who not only accompanied my PhD but also built many good memories and made the time fly by.

I would like to thank the Graduate School of Systemic Neuroscience (GSN) for providing the best environment for a successful PhD. Special thanks to the wonderful administrative office for always being there to help no matter how small the problems were

I would like to thank all of my friends who made Munich my home, who always supported and motivated me, and who kept me going on.

Of course, I want to thank my family for their enduring support and for constantly encouraging me and believing in me. Thank you, Nora for being the best big sister I could imagine.

Zum Schluss möchte ich der Person danken, die immer hinter mir stand, die immer an mich geglaubt und niemals meine Entscheidungen hinterfragt oder angezweifelt hat. Ohne dich wäre all das nicht möglich gewesen. Danke, Mama.